



**The 2014-2015 lava flow field at Holuhraun:
Deriving physical properties of the lava
using multi remote sensing techniques and
datasets**

Muhammad AUFARISTAMA



**Faculty of Earth Sciences
University of Iceland
2020**

The 2014-2015 lava flow field at Holuhraun: Deriving physical properties of the lava using multi remote sensing techniques and datasets

Muhammad AUFARISTAMA

Dissertation submitted in partial fulfillment of a
Philosophiae Doctor degree in Earth Sciences

Advisor

Dr. Armann Höskuldsson, University of Iceland, Iceland

PhD Committees

Dr. Magnus Örn Úlfarsson, University of Iceland, Iceland
Dr. Ingibjörg Jónsdóttir, University of Iceland, Iceland
Dr. Thorvaldur Thordarson, University of Iceland, Iceland

Opponents

Dr. Chris Hecker, University of Twente, The Netherlands
Dr. Catherine Neish, The University of Western Ontario, Canada

Faculty of Earth Sciences
School of Engineering and Natural Sciences
University of Iceland
Reykjavik, April 2020

The 2014-2015 lava flow field at Holuhraun: Deriving physical properties of the lava using multi remote sensing techniques and datasets
Deriving physical properties of the lava using remote sensing
Dissertation submitted in partial fulfilment of a *Philosophiae Doctor* degree in Earth Sciences

Copyright © 2020 Muhammad AUFARISTAMA
All rights reserved

Faculty of Earth Sciences
School of Engineering and Natural Sciences
University of Iceland
Askja, Sturlugata 7
101, Reykjavik
Iceland

Telephone: 525 4000

Bibliographic information:

Muhammad AUFARISTAMA, 2020, *The 2014-2015 lava flow field at Holuhraun: Deriving physical properties of the lava using multi remote sensing techniques and datasets*, PhD dissertation, Faculty of Earth Sciences, University of Iceland, 121 pp.

Author ORCID: 0000-0002-1962-7511

ISBN 978-9935-9412-9-9

Printing: Háskólaprent
Reykjavik, Iceland, April 2020

Abstract

The purpose of this thesis is to employ remote sensing to study lava flow products during the 2014-2015 eruption at Holuhraun, Iceland. Multimodal remote sensing techniques and datasets were applied and developed for three study themes (1) deriving thermal properties from satellite infrared remote sensing, (2) differentiating lava surface using airborne hyperspectral remote sensing, and (3) quantifying lava surface roughness from elevation model acquired by airborne LiDAR.

In the first study, we present a new approach based on infrared satellite images to derive thermal properties within the lava field during eruption and then compare the results with field measurement during the 2014-2015 eruption at Holuhraun. We develop a new spectral index for Landsat 8, named the thermal eruption index (TEI), based on the SWIR and TIR bands (bands 6 and 10). The purpose of the TEI consists mainly of two parts: (i) as a threshold for differentiating between different thermal domains; and (ii) to apply dual-band technique to determine the maximum subpixel temperature (T_h) of the lava. Lava surface roughness effects are accounted for by using the Hurst exponent (H), which is estimated from radar backscattering profiles. A higher H (smooth surface) generates thinner crust and high thermal flux meanwhile a lower H (rough surface) generates thicker crust and lower thermal flux. The total thermal flux peak is underestimated compared to other studies, although the trend shows good agreement with both field observation and other studies.

In the second study, we focus on retrieving the lava surface types contributing to the signal recorded by airborne hyperspectral at the very top surface of the 2014-2015 lava flow field at Holuhraun. For this purpose, an airborne hyperspectral image acquired at Holuhraun with an AisaFENIX sensor onboard a NERC (Natural Environment Research Council Airborne Research Facility) campaign. For sub-pixel analysis, we used the sequential maximum angle convex cone (SMACC) algorithm to identify the spectral image endmembers and the linear spectral mixture analysis (LSMA) method was employed to retrieve the abundances. SMACC and LSMA methods offer a fast selection for volcanic product segregation. However, ground-truthing of spectra is recommended for future work.

In the third study, we perform both the topographic position index (TPI) and one-dimensional Hurst Exponent to derived lava flow unit roughness on the 2014-2015 lava flow field at Holuhraun using both airborne LiDAR and photogrammetry topography datasets. The roughness assessment was acquired from four lava flow features: (1) spiny pāhoehoe, (2) lava pond, (3) rubbly pāhoehoe lava, and (4) inflated channel. The TPI patterns on spiny lava and inflated channels show that the intermediate TPI values correspond to a small slope indicating a flat and smooth surface. Lava pond is characterized by low to high TPI values and forms a wave-like pattern. Meanwhile, irregular transitions patterns from low to high TPI values characterize lava with rough blocky surfaces, i.e. rubbly pāhoehoe to 'ā'a flows and lobes and their margins. These lobes and margins may give the impression of having similar roughness as the "rough" surface on meters scale since this is an "apparent" roughness. On centimeters scale these

multitudes of lobes feature coherent and smooth surfaces because they are pāhoehoe. The surface roughness of these lava features falls within the H range of 0.30 ± 0.05 to 0.76 ± 0.04 . The bubbly pāhoehoe / 'ā'a has the roughest surface and the inflated lava channel along with pāhoehoe feature the smoothest surfaces among these four surface types. In general, the Hurst exponent values in the 2014-2015 lava field at Holuhraun has a strong tendency in 0.5, which is compatible with results from other study of geological surface roughness.

Overall, this project provides an important insights into the application of remote sensing for monitoring and studying active lava flow fields and the techniques developed here will benefit such work in future events.

Útdráttur

Tilgangurinn með verkefninu var að rannsaka hraunrennsli og landform er urðu til í eldgosinu norðan Vatnajökuls 2014-2015 og kennt við Holuhraun. Fjölþátta fjarkönnunartækni og gögn úr gervitunglum og flugvélum voru nýtt við úrvinnslu verkefnisins. Rannsóknin sneri að þremur megin þáttum: (1) greiningu á eðli varmaústreymis frá Holuhrauni, út frá innrauðri varmageislun sem mæld er með gervitunglagögnum (2) aðgreining á mismunandi hraunfyrirborði, út frá ofur-fjölrófs mælingum úr lofti, og (3) greiningu og flokkun á yfirborðshrjúfleika Holuhrauns út frá hæðarlíkani er aflað var með LiDAR settur upp í flugvél.

Fyrsti þáttur beindist að eðli varmaústreymis á meðan á eldgosi stóð. Stuðst var við gervitunglagögn og mælingar með FLIR tækni á meðan eldgosið stóð yfir. Afraksturinn er nýr hitastuðull fyrir Landsat 8 og greiningu á eldgosum, (TEI). Hitastuðullinn TEI er unninn út frá SWIR og TIR böndum Landsat 8 (bönd 6 og 10). Með TEI næst fram tvennt: (i) að greina þröskuld milli tveggja hitasviða; og (ii) að beita tvíbanda tækni til að greina hitastig innan hverrar myndeiningar (Th) af hrauninu. Hrjúfleiki hraunsins hefur áhrif á varmaústreymi, og er gert ráð fyrir honum með því að reikna Hurst veldisstuðulinn (H) og eru reiknuð út frá radar endurkasti hraunfyrirborðs. Hátt H einkennir flatt og mjúkt yfirborð og þunna skorpu á hrauninu, á meðan að lágt H einkennir úfið yfirborð, þykka skorpu og lága varmaúteislun. Heildar varmaúteislun með þessari aðferð er heldur vanmetin en ofmetin í samanburði við aðrar aðferðir. Hinsvegar er góð fylgni með mælingum í mörkinni og samanburðar aðferðum.

Annar hluti rannsóknarinnar sneri að túlkun ofur-fjölrófsgreininga á yfirborði Holuhrauns. Flogið var yfir Holuhraun sumarið 2015 með ofur-fjölrófsmæli (AisaFENIX) um borð í flugvél frá NERC (Natural Environment Research Council Airborne Research Facility). Við greiningu á yfirborði innan hverrar myndeiningar var, (i) notast við aðferð runubundins hámarkshorns kúprar keilu (SMACC) til að finna útmörk ofurrófs mælinganna, (ii) blönduð línulega rófgreining (LSMA) var nýtt til að greina styrk eða gnægð innan myndeiningar. SMACC og LSMA aðferðirnar bjóða upp á mjög hraða greiningu á yfirborði og útfellingum efna á yfirborðið. Hins vegar þarf að gera fleiri rófmælingar á staðnum, til þess að auka notkunnargetu aðferðarinnar í hraungosum framtíðarinnar.

Þriðji þáttur rannsóknarinnar sneri að því að greina landfræðilega stöðuvísitölu (TPI) og einvíðan Hurst veldisvísi til að meta hrjúfleika á hinu endanlega yfirborði Holuhrauns. Við þessa greiningu var notast við LiDAR mælingu af hrauninu og hæðagrunn unninn út frá ljósmyndum. Hrjúfleikinn var metinn fyrir fjögur yfirborð sem einkenna hraunið: (1) broddahraun „spiny pāhoehoe lava“, (2) hrauntjörn „lava pond“, (3) klumpahraun „rubbly pāhoehoe lava“ og (4) upptjakkada hrauntröð „inflated lava channel“. TPI fyrir yfirborð (1) og (4) gefur meðalgildi sem einkennist af litlum halla og flötu yfirborði. Hrauntjörnin einkennist af lágum og háum TPI gildum sem endurspeglar bylgjukennt mynstur. Hinsvegar einkennast hrjúfustu yfirborðin (3) og hraunjaðrar af óreglulegu mynstri lágra og hárra TPI gilda. Hrjúfleika stuðull þessara yfirborða H , er á bilinu 0.30 ± 0.05 til 0.76 ± 0.04 . Mestur er hrjúfleiki kubbahrauna og minnstur er hrjúfleiki þandar hrauntraðar. Hurts veldisvísir Holuhrauns er nærri 0.5, en það er í mjög góðu samræmi við niðurstöður fyrri rannsókna á jarðfræðilegum yfirborðum.

Í heild gefur verkefnið mikilvæga sýn á notagildi fjarkönnunaraðferða við rauntímaeftirlit með hraungosum, m.a. með þróun stuðla sem munu nýtast við atburði framtíðar. Þá voru tengsl hraunmyndana við ýmsa eiginleika eldgosa skýrð, sem aftur getur gefið vísendingar um eðli fyrri atburða.

“Kalakuan keok memeh dipacok”

Nothing to lose, don't give up before trying!

*“Gunung teu meunang di lebur, sagara teu meunang di ruksak, buyut teu meunang di
rempak”*

We need to live in harmony with nature

Preface

The occurrence of a volcanic eruption every fourth to five years in Iceland, makes it one of the liveliest places in the world in regard to volcanic eruptions. Over the past 500 years, Iceland's volcanoes have erupted a third of the total global lava output on Earth (Thordarson & Larsen, 2007). Due to this fact, remote sensing will play an essential role developing methods for monitoring of volcanic eruptions, especially for lava flows. This thesis is focused on the application of remote sensing of lava flow products during the 2014-2015 eruption at Holuhraun, Iceland. It is split into three parts utilizing a range of applications of remote-sensing techniques to monitor and understand (a) surface thermal anomalies, (b) surface type and (c) surface roughness of lava flow.

Table of Contents

List of Figures	xiii
List of Tables.....	xiv
Abbreviations	xv
Acknowledgements	xvii
1 Introduction.....	1
1.1 Research Objectives	2
1.2 Remote sensing of volcanoes	2
1.2.1 Remote sensing of a lava flow	3
1.2.2 Infrared remote sensing of the lava flow	4
1.2.3 Hyperspectral unmixing remote sensing on a lava field	5
1.2.4 Lava surface roughness estimated from remote sensing.....	7
1.3 Study area	11
1.3.1 Geologic setting	11
1.3.2 The 2014-2015 Holuhraun eruption.....	12
2 Datasets and Methods.....	15
2.1 Datasets	15
2.1.1 During the eruption	15
2.1.2 Post-eruption	16
2.2 Methods	18
2.2.1 Deriving thermal properties of lava flow during the eruption	18
2.2.2 Discriminating lava surface	20
2.2.3 Deriving roughness properties	21
3 Summary of papers.....	25
3.1 Paper I.....	25
3.1.1 Main highlights of paper I.....	25
3.2 Paper II	26
3.2.1 Main highlights of paper II	26
3.3 Paper III.....	26
3.3.1 Main highlights of paper III.....	27
4 Discussion and Limitations	29
4.1 Deriving thermal properties.....	29
4.2 Hyperspectral unmixing	29
4.3 Roughness indicator	30
5 Concluding remarks	33
6 Synthesis	35

6.1 Future for remote sensing for the volcano, artificial intelligence, and new sensor?.....	35
References	37
Paper I: New Insights for Detecting and Deriving Thermal Properties of Lava Flow Using Infrared Satellite during 2014–2015 Effusive Eruption at Holuhraun, Iceland.....	51
Paper II: The 2014–2015 Lava Flow Field at Holuhraun, Iceland: Using Airborne Hyperspectral Remote Sensing for Discriminating the Lava Surface	77
Paper III: Lava Flow Roughness on the 2014–2015 Lava Flow-Field at Holuhraun, Iceland, Derived from Airborne LiDAR and Photogrammetry.....	99
Appendix A: Deriving Hurst exponent with R/S technique	121

List of Figures

Figure 1.1 Electromagnetic spectrum.....	3
Figure 1.2 Illustration of the mixed pixel concept.....	7
Figure 1.3 The four different surface morphologies that typify the Holuhraun lava flow field.....	10
Figure 1.4 Map presenting Iceland's Neovolcanic Zone.....	12
Figure 1.5 The 2014-2015 eruption at Holuhraun from satellite image.....	13
Figure 2.1 Acquisition map of hyperspectral image at the Holuhraun lava field.....	16
Figure 2.2 The LiDAR DEM of the Holuhraun lava field.....	17
Figure 2.3 Aerial photograph and photogrammetry DEM of the Holuhraun lava field.....	17
Figure 2.4 The workflow used for processing derive thermal properties.....	18
Figure 2.5 The workflow processing used to derive an abundance map.....	20
Figure 2.6 The workflow processing used to assess roughness.....	22
Figure 2.7 The illustration of the topographic position index (TPI).....	23

List of Tables

Table 1.1 Remote sensing sensor that commonly used for lava flow study 4

Table 2.1 Product ID and the dates of the Landsat 8 datasets..... 15

Abbreviations

TIR: Thermal infrared

SWIR: Shortwave infrared

VNIR: Visible near-infrared

VIS: Visible light

TEI: Thermal eruption index

DEM: Digital elevation model

LiDAR: Light detection and ranging

SMACC: Sequential maximum angle convex cone

LSMA: linear spectral mixture analysis

TPI: Topographic position index

Acknowledgements

Alhamdulillah, all the praise and thanks be to Allah, the Almighty, who gave me the ability to finish this PhD thesis successfully. I would like to thank the LPDP and the University of Iceland for granting me the fellowship to provide an excellent opportunity for me to pursue a PhD degree at the University of Iceland.

I would like to give big thanks and full admiration to my PhD supervisors Ármann Höskuldsson, for accepting me as his PhD student. He always supported and guided me and also shared new things about Iceland and the world. I further thank all my advisors and PhD committees Magnús Örn Úlfarsson, Ingibjörg Jónsdóttir, and Thorvaldur Thordarson, who kindly and patiently guided and supported me with their knowledge to accomplish this research, also dedicating a lot of their time to review my writings.

I would like to thank all my fellow in Volcanology and Natural Hazard Group (Eldar-Alda), Institute and Faculty of Earth Sciences at the University of Iceland, who supported me and my research throughout. The Indonesian student in Iceland, I'm grateful to you all for making me always feel like at home.

Last but not least, special thanks and my deepest gratitude to my parents Sudarisman Sofian and Nenni Nuraeni, and my sisters Annisa Benaquina and Azeisha Dienarahmani, and my beloved wife Fella Tiffany and my daughter Askja Aufarsdóttir who always supported and inspired me to strive for a higher quality of life.

1 Introduction

This PhD thesis was carried out at the Institute of Earth Sciences, University of Iceland. The thesis aims to explore multi remote sensing techniques and datasets to derive physical properties of 2014–2015 Holuhraun lava flow during the eruption and after the eruption. The results are presented in three papers: I paper published in *Remote Sensing*, II paper published in *Remote Sensing* and III paper published in *Geosciences*.

Paper I: Aufaristama, M.; Hoskuldsson, A.; Jonsdottir, I.; Ulfarsson, M.O.; Thordarson, T. New Insights for Detecting and Deriving Thermal Properties of Lava Flow Using Infrared Satellite during 2014–2015 Effusive Eruption at Holuhraun, Iceland. *Remote Sens.* 2018, 10, 151. doi.org/10.3390/rs10010151

Paper II: Aufaristama, M.; Hoskuldsson, A.; Ulfarsson, M.O.; Jonsdottir, I.; Thordarson, T. The 2014–2015 Lava Flow Field at Holuhraun, Iceland: Using Airborne Hyperspectral Remote Sensing for Discriminating the Lava Surface. *Remote Sens.* 2019, 11, 476. doi.org/10.3390/rs11050476

Paper III: Aufaristama, M.; Höskuldsson, Á.; Ulfarsson, M.O.; Jónsdóttir, I.; Thordarson, T. Lava Flow Roughness on the 2014–2015 Lava Flow-Field at Holuhraun, Iceland, Derived from Airborne LiDAR and Photogrammetry. *Geosciences* 2020, 10, 125. doi.org/10.3390/geosciences10040125

This PhD study is focused on the 6-month long eruption at Holuhraun in 2014–2015. This event is the largest effusive eruption in Iceland in the past 230 years, with an estimated bulk lava volume of about 1.44 km³. The eruption had an average discharge rate of ~90 m³/s (Kolzenburg et al., 2017; Pedersen et al., 2017). The lava was emplaced on the *sandur* plains (glacial outwash sediment plains) north of the Vatnajökull glacier, partially covering the previous two Holuhraun lava flow fields. The area is gently sloping (average inclination <0.5%; i.e., ~0.3°) to the east-northeast. Field observation during the 2014–2015 eruption was documented in Pedersen et al. (2017), which compiled the evolution history of the lava flow field and corresponding database. Most of these field observations are related to the modes of lava transport, emplacement and thermal camera measurement, along with the mapping of the flow field growth and evolution (Kolzenburg, et al. 2018; Kolzenburg et al., 2017; Pedersen et al., 2017). Because of this extensive documentation of this eruption, it offers an opportunity to improve our understanding of large effusive eruptions using multi-modal remote sensing techniques and datasets. In Paper I, we focused on deriving physical properties of the lava during the eruption, we presented a new approach based on using infrared satellite images to derive thermal properties within the lava field during emplacement and then compared the results with field observation and measurement. Paper II and III focused on the post-eruptive lava field. This lava flow generated in the eruption offers an excellent diverse surface environment to investigate and characterize lava flow fields. In Paper II, we identified the primary lava surface type contributing to the signal recorded by airborne hyperspectral sensor at the very top surface of the 2014–2015 Holuhraun lava field. Further, in this effusive eruption a lava flow field of diverse surface structures and morphologies was generated and observed, and, in Paper

III, we quantified these structures of the lava flow in regard to roughness based on airborne LiDAR and high-resolution airborne photogrammetry DEM. The results from these three papers when compiled, demonstrates the importance and significance of remote sensing as a data set and a tool for monitoring and studying modern day lava flow fields. Here this is achieved by using datasets derived from several remote Sensing tools, namely multispectral, hyperspectral, infrared, radar and LiDAR. Thus, this study provides an insight into how to derive important physical properties of lava flow fields using multi remote sensing techniques and datasets.

1.1 Research Objectives

Based on the aims set at the onset of the project, and through exploiting the unique opportunities presented by the current remote sensing techniques and datasets observed in the Holuhraun eruption in 2014-2015, the main objectives of this thesis are the following:

1. Present a new approach based on infrared satellite images to derive thermal properties within the lava flow field of the 2014-2015 eruption at Holuhraun and then compare the results with field observation and measurement.
2. Identify the main lava surface types contributing to the signal recorded by airborne hyperspectral remote sensing at the very top surface of the 2014-2015 lava flow field at Holuhraun.
3. Develop a quantitative measurement of lava surface roughness to distinguish the 2014-2015 Holuhraun lava surface morphology based on LiDAR measurements and high-resolution DEM.

1.2 Remote sensing of volcanoes

In general terms, remote sensing is the science and practice of acquiring information about an object without direct contact with itself. It is a process that obtains, prepares, and deciphers information of spectral and spatial-temporal nature of an object (Awange et al., 2013; Lillesand & Kiefer, 1987). It uses the entire electromagnetic spectrum (Fig 1.1), ranging from short wavelengths (for example, ultraviolet) to long wavelengths (microwaves) emitted from a target. The information is usually captured at a distance from above the object and set forth on the form of image data. Such data can allow us to determine the composition and nature of the Earth's surface and the atmosphere from local to global scales and assess changes by analyzing the spectrum captured at different points in time. In this sense, remote sensing is useful in providing spatial information that is otherwise difficult or impossible to obtain (Read & Torrado, 2009).

The development of remote sensing for volcanology purposes has increased rapidly during the past decade. Remote sensing provides spectral, spatial, and temporal coverage that can be used for monitoring at numerous volcanoes throughout the world. Many of the volcanoes are remote but has traces that may extend across many hundreds or thousands of square kilometers (Pyle et al., 2013). Volcanoes are inaccessible during eruption and may remain inaccessible for extended periods after the eruption; however, their products can

scatter on a regional to global scale (Pyle et al., 2013). Consequently, since direct measurement can only give us part of the picture of many volcanic processes, remote sensing is playing an increasingly important role in advancing the understanding of the science underlying volcanic processes (Blackett, 2014; Blackett & Matthew, 2017). Satellite, airborne, and ground-based remote sensing are increasingly vital tools for monitoring active or potentially active volcanoes and assessing their likely, real-time, or time-averaged impact. Multiple and complementary data streams are frequently being used both to monitor active volcanoes leading to advance in the understanding of volcanoes. New methodology in remote sensing research of volcanoes is often determined by the technological advancements of novel sensors, the launching of new platforms, and the development of new processing and acquisition techniques. In term of volcanic eruption, remote sensing plays important contributions for preliminary assessment of eruption products such as:

1. Rapid detection of an eruption plume (Arellano, 2013; de Michele et al., 2016).
2. Monitoring of thermal energy emitted from a volcano (Ganci et al., 2013; Harris et al., 1997; Lombardo & Buongiorno, 2006; Murphy et al., 2003).
3. Large area mapping of surface deformation of a volcano (Browning & Gudmundsson, 2015; Gudmundsson et al., 2014; Hollingsworth et al., 2012).
4. Measurement of volcano topography and topographical change (MacKay et al., 1998; Zimelman et al., 2008).
5. Illustrating the spatial distribution of ash, gases, and aerosols produced by eruptions (Schmidt et al., 2015).
6. Referencing a data set for each volcano for quantifying future changes (Pedersen et al., 2018).

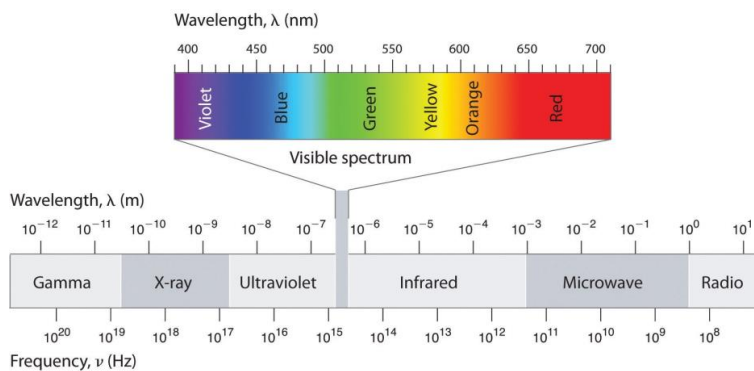


Figure 1.1 Electromagnetic spectrum, giving the terminology used for various wavelength intervals as well as illustrating schematically the characteristic wavelengths. Adapted from (Lillesand & Kiefer, 1987)

1.2.1 Remote sensing of a lava flow

Remote Sensing technology for studying lava flow emerged in the 1980s and has established itself in the following decades (e.g. Oppenheimer, 1991; Pieri et al., 1990; Rothery et al., 1988). It spans a range of applications of remote-sensing techniques, from: 1) monitor surface thermal anomalies, 2) map lava flow emplacement and 3) classify lava flow morphology as illustrated in Table 1.1, which lists several remote sensing sensors

used in monitoring and studying active lava flow along with citations to selective cohort of recent publications.

This thesis is divided into two main parts, firstly an analysis of the lava during the eruption and secondly looking at the final results and the emplaced lava flow field and its characteristics. The papers that make up this thesis cover a range of applications in remote-sensing techniques used to monitor and map; (a) surface thermal anomalies, (b) surface type discrimination and (c) surface roughness of the lava flow.

Table 1.1 Remote sensing sensor that commonly used for lava flow study for different applications

Remote Sensing Sensor	Lava flow application	References
Infrared	lava subpixel temperature, radiant flux, mass eruption rate, volume and lava crust thickness, etc	(Bonny et al., 2018; Harris et al., 1998; Lombardo & Buongiorno, 2006; Oppenheimer, 1991; Wright & Flynn, 2003)
Radar (SAR), LIDAR	Surface roughness, lava morphology, thickness, etc	(Byrnes et al., 2004; James, 2019; Neish et al., 2017; Pedersen et al., 2017; Shepard et al., 2001)
Optical (VIS), Hyperspectral, Multispectral	Lava morphology, surface mineral, surface type, hydrothermal alteration, etc	(Aufaristama et al., 2016; Gudmundsson et al., 2016; Head et al., 2013; James, 2019; Li et al., 2015; Smets et al., 2010)

1.2.2 Infrared remote sensing of the lava flow

Satellite-based infrared remote sensing data are increasingly being used to monitor active volcanoes around the world. Monitoring volcanoes by infrared remote sensing is essential to improve our understanding and occurrence of volcanic eruptions. For example, thermal monitoring of volcanoes and volcanic eruptions does improve our understanding of volcanic eruption processes, since almost all volcanic eruptions are associated with a thermal anomaly, either through changes in temperatures of crater lakes, extrusion of molten material onto the Earth's surface or injection of hot ash and gas into the atmosphere. The potential for using thermal infrared (TIR) measurements to track volcanic eruptions and to constrain volcanic processes has been recognized for many years (e.g., Harris et al., 1998; Harris et al., 1997), with an automated volcanic alert system in operation since 2002 (Wright et al., 2002). Space-based measurements have also been used to estimate the global volcanic heat flux to the atmosphere (Wright et al., 2015).

This dissertation focuses on remote sensing of thermal features associated with an effusive eruption that formed a lava flow. Effusive eruption activity is known for generating lava

fields that can change during the time of emplacement and the development of the lava field. In most cases, thermal observations of active eruptions, from the ground and by aircraft, are risky and difficult, primarily when the lava flow field covers a large area. Satellite-based remote sensing does provide high temporal resolution of infrared data that are very suitable for monitoring large effusive eruptions, as in the case of the 2014-15 effusive eruption at Holuhraun, Iceland. Satellite-based remote sensing provides data that allow for detection of changes in the eruption style and evolution of activity regardless of the coarse spatial resolution of the data (Bonny et al., 2018; Harris et al., 1997).

Satellite-based remote sensing is used to monitor thermal activity within lava fields (Bonny et al., 2018; Ramsey & Harris, 2013; Wright & Flynn, 2003). Over the past 25 years, several remote sensing techniques have been proposed to estimate the thermal structure of active lava flows from infrared remotely-sensed data (Lombardo & Buongiorno, 2006; Lombardo et al., 2004; Pieri et al., 1990), heat flux (Harris et al., 1997; Piscini & Lombardo, 2014; Wright et al., 2010), effusive rate (Morgan, 2012; Oppenheimer, 1991; Zakšek et al., 2015) and crust thickness (Harris et al., 1997; Oppenheimer, 1991). Dozier (1981) developed a method involving a solution of simultaneous equations that allow the calculation of the ‘sub-pixel’ coverage and temperature of cool and hot components. This method is called the dual-band method, and involves two distinct infrared bands to formulate a system of two equations from the simultaneous solution of the Planck equation in each band as shown below:

$$R_x = pR(\lambda_x, T_h) + (1 - p)R(\lambda_x, T_c) \quad (1)$$

$$R_y = pR(\lambda_y, T_h) + (1 - p)R(\lambda_y, T_c) \quad (2)$$

where R_x and R_y are the radiances in bands x and y , respectively, ($\text{Wm}^{-2} \text{sr}^{-1} \text{m}^{-1}$) after adjusting for atmospheric effects and surface emissivity; p is the pixel portion occupied by the hot component; $R(\lambda_x, T_h)$ and $R(\lambda_y, T_c)$ are the radiances ($\text{Wm}^{-2} \text{sr}^{-1} \text{m}^{-1}$) emitted for wavelengths λ_x , and λ_y , at surface temperatures T_h (hot component) and T_c (cool component), respectively. The dual-band method can be applied if the two bands of the short-wave infrared (SWIR) and the thermal infrared (TIR) data are available (Harris, 2013), whereby any two of the unknowns, T_c , T_h , and p , can be estimated if the third is assumed. This method has been successfully applied by several researchers (Flynn et al., 2001; Harris et al., 1997; Lombardo et al., 2004; Lombardo et al., 2012; Lombardo et al., 2006). Harris et al. (1997) and Lombardo et al. (2004) used the dual-band method to retrieve the crust, and the hot cracks temperature for active lava flows in Mt. Etna. They used band 5 (1.55–1.75 μm) and 7 (2.08–2.35 μm) from Landsat Thematic Mapper (TM) and assumed T_h to estimate T_c and p .

1.2.3 Hyperspectral unmixing remote sensing on a lava field

Characterization of surface spectral reflectance by remote sensing is constrained by the spectral resolution as well as by the spatial resolution of the imagery. The spectral reflectance of the lava of different compositions has been documented using laboratory spectrometry measurements on decimeter-size samples (Spinetti et al., 2009). For accessible volcanic terrains, field spectrometry offers a useful alternative approach for characterizing the spectral reflectance of contrasted lava surfaces and for documenting its spatial variation at different spatial scales (Li et al., 2015; Spinetti et al., 2009). The great

variety of morphologies observed in the 2014-2015 lava flow field at Holuhraun (Kolzenburg et al., 2018; Pedersen et al., 2017) encouraged a detailed study of their spectral characteristics, to obtain information about lava composition and detect possible differences in the spectra of the flow. In spectroscopy, the identification of the mineral constituents of major rock types is typically approached using spectral unmixing methods (Daskalopoulou et al., 2018; Li, Canters, et al., 2015). Various spectroscopy studies over the volcanic area (Graettinger et al., 2013; Li et al., 2015; Tayebi et al., 2014) have examined the mineralogical composition of extensive lava fields. Usually, in the visible (VIS) and near-infrared (NIR) spectral range, mafic rocks are characterized by very low reflectance due to the presence of large amounts of dark mafic minerals (Spinetti et al., 2009).

Spectral indices provide a first efficient way to emphasize subtle spectral variants at the surface (Clark & Roush, 1984). More elaborate methods have been developed to distinguish and quantify mixtures of mafic minerals. They have been used to derive composition maps of mafic minerals (Rowan et al., 2005; Zhang et al., 2004; Zhang et al., 2005). However, some lava flows can have a similar chemical/mineralogical composition but different spectral behavior due to the varying grain size, surface texture, and presence of weathering (Aufaristama et al., 2016; Spinetti et al., 2009). The main components of igneous rocks do not display any peculiar spectral features in the visible and near-infrared spectral range. In the case of basalts, the only spectral feature commonly found is an absorption peak due to iron, located around 1000 nm (Clark & Roush, 1984). However, in the case of hydrothermal alteration, hydroxyl bearing minerals show distinctive absorption features in the 2000–2500 nm spectral region (Hellman & Ramsey, 2004). Because of the heterogeneity of a lava surface and due to the limited spectral resolution of the remote sensing sensors, mixed pixels are very common, as is illustrated in Figure 1.2a and Figure 1.2b.

Spectral Mixture Analysis (SMA) has been specially developed to account for mixtures (Adams et al., 1986). Analysis of the data sample can simply be performed on these abundance fractions rather than the sample itself. This method is well-suited for spectroscopic analysis because most of the spectral shapes are due to different materials. The signal detected by a sensor at a single pixel is frequently a combination of numerous disparate signals. Li et al. (2015) used unmixing techniques to discriminate lava flows of different ages at the volcano of Nyamuragira. The most recent study by Daskalopoulou et al. (2018) used unmixing techniques to segregate lava flows and related products from the historical eruptions on Mt. Etna. Nonetheless, to date no lava identification studies that include lava flow delineation through unmixing, have been undertaken in Iceland.

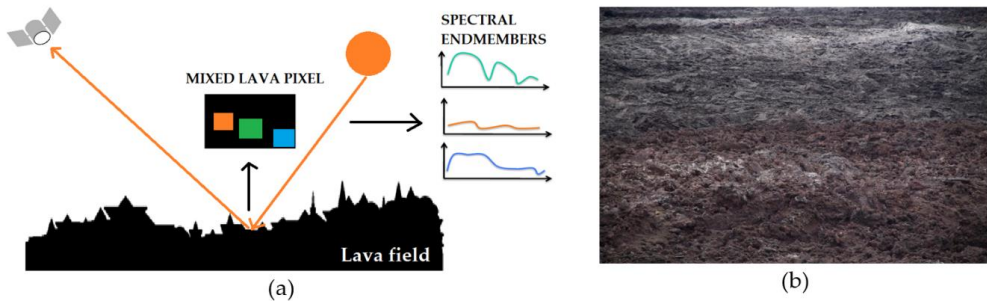


Figure 1.2 Illustration of (a) the mixed pixel in lava surface due to present another spectral in the pixel; (b) variability of lava surfaces in the Holuhraun lava field, which includes oxidizing surface, sulfate mineral, and lava. The original figure was presented in Paper II.

1.2.4 Lava surface roughness estimated from remote sensing

Measurements of lava surface roughness on Earth have been used to describe changes in (i) eruption conditions (Kilburn, 1999; Lopes & Kilburn, 1990; Swanson, 1973), (ii) surface processes that have occurred post-emplacment (Shepard et al., 2001), and (iii) to identify and map out individual lava flows (Gaddis et al., 1990; Morris et al., 2008). The relation between lava roughness and composition has been explored in some detail (e.g. Anderson et al., 1998; Ramsey & Fink, 1999; Shepard et al., 2001). Basaltic lava is generally produced by effusive eruptions and are typified by low magma viscosity, low volatile content and high magmatic temperatures. Fast-flowing lava tend to produce a crust that is disintegrated as it is formed (Anderson et al., 1998; Guest et al., 2012). This influences centimeter to decameter-scale roughness. If the flow of the lava is slow and fully laminar it allows formation of smooth, continuous, coherent crust that typifies pāhoehoe. its formation is initiated by formation of thin viscous skin (Hon et al. 1994). In this case the transport of the lava takes place beneath a stationary crust. This process minimizes the heatloss from the lava interior because it is confined to conductive heat transfer through lava crust. If this crust is, by some process, broken up it results in a rougher lava surface as is the case with rubbly pāhoehoe (Anderson et al., 1998; James, 2019; Keszthelyi, 2002; Keszthelyi et al., 2004).

According to Kilburn (Kilburn, 2000), most basaltic lavas can be grouped using their characteristic surface roughness such as; (1) pāhoehoe, with surfaces is smooth, continuous and coherent surfaces, (2) 'ā'a with its incoherent, clinkery rough and fragmented surfaces, and (3) block lava where is the surface is brecciated and typified by meter-size equant blocks. Hence, studies of lava surface textures and structures gives insight into lava flow dynamics. Generally speaking, lower viscosities or shear strain results in smooth textures; rough textures are the result of higher viscosities, higher shear strain, or disruption of the rapidly cooled surface (Gaddis et al., 1990; Neish et al., 2017; Shepard et al., 2001). Identification of lava surface textures and structures can aid understanding of eruption history as it may indicate changes in the eruption styles, timing of events and geographic extent of the lava (Byrnes et al., 2004).

Emplacment histories can be inferred from variations in lava surface roughness at different scales. Spiny pāhoehoe are typically smooth at meter scale and with mm-cm large

spines spinose preserved on the surface of a pāhoehoe flow and sometimes characterized by feature longitudinal grooves and ridges (Griffiths & Fink, 1992). Ropy fold also provides an example of relating roughness to local emplacement conditions (Anderson & Fink, 1990; Fink & Fletcher, 1978). Field observations of solidified pāhoehoe surfaces and motion pictures of active flows suggest that these features may be interpreted as folds that develop in response to the shortening of the flow surface (Fink & Fletcher, 1978). These features also indicate that slow moving, and low viscosity basalt lava flows forms pāhoehoe surface (Moore et al., 1987; Ramsey & Fink, 1999; Swanson, 1973). Though these features may appear flat and devoid of height changes at the meter and decameter scale, the texture is quite rough when observed at the centimeter scale. Spiny surfaces and ropy folds are very different from 'ā'a lava surfaces, which are composed of piles of jagged blocks and are rough at centimeter to decameter scale (Gaddis et al., 1990; Shepard et al., 2001).

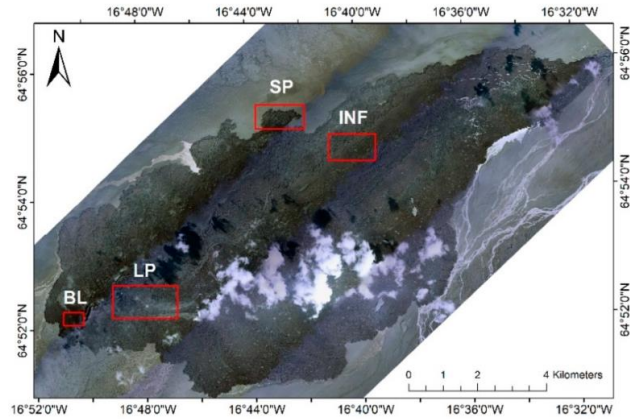
A variety of methods are used to assess surface roughness of various lava surfaces (Gaddis et al., 1990; Shepard et al., 2001; Whelley et al., 2014). Two commonly used are the Root Mean Square (RMS) heights and Hurst exponent (H) (Mallonee et al., 2017; Shepard et al., 2001). RMS represents the standard deviation of the height slope around the mean height (Shepard et al., 2001). RMS is a valuable method for vertical roughness, but it does not include horizontal patterns (Bretar et al., 2013; James, 2019). It has been used to study the roughness of lunar impact melts, and Martian lava flows (Neish et al., 2017).

In this study, we consider using rescaled range analysis, the R/S technique, to derive Hurst exponent (Hurst, 1951). The method offers fast computation and relatively straightforward to adapt with localization in space domains. It is well adapted in the analysis of surface roughness of the material, providing an insight into the stochastic properties of a fractal surface (Candela et al., 2009; Kuang & Chien, 2011; Torres-Argüelles et al., 2010; Wawszczak, 2005). This study provides the first R/S technique applied to a lava flow roughness study. Currently, there is no lava surface roughness study that compares RMS and R/S techniques, but such studies do exist in material science (Babič et al., 2014; Wawszczak, 2005).

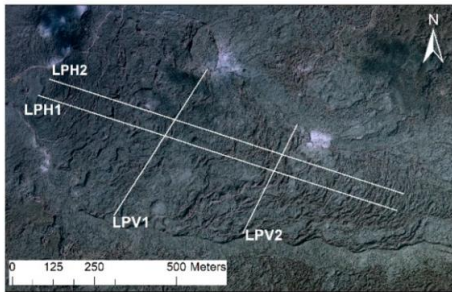
To accurately reflect lava surface roughness, elevations within 360° radius around a point should be considered, rather than only measuring topographic changes along single horizontal direction (James, 2019). Therefore, we use TPI, and the one-dimensional Hurst exponent for assessing the surface roughness of the 2014-2015 lava flow field at Holuhraun from both LiDAR DEM and photogrammetry DEM. The detailed methodology for these techniques is explained in chapter 2.

We examine roughness of the lava surfaces at four sites within the 2014-15 flow field as is depicted in Figure 1.3. These areas were selected because they represent portions of the flow field where the lava surface morphology is well established (Neish et al., 2017; Pedersen et al., 2018). The lava features that are considered are (1) a lava pond, (2) a spiny pāhoehoe, (3) an inflated channel and (4) a rubbly pāhoehoe/'ā'a. The lava pond formed during the first phase of the eruption (Pedersen et al., 2017). Ropy folds preserved on the surface of a lava pond (Figure 1d) are consistent with formation via slow moving, low viscosity lava (Fink & Fletcher, 1978). In the 2014-15 lava field at Holuhraun, the spiny pāhoehoe is characterized by a network of interconnected lobes that in some instances have merged to form inflated sheet-lobes with spinose but coherent surfaces. The millimeter-scale spines on the surface of these flows resemble the texture of 'ā'a, but the flow surfaces

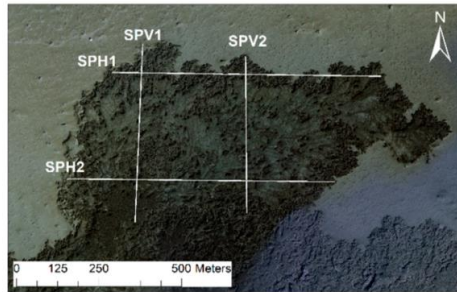
are coherent and continuous (Neish et al., 2017). Spiny pāhoehoe are the dominant flow type along most of the margins of the flow field, with exception of margins in the NE (Neish et al., 2017). Two pre-existing lava channel, the channels of flows 1 and 2, were reactivated towards the end of the second phase and remained active throughout the final phase (Pedersen et al., 2017). These reactivated channels maintained the original lava channel surface morphology as it was elevated via inflation. It is well established that lava inflation is an important component of the emplacement of pāhoehoe. However, emplacement of 'ā'a may also inflate under certain circumstances (Hargitai, 2015). Rubbly pāhoehoe surfaces consist of jumbles of the blocks and plates. This feature likely formed due to sustained auto-brecciation initially of coherent pāhoehoe crust and subsequently of crustal slabs into blocks via mechanical collisions induced by the moving lava. In the 2014-15 lava flow field at Holuhraun the rubbly pāhoehoe are common in the proximity of the source vents.



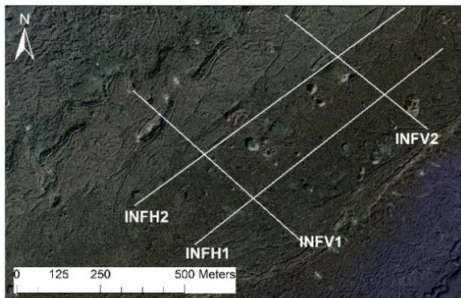
(a)



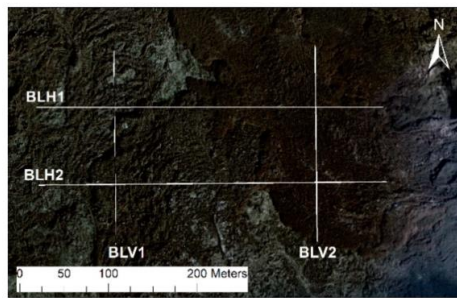
(b)



(c)



(d)



(e)

Figure 1.3 The four different surface morphologies that typify the Holuhraun lava flow field illustrated via aerial photographs (a) location of the selected study areas, (b) Lava pond (LP); (c) spiny pāhoehoe (SP); (d) inflated channel (INF); and (e) blocky pāhoehoe (blocky) surface (BL). The horizontal and vertical profiles are collected for each unit marked with H1, H2, V1, and V2. The original figure presented in Paper III.

1.3 Study area

1.3.1 Geologic setting

Iceland is one of the most active volcanic regions on the Earth due to its situation at the Mid-Atlantic Ridge and the Greenland–Iceland–Faeroe Ridge. Active volcanism in Iceland is primarily constrained to the area known as the Neovolcanic Zone. The Neovolcanic Zone contains three subzones: The North Volcanic Zone (NVZ), the West Volcanic Zone (WVZ), and the East Volcanic Zone (EVZ) (Fig.1.4). Volcanic eruptions occur every four to five years and produce more than 5 km³ magma per century (Thordarson & Höskuldsson, 2008). Volcanism surrounding the Neovolcanic Zone is primarily concentrated in volcanic systems, and these are the main geological features in Iceland. There are 30 volcanic systems, distributed evenly throughout the Neovolcanic Zone. Twenty of the 30 volcanic systems feature a fissure swarm. According to Thordarson & Larsen (2007), 12 of those are well developed and mature swarms, five are of average maturity, and four can be regarded as embryonic. The mature and moderately mature fissure swarms are distinct narrow and elongated strips (5–20 km wide and 50–200 km long) with a high density of tensional cracks, normal faults, and volcanic fissures, whereas embryonic swarms feature one or a few discrete volcanic fissures.

The spreading and subsequent rifting of the crust that occurs at the plate boundary is not a continuous process, in either time or space. It occurs in different rifting episodes that most commonly are narrowed to a single volcanic system at any one time, although near-concurrent activity on two or more systems is known to have occurred (Thordarson & Larsen, 2007; Thordarson & Höskuldsson, 2008). The 2014–2015 lavas at Holuhraun were emplaced on the central part of the floodplain, 6 km north of the Dyngjujökull glacier. This floodplain is primarily covered by glacial and fluvial deposits from Jökulsá á Fjöllum river and has a regional dip of ~1° to the northeast. It features decimeter to meter scale banks, bars and river terraces, which close to the central parts of the river channel may have relief up to 7 m (Pedersen et al., 2017). This eruption has been related to The Bárðarbunga-Veiðivötn volcanic, one of Iceland's largest volcanic systems (Reynolds, et al., 2017).

The central volcano is located within the northwestern part of the Vatnajökull ice cap and features an 8 km by 13 km wide and 500–700 m-deep caldera (Gudmundsson et al., 2016). The eruption history of the Bárðarbunga-Veiðivötn volcanic system in the Holocene is not fully known. However, the eruption frequency is suggested to be ~five eruptions per century (Óladóttir et al., 2011). Tephrochronological studies of ice and soil, along with written records from the last 1000 years have verified 22 eruptions on the southwestern (i.e. Veiðivötn) segment of the fissure swarm in the last 9000 years. The eruption history of the fissure swarm segment to the north is less well constrained, but observations suggest that more than ten eruptions have taken place there during the Holocene (Óladóttir et al., 2011). The most recent pre-2014 lava flow fields in the region are the Holuhraun lavas of 1797 CE (Huluhraun I) and 1867 CE (Huluhraun II). These basaltic lavas have chemical composition identical to that of 2014–15 lavas and chemical signatures that indicate affinity with the Bárðarbunga-Veiðivötn volcanic system (e.g., Hartley & Thordarson, 2013). Holuhraun I erupted from a 1.5 km long fissure 5–6 km north of Dyngjujökull, whereas Holuhraun II erupted just outside the Dyngjujökull glacier. The 2014–15 fissure opened up through the cone row of the Holuhraun I event and thus reactivated a more than 200 year old fissure.

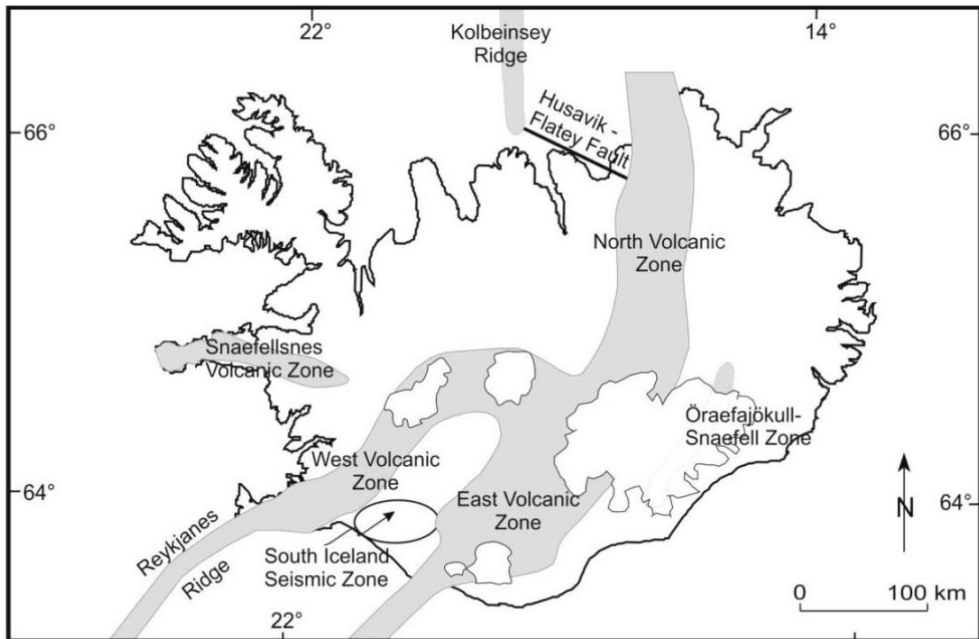


Figure 1.4 Map showing Iceland's Neovolcanic Zone at the junction of the Reykjanes and Kolbeinsey Ridges to the south and north, respectively (Thordarson & Höskuldsson, 2008).

1.3.2 The 2014-2015 Holuhraun eruption

On 16 August 2014, the beginning of intense seismic activity beneath, north and east of the Bárðarbunga central volcano marked the beginning of a significant rifting event (Gudmundsson et al., 2016). On the 16th seismic activity was confined to four areas in at or near the Bárðarbunga volcano: (i) beneath southeast flank of the volcano propagating from the caldera rim to the southeast over a few hours, (ii) beneath the northeast flank of the volcano, (iii) in the region beneath Mt. Kistufell and (iv) beneath the glacier in an area 5-6 km to the east of the volcano (Sigmundsson et al., 2014; Ágústsdóttir et al., 2016; Gudmundsson et al 2016). Over the following 14 days, the seismic activity represented by the easternmost cluster concentrated along a lineament and propagated about 39 km to the northeast, terminating on the floodplain, six km north of the outlet glacier Dyngjujökull (Fig. 1.5). The northern terminus of the seismic activity was directly below the cone row of the Holuhraun I event and was the loci of the minor eruption on 29th August, 2014 as well as the main eruption that began two days later at 4 am (local time) on 31st August. The main eruption was characterized by a high average flux of $\sim 90 \text{ m}^3/\text{s}$, and the maximum discharge rate during the first phase of the eruption is estimated to have been $\geq 350 \text{ m}^3/\text{s}$ (Bonny et al., 2018;; Pedersen et al., 2017), dropping to $\sim 60\text{--}70 \text{ m}^3/\text{s}$ at the end of December, after four months of continuous eruption. The discharge rate continued to decrease from mid- January until the end (Bonny et al., 2018; Coppola et al., 2017). In total, the bulk volume of erupted lava has been estimated to be 1.44 km^3 based on pre and post-eruption topography derived from stereo-photogrammetry and satellite (Bonny et al., 2018). The erupted lava had an olivine tholeiite composition with a minor abundance of

phenocrysts and a groundmass containing silicate glass with plagioclase, clinopyroxene, and olivine microlites (Geiger et al., 2016; Halldórsson et al., 2018).

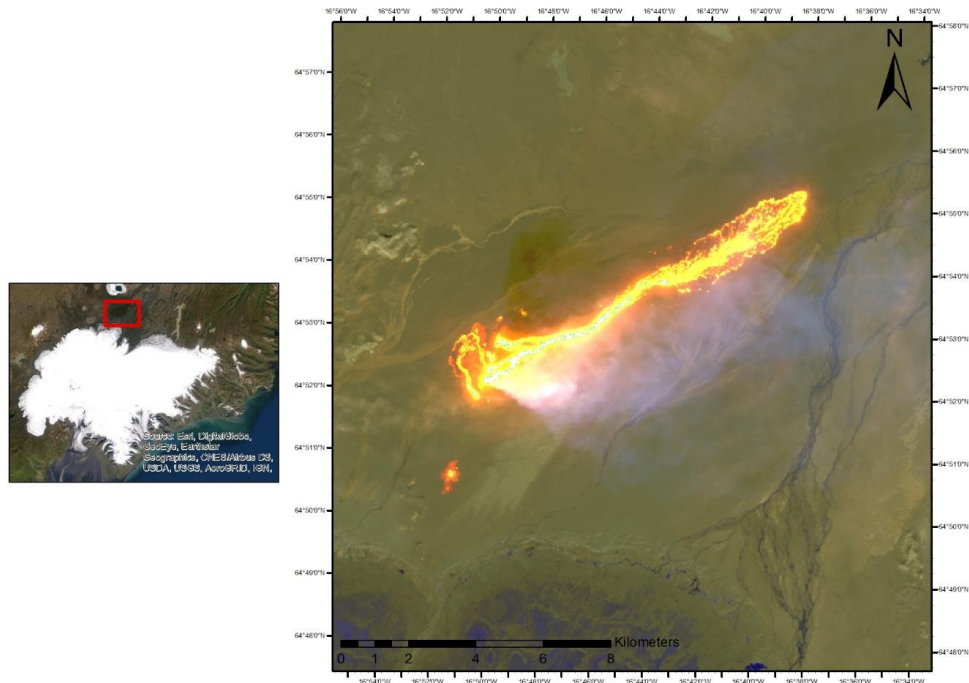


Figure 1.5 The 2014-2015 eruption at Holuhraun on 6th September 2014, acquired from Landsat 8 False color band 7,6,5. The Holuhraun lava field is situated on the flood plain, which is situated south of Askja volcano and north of Dyngjufökull, which is an outlet glacier from the Vatnajökull ice cap.

The 2014-15 eruption at Holuhraun began on 31st August on a 1.8 km long fissure feeding up to 500 m wide, incandescent sheets of slabby pāhoehoe (Pedersen et al., 2017). The eruption is divided into three phases based on the lava field evolution: (i) Phase I from 31st August to mid-October, (ii) Phase II from mid-October to end-November and Phase III from early December to 27th February 2015 (Pedersen et al., 2017). The first phase of the 2014–2015 eruption was dominated by transport of lava through open channels. This phase had a discharge rate of ~560–100 m³/s. The second phase had a discharge rate ranging from 100 to 50 m³/s (Bonny et al., 2018; Pedersen et al., 2017). Throughout this time (mid-October to end-November), a lava pond <1 km² was active at 0.8 km east of the vents. From this time on this lava pond became the main point of lava distribution, controlling the emplacement of the lava flow field (Pedersen et al., 2017). Towards the end of this phase, the lava channel formed during the first phase was reactivated and inflated due to the injection of new lava into the previously active lava (Pedersen et al., 2017). The final phase, from early December to the end of February, had a mean discharge of <50 m³/s. In this phase, the lava transport was confined to internal lava pathways within flow field. Over 19 km² of the flow field was resurfaced via surface breakouts from these internal pathways. It is likely that restrictions within the lava transport system resulted in build up of the lava static pressure within the flow field (Pedersen et al., 2017), such that it could lift

it surface 5-10 m in places. Thus, allowing new lava to be transported to the distal ends of the lava flow field. According to Pedersen et al. (2017), shelly, slabby, rubbly, and spiny pāhoehoe along with formation of 'ā'a were observed within the first week of the eruption. During the first phase and the second phase, 'ā'a was the dominant lava type, and in the final phase, spiny pāhoehoe was the primary lava type (Pedersen et al., 2017). This change from 'ā'a and pāhoehoe in the first and second phases to spiny pāhoehoe in the final phase makes Holuhraun a paired lava field. Rowland and Walker (1990) suggest that a paired lava field is formed due to the decline in the effusion rate over the course of the eruption. The 2014-15 lava flow field was emplaced on a near-flat floodplain, and the chemical composition of the lava was uniform throughout the whole eruption (Halldórsson et al., 2018). This suggests that neither the topography nor the composition was the main factor for the observed changes in flow morphology (Pedersen et al., 2017). The first transition of slabby pāhoehoe to rubbly pāhoehoe to 'ā'a took place downstream of the vent, which is consistent with such changes in other lava producing eruptions and is explained by increased viscosity due to cooling of the lava during transport and emplacement (e.g. Harris and Rowland, 2001), mixing of cold components into the hotter interior (Crisp and Baloga, 1994) and gas loss during lava transport (Cashman et al., 1999).

2 Datasets and Methods

This chapter will describe datasets and methods used for Paper 1,2 and 3. Limitation of datasets and methods will be further discussed in Chapter 4.

2.1 Datasets

The multiple datasets used in this study range from multispectral satellite, SAR satellite, airborne hyperspectral, airborne LiDAR, DEM, aerial photograph, and field data. These datasets were grouped into two based on time of the acquisition, “during the eruption datasets” and “post-eruption datasets.” The details of datasets will be explained in sections 2.1.1 and 2.1.2, respectively.

2.1.1 During the eruption

Landsat 8: In this study, thermal remote sensing observations made during the eruption by Landsat 8. Landsat 8 Level 1 product band 6 (1.56–1.66 μm) and band 10 (10.60–11.19 μm). The selection of band 6 and 10 was made to minimize oversaturation effects on the active lava flow. Acquisition dates are selected according to the availability and quality of data covering the eruption (Table 2.1). The data selected and used has minimum cloud coverage. The data can be downloaded USGS website (<https://earthexplorer.usgs.gov>).

Table 2.1 Product ID and the dates of the Landsat 8 datasets that were used in this study

Product ID	Date
LC82170152014249LGN00	6 September 2014
LC82180142014272LGN00	29 September 2014
LC82180142014288LGN00	15 October 2014
LC80642292014297LGN00	24 October 2014
LC80642302014329LGN00	25 November 2014
LC80652292014336LGN00	2 December 2014
LC80652292014352LGN00	18 December 2014
LC80652292015003LGN00	3 January 2015
LC82180142015035LGN00	4 February 2015

Sentinel 1A: Sentinel 1A satellite radar data from 18 October 2014 was used to derive roughness of lava during the eruption based on backscattering signal. This data can be acquired from the Copernicus website (<https://scihub.copernicus.eu/dhus/#/home>).

Field data for validation: In this study, thermal camera (FLIR) measurement carried out on 2 December 2014, are used since those observations overlap with the satellite data that were used to compare with satellite-derived temperature. Similarly, the theodolite derived lava height measurement made during 3-4 September 2014 were used for comparison with satellite-derived crust thickness calculations.

2.1.2 Post-eruption

Airborne Hyperspectral: Airborne hyperspectral data were acquired on 4 September 2015 between 16.56 and 17.58 (local time) with an AisaFENIX sensor (Specim, Spectral Imaging Ltd, <http://www.specim.fi>) onboard a NERC Airborne Research Facility (Natural Environment Research Council Airborne Research Facility <http://www.bas.ac.uk/nerc-arf>) aircraft. The hyperspectral data contain 622 bands with a spectral range from $\sim 0.4 \mu\text{m}$ to $2.5 \mu\text{m}$ (break at $\sim 0.97 \mu\text{m}$). In total, eight flights were acquired over the 2014-15 lava flow field at Holuhraun during this period, and acquisition flight altitude was 2.4 km (Figure 2.1a) and pixel size 3.5 m. The data are delivered as level 1b ENVI BIL format files, which means that radiometric calibration algorithms have been applied and navigation information have been synchronized to the image data (Figure 2.1b). In this study, the data used was a subset focused on the area around the eruptive fissures vent (Figure 2.1c).

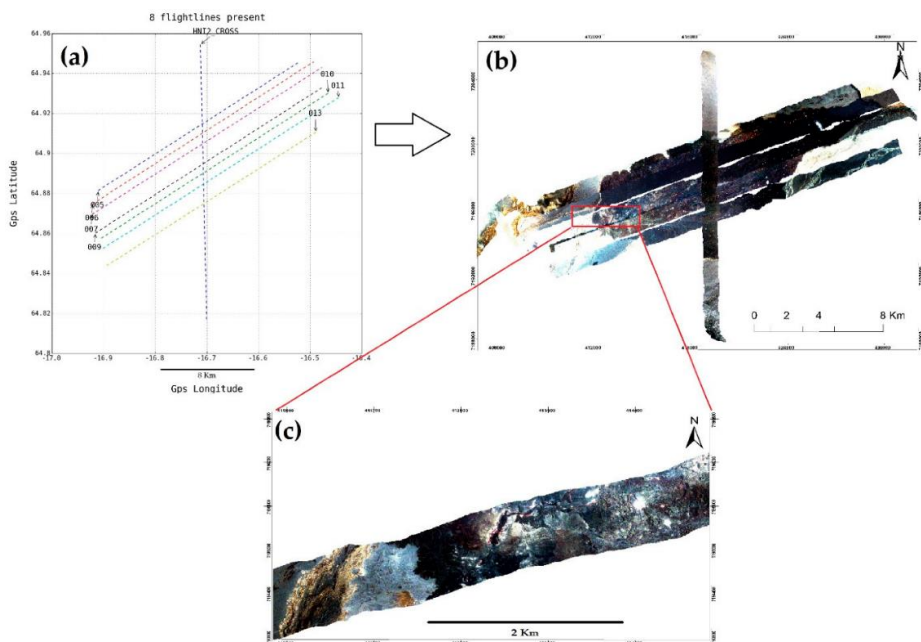


Figure 2.1 Map showing line acquisition of FENIX hyperspectral image in the Holuhraun lava field; (b) Image mosaic from eight FENIX lines collected during the campaign (red box shows the image subset location); (c) Image subset of the focusing study area in the eruptive fissure vent of Holuhraun. The original figure presented in Paper II.

Airborne LiDAR: LiDAR data was collected by the Natural Environment Research Council (NERC). It was acquired on September 4, 2015, and we processed the DEM based on the LiDAR point cloud with 1 m spatial and vertical resolution (mean error of 4 to 5 cm depending on the flight line) over most of the lava flow. Eight flight lines were made over the 2014-15 lava flow-field at Holuhraun: seven of these are parallel and aligned with the long axis of the field (from the vent to the hot springs region in the northeast end of the lava field) while the eighth is transverse and crosses all the others. The LiDAR, therefore,

does not cover the entirety of the flow-field. Furthermore, clouds obscured parts of the lava and created gaps in the data (Figure 2.2).

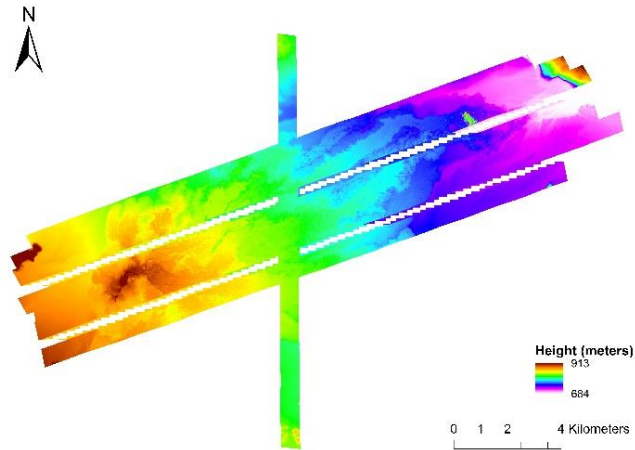


Figure 2.2 The LiDAR DEM acquired on 4 September 2015, with the 1-meter pixel spatial resolution. The LiDAR does not cover the entirety of the flow-field and has a gap in between eight lines.

Very high-resolution aerial photograph: Very high-resolution aerial photographs of the lava field (Fig 2.3a) from Loftmyndir ehf (<http://www.loftmyndir.is/>) acquired on 30 August 2015 are used in this study. Clouds obscured interior portion of the 2014–2015 lava flow-field at Holuhraun (Fig. 2.3a). This dataset, along with a collection of field photographs, was used for comparison and validation of the unmixing results. This aerial photograph has a spatial resolution of 0.5 m. Photogrammetry-derived DEM based on this data with spatial resolution 5 m was used. The DEM is used to deriving surface roughness (Fig 2.3b).

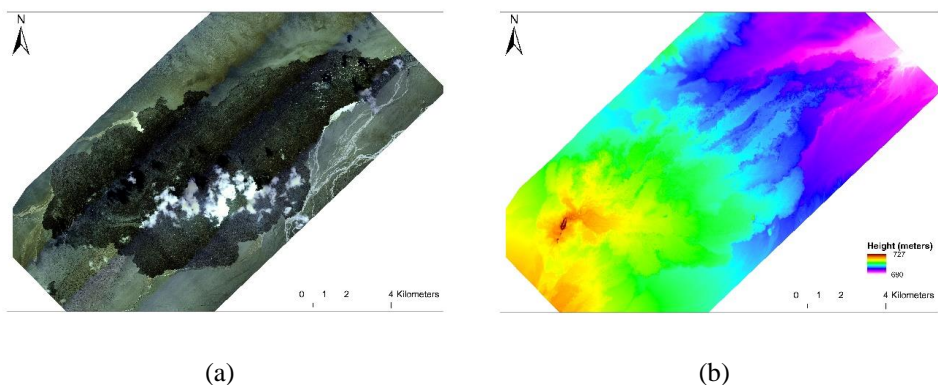


Figure 2.3 (a) Aerial photograph of the Holuhraun lava field, the spatial resolution of this image is 0.5 m. The white patch in the image is cloud covering the area. (b) Photogrammetry-derived DEM based on an aerial photographs with spatial resolution 5 m.

2.2 Methods

2.2.1 Deriving thermal properties of lava flow during the eruption

The processing workflow to derive the temperature of the lava surface, identify different thermal domains, estimation of radiant flux, and the crust thickness model of the lava flow is illustrated in Fig 2.4.

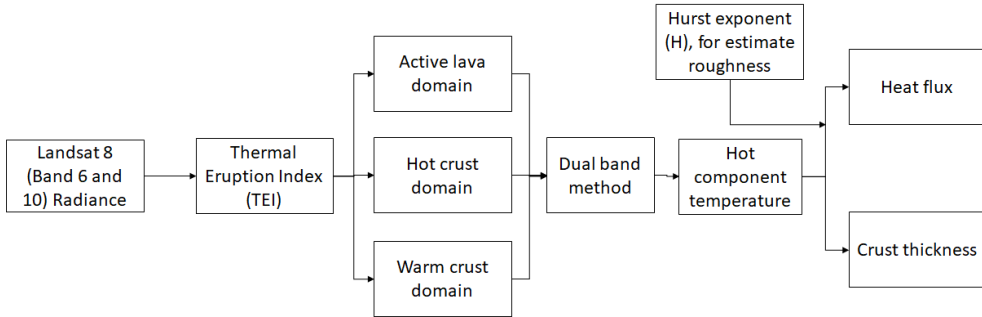


Figure 2.4 The workflow used for processing derive thermal properties of the lava flow field from Landsat 8.

Thermal Eruption Index (TEI): TEI was developed by using the SWIR and the TIR bands from Landsat 8. The method uses the sensitivity difference between SWIR (band 6) and TIR (band 10) to differentiate pixel hot spots. The objective of TEI is to provide a new variant for a hotspot thermal index, by using data from the medium spatial resolution satellite Landsat 8. TEI is based on the principle that the SWIR spectral radiance (R_{SWIR}) from the crust will be less than the TIR spectral radiance (R_{TIR}) and vice versa, on the active lava ($R_{SWIR} > R_{TIR}$). The active lava pixels are emitting more spectral radiance in both band 6 and band 10; at the same time, the crust pixels are emitting more spectral radiance in TIR. Therefore, TEI has higher values where there is active lava, than where there is a stagnant crust. This index uses the square of the TIR spectral radiance and the maximum of the SWIR spectral radiance to differentiate between the thermal domains. TEI is expressed as,

$$TEI = \frac{R_{SWIR} - \frac{(R_{TIR})^2}{10 R_{SWIR MAX}}}{R_{SWIR} + \frac{(R_{TIR})^2}{10 R_{SWIR MAX}}} \frac{(R_{TIR})^2}{\left(\frac{R_{SWIR MAX}}{3}\right)^2} \quad (3)$$

where R_{SWIR} , R_{TIR} are the pixel corrected spectral radiances detected in the band 6 and band 10, respectively and $R_{SWIR MAX}$ are the maximum spectral radiances detected in band 6. The purpose of TEI is mainly of two kinds; (1) detect a threshold to differentiate between different thermal domains of the lava field and (2) to estimate subpixel temperature within thermal domains to differentiate between types of lava surface.

Dual-band method: In this study, the dual-band method was applied to automatically calculate the hot component temperature within the region defined by the hotspot threshold ($TEI > 0.10$). By use of simple two thermal component scenarios, with T_h as the

temperature of the lava surface and, T_c as temperature surrounding the lava. T_c was set equal to the lowest brightness temperature detected in TIR data, for each thermal domain considered, with , $T_c = 25$ C in the surrounding of warm crust, , $T_c = 50$ C in the surrounding of hot crust, and , $T_c = 85$ C in the active lava. These assumptions is suitable in situations where different thermal domains (active lava and crust) within the lava flow are clearly separable. Pixel portion (p) was solved by iterating for, T_h , by equation (1) and (2).

Radiant flux estimation: Radiation is the most important direct heat flux to estimate. For rough lava surface (aa and brecciated surface), not all the radiation can escape from the lava surface because of surface scattering. Therefore, in this study, the Hurst exponent (H) is introduced to describe the lava surface roughness; thus the actual radiation emitted is reduced due to the fractal model (this technique will be explained in detail on section 2.2.3 and Appendix A). In Paper I, we estimate H from a radar backscattering profiles from Sentinel 1A VH polarization data that have been calibrated, speckle filtered, and terrain corrected. Here, we assume that surface roughness reflects the lava thermal domain in such a way that active lava (moving incandescent lava) is smooth, the hot crust is rough, and the warm crust domain is very rough. We assume that H has a strong tendency to cluster around 0.5 from topography profiles (Shepard et al., 2001). Therefore, we simply adjust the H value on radar backscattering profiles by multiplying it with 0.5. although there is no reference related to this, we did this in an empirical way. Hurst exponent range from 0 to 1, where a higher H tends to have a relatively smoother surface (Babič et al., 2014; Candela et al., 2009; De Assis, 2015; Fargier et al., 2018; Kuang & Chien, 2011; Martino et al., 2008; Sanchez-Ortiz et al., 2015). Following this model, the radiant flux for each pixel that contains lava can be estimated as

$$\Phi_{\text{rad}} = \epsilon \sigma H A T_e^4 \quad (4)$$

where Φ_{rad} is the radiant flux (W), σ is the Stefan–Boltzmann constant ($5.67 \times 10^{-8} \text{ W m}^{-2} \text{ K}^{-4}$), and A is the Landsat 8 pixel area, which is 900 m^2 . In this approach, we use the effective temperature model (T_e), which is the average surface temperature of lava for the two thermal components present on the lava flow surface (Ferrucci & Hirn, 2016; Pieri et al., 1990).

Crust thickness model: The crust thickness Δh is calculated by assuming that the density of conductive heat flux across the surface of a crust is equal to the total densities of the radiative and convective heat flux leaving the surface of lava (Oppenheimer et al., 1993; Oppenheimer, 1991), so that

$$\Delta h = -k \frac{\Delta T}{M_{\text{rad}} + M_{\text{conv}}} \quad (5)$$

where Δh is the crust thickness (m), M_{rad} and M_{conv} are radiative and convective flux densities (W m^{-2}), respectively, k is the thermal conductivity, where we use $2.5 \text{ Wm}^{-1} \text{ K}^{-1}$ (Lombardo et al., 2011; Reynolds et al., 2017), and ΔT is the temperature of the lava flow interior. In this study, the interior temperature of 1128 °C (for lava outside vent) and 1200 °C (for lava surrounding vent) were used; these values were selected according to thermocouple measurements for freshly exposed patches of lava in the flow field on 19 and 20 November 2014 (Kolzenburg et al., 2017).

2.2.2 Discriminating lava surface

In this study, a spectral unmixing technique was applied to the airborne hyperspectral data to discriminate between lava surfaces. The processing workflow towards unmixing and generating abundance consists of four steps: (1) Atmospheric correction to retrieve surface reflectance; (2) Data masking, geo-correction, reprojection, and resampling; (3) An endmember selection algorithm was adopted to select the endmembers; then a linear spectral mixture analysis method was employed to retrieve the abundance (Fig 2.5).

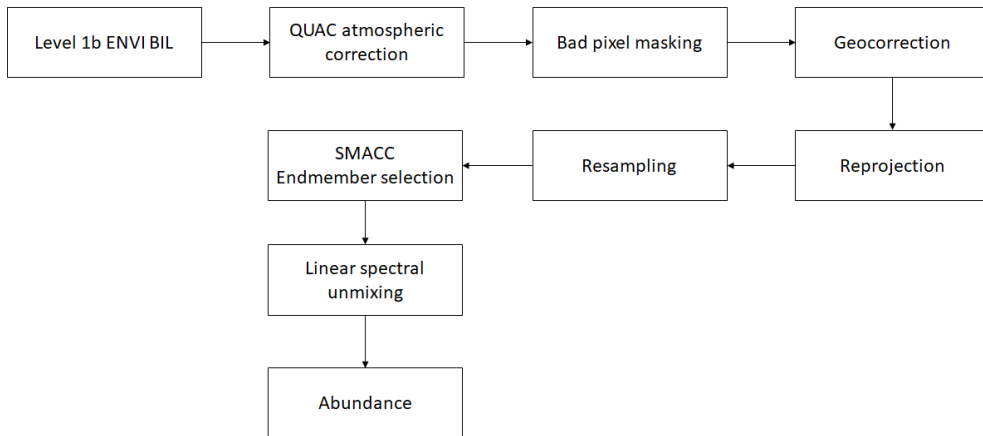


Figure 2.5 The workflow processing used to derive an abundance map from the FENIX hyperspectral data.

Atmospheric Correction: In this study, the data were atmospherically corrected using the quick atmospheric correction (QUAC) algorithm (Bernstein et al., 2005; Bernstein, 2012), since we had no prior knowledge to perform empirical calibration (Karpouzli & Malthus, 2003; Kizel et al., 2018). QUAC is an in-scene approach, requiring only an approximate specification of sensor band locations (i.e., central wavelengths) and their radiometric calibration; no additional metadata is required (Bernstein, 2012). QUAC does not involve first principles radiative transfer calculations, and therefore it is significantly faster than physics-based methods; however, it is also more approximate (Bernstein, 2012).

Data Masking, Geocorrection, Reprojection, and Resampling: Airborne Processing Library (APL) software was used in this study (Warren et al., 2014). The first step of the APL processing is to apply the mask of bad channels to atmospherically corrected data, creating a new file with bad channels set to zero. The next step uses the navigation file, the view vector file, and the digital elevation file (DEM) to calculate the ground position for each pixel, it is subsequently changed to the UTM projection (Universal Transverse Mercator) Zone 28N (Warren et al., 2014). A satellite-based ASTER sensor was used for the DEM. In the final step, we resampled the output pixel size to ~3.5 m according to the height above ground level (AGL) that is given by the theoretical pixel size chart that can be found on <https://nerc-arf-dan.pml.ac.uk/trac/wiki/Processing/PixelSize>.

Endmembers Selection: The sequential maximum angle convex cone (SMACC) algorithm was employed (Gruninger et al., 2004) to identify spectral image endmembers. Endmembers are spectra that represent pure surface materials in a spectral image. The extreme points were used to determine a convex cone, which defined the first endmember. A constrained oblique projection was applied to the existing cone to derive the next endmember. The cone was then increased to include a new endmember (Gruninger et al., 2004; Zhang et al., 2014). This process was repeated until a projection derived an endmember that already existed within the convex cone, or until a specified number of endmembers was satisfied (Gruninger et al., 2004). When implemented with SMACC, the output endmember number was set as 5, 10, 15, 20, and 30, respectively. Endmembers could be identified easily from the 15 endmembers. Then, the selected 15 endmembers were used to derive the abundance.

Linear Spectral Mixture Analysis: The linear spectral mixture analysis (LSMA) approach was adopted to calculate the abundance of endmembers for each pixel. LSMA assumes that the spectrum measured by a sensor is a linear combination of the spectra of all components (endmembers) within the pixel, and the spectral proportions of the endmembers (i.e., their abundance) reflect the proportion of area covered by distinct features on the ground (Adams et al., 1995; X. Zhang et al., 2014). The general equation for linear spectral mixing can be expressed as:

$$R_{ij,\lambda} = \sum_{n=1}^N p_{ij,n} R_{n,\lambda} + E_{ij,\lambda} \quad (6)$$

where $R_{ij,\lambda}$ is the measured reflectance at wavelength λ for pixel i,j , where i is the column pixel number, and j is the line pixel number; $p_{ij,n}$ is the abundance of endmembers n contributing to the image spectrum of pixel ij ; N is the total number of endmembers; $R_{n,\lambda}$ is the reflectance of endmember n at wavelength λ ; and $E_{ij,\lambda}$ is the error at wavelength λ of the fit of the N spectral endmembers. The abundance $p_{ij,n}$ can be solved using a least-square method with fully constrained unmixing. Fully constrained unmixing means that the sum of the endmember fractional (abundance) values for each pixel must equal unity, which requires a complete set of endmembers. In this study, fully constrained LSMA was applied to the FENIX image to obtain the abundance result and both SMACC and LSMA were executed by ENVI 5.3 and IDL 8.5 language programming.

2.2.3 Deriving roughness properties

The methodology adopted for the assessment of the roughness is given in sequential a manner in Figure 2.6. In this study, we use the Topographic Position Index (TPI) to describe roughness pattern and one-dimensional Hurst exponent approaches to assess the roughness on the 2014-2015 Holuhraun lava flows from both photogrammetry DEM and LiDAR DEM. Finally, we determined the roughness properties for four different regions on the lava field from Figure 1.3.

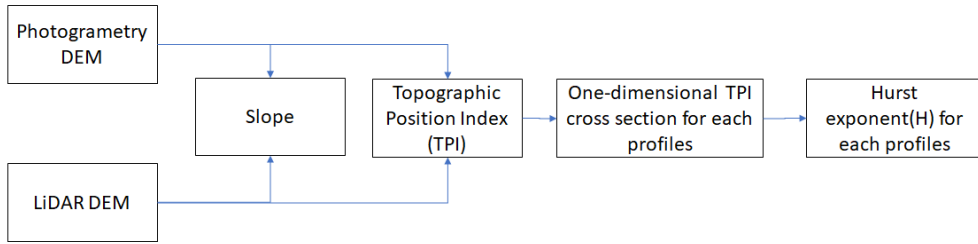


Figure 2.6 The workflow processing used to assess roughness from the lava flow from LiDAR and photogrammetry

Topographic Position Index (TPI): The topographic position index (TPI) was introduced by Guisan et al. (1999) and was further developed by Jennes (2006). Mokarram et al. (2015) were used TPI for landform classification, a recent study from James (2019) was derived roughness of lava flow in the Earth and Mars based on TPI. TPI compares the elevation of each cell in a DEM to the mean elevation of a specified neighborhood around that cell. Mean elevation is subtracted from the elevation value at the center.

$$TPI = \frac{C_0 - \bar{C}}{\sigma} \quad (7)$$

where C_0 is the elevation of the model point under evaluation, \bar{C} is the mean elevation cell of the grid, σ is the standard deviation of elevation in the neighborhood. TPI indicates that the cell is higher in elevation (or more steeply sloping) than the average of its neighbors up to a specified distance away, whereas a negative one shows the cell is lower than the average surrounding elevations (Fig 2.7) (Jennes, 2006). The cell is classified by the magnitude of the difference in elevation along with the slope value. The cell neighborhood can be adjusted to produce varying TPI values for different scales, thus changing the scale of roughness being measured (Jennes, 2006). This extension was initially created for use in geomorphology- and hydrology-based projects (Jennes, 2006) but may be useful in assessing the topographic characteristics of a lava flow surface by building a catalog of features present at each scale (James, 2019). In this study, we use a rectangular TPI with a 3x3 neighborhood size for both LiDAR DEM and photogrammetry DEM.

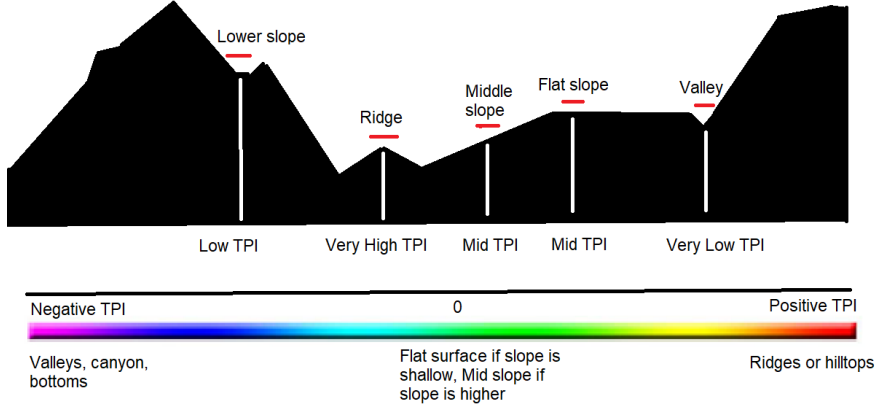


Figure 2.7 Illustration of the topographic position index (TPI) value in the topography (Jennes, 2006). The original figure presented in Paper III.

Hurst exponent: The Hurst exponent is derived using rescaled range analysis (R/S) for the Radar backscattering profiles (Paper I) and TPI profiles (Paper III). This technique originally developed by Hurst (1951) to investigate long term capacity of water reservoirs. R/S has the advantage of fast computation with localization in space domains and is well adapted in the analysis of surface roughness, providing an insight into the stochastic properties of a fractal surface (Candela et al., 2009; Kuang & Chien, 2011; Torres-Argüelles et al., 2010; Wawszczak, 2005). In R/S, a profile of the spatial series is constructed by averaging over the values of a newer series made of accumulated deviations from the arithmetic mean. With the profile, the method forms a rescaled range by standardizing each range by their corresponding standard deviation. For many sub spatial points τ , the rescaled range is given by

$$(R/S)_\tau \sim \tau^H \quad (8)$$

Then, a least-squares regression on logarithms of each side is applied, so that

$$\log(R/S)_\tau = H \log \tau \quad (9)$$

where H is the Hurst exponent, for smaller τ , the exponent is biased and a larger value of τ is recommended (Babič et al., 2014; Couillard & Davison, 2005). The details for deriving equation (8) and equation (9) is described in Appendix A. The Hurst exponent value has a range $0 < H < 1$. In this study, we consider higher Hurst exponent indicates a relatively smoother surface or profile (Candela et al., 2009; De Assis, 2015; Kuang & Chien, 2011; Martinez et al., 2014; Torres-Argüelles et al., 2010; Wawszczak, 2005). There are several ways and techniques to interpret and derive H , which will be covered in Chapter 4. There are also several naming for H in the literature which have similar or analogous meanings and are often confused with one another, among them the Hurst exponent (Alvarez-Ramirez et al., 2008; De Assis, 2015; Jordan et al., 2017; Shepard et al., 2001), Hurst coefficient (Kuang & Chien, 2011; Martino et al., 2008; Tubman & Crane, 1995) and Hurst parameter (Babič et al., 2014). In order to maintain consistency, in this dissertation, we will refer to H as the Hurst exponent.

3 Summary of papers

3.1 Paper I

Paper I, *New Insights for Detecting and Deriving Thermal Properties of Lava Flow Using Infrared Satellite during 2014–2015 Effusive Eruption at Holuhraun, Iceland*. This study presented a new approach based on infrared satellite images to derive thermal properties within the lava field during eruption and then compare the results with field measurement during the 2014–2015 eruption at Holuhraun. We develop a new spectral index for Landsat 8, named the thermal eruption index (TEI), based on the SWIR and TIR bands (bands 6 and 10). The purpose of the TEI consists mainly of two parts: (1) be a threshold for differentiating between different thermal domains; and (2) applying a dual-band method (Dozier, 1981; Harris et al., 1997; Lombardo et al., 2004) to estimate subpixel temperature within thermal domains and differentiating between the types of lava surface. The active lava surface has thermal domain complexity and contains more than one thermal component, here we use two thermal component scenarios, with T_h as the temperature of lava surface and T_c as temperature surrounding the lava for different thermal domains. We also discuss the effect of lava surface roughness using the Hurst exponent (H) on Φ_{rad} and Δh .

3.1.1 Main highlights of paper I

- Introduce a new spectral index called the thermal eruption index (TEI) based on the SWIR and TIR bands, allowing us to differentiate thermal domains within the lava flow field.
- TEI detects hotspots with $\text{TEI} > 0.10$: this value provides encouragement that the TEI method yields robust estimates.
- Apply dual-band technique to determine the subpixel temperature (T_h) of the lava
- Lava surface roughness effects are accounted for by using the Hurst exponent (H) (derived from Sentinel 1 radar backscattering profiles) for deriving the radiant flux and crust thickness.
- The higher H (smoother surface) generates thinner crust; meanwhile, the lower H (rough surface) generates a thicker crust.
- The total radiant flux peak is underestimated (~ 8 GW) compared to other studies (~ 25 GW), although the trend shows good agreement with both field observation and other studies.
- The proposed techniques were successfully applied to Landsat 8 on SWIR and TIR datasets from the 2014–2015 Holuhraun eruptions.
- In future work, the proposed methods will be applied to other satellite/airborne datasets that have both SWIR and TIR band and consider an alternative method to determine H (e.g., airborne LiDAR and terrestrial laser scanning).

3.2 Paper II

Paper II, *The 2014–2015 Lava Flow Field at Holuhraun, Iceland: Using Airborne Hyperspectral Remote Sensing for Discriminating the Lava Surface*. This paper was focused on both endmember extraction and estimation of fractional abundances of the lava field products in the 2014–2015 lava flow field at Holuhraun. The aim of this study is to retrieve the main lava surface type contributing to the signal recorded by airborne hyperspectral at the very top surface of the 2014-2015 lava flow field at Holuhraun. For this purpose, an airborne hyperspectral image with an AisaFENIX sensor onboard a NERC (Natural Environment Research Council Airborne Research Facility) campaign was acquired at the flow field after the eruption, and for the sub-pixel analysis, we used the sequential maximum angle convex cone (SMACC) algorithm to identify the spectral image endmembers while the LSMA method was employed to retrieve the abundances. Our approach was narrowed to the eruptive fissure vent part since it is considered to have a more diverse surface. The resulting abundances from the linear spectral mixture analysis (LSMA) method were both quantitatively and qualitatively compared with the spectral indices' technique, aerial and field photographs, respectively.

3.2.1 Main highlights of paper II

- In total, 15 spectral endmembers and their abundances were acquired. The first endmember was the brightest pixel, which represented saturated incandescent lava.
- These 15 endmembers were grouped into six groups (basalt, oxidized surface, sulfate mineral, hot material, water, and noise) based on the shape of the endmembers since the amplitude varies due to illumination conditions, spectral variability, and topography.
- We, thus, obtained the respective abundances from each endmember group using fully constrained linear spectral mixture analysis (LSMA).
- The oxidized surface and water abundances indicate a good correlation with the reference indices. This suggests that both oxidation and water generated from a spectral index are properly validated. Meanwhile, basalt shows a low correlation with the mafic index suggesting that the estimates of the basalt surface from the unmixing technique are an overestimation since the basalt abundance shows the older lava flows as mafic with a relatively high fraction compared to the mafic index that only showed for fresh lava flow. This being due to a full spectrum of hyperspectral can easily differentiate between basalt surface and non-basalt.
- A Combination of SMACC and LSMA methods offers an optimum and a fast selection for volcanic product segregation. However, ground-truthing spectra are recommended for future work.
- In a future study due to the complementary nature of the reflective (VIS-SWIR) and emissive (TIR) spectral regions, synergistic use of airborne data from both FENIX (VIS-SWIR) and OWL (TIR) could give great potential for lava discrimination. This might significantly improve our understanding of physical lava surface properties determination.

3.3 Paper III

Paper III, *Lava Surface Roughness on 2014-2015 Lava Flow Field at Holuhraun, Iceland derived from Airborne LiDAR and photogrammetry*. In this paper, lava surface roughness

in the 2014-2015 lava flow field at Holuhraun was quantified based on LiDAR DEM and airborne photogrammetry DEM. Roughness properties were determined for four different surfaces (Lava pond; spiny pāhoehoe; inflated channel; and blocky surface) that exhibit well-studied known lava flow morphology at Holuhraun. This study used Topographic Position Index (TPI) and One-dimensional Hurst exponent approaches to determine roughness on the 2014-2015 Holuhraun lava flows for both photogrammetry DEM and LiDAR DEM. TPI compares the elevation of each cell in a DEM to the mean elevation of a specified neighborhood around that cell. Mean elevation is subtracted from the elevation value at the center. One-dimensional TPI was acquired in perpendicular directions in order to avoid directional bias (Hamilton et al., 2018; Neish et al., 2017). The Hurst exponent is derived using a rescaled range analysis (R/S technique) for the TPI profiles. Hurst exponents range from 0 to 1, where a higher Hurst exponent tends to have relatively smoother profiles.

3.3.1 Main highlights of paper III

- Both the TPI and One-dimensional Hurst Exponent can distinguish end member flow roughness.
- TPI patterns show the intermediate TPI values correspond to a small slope indicating a flat and smooth surface which found on spiny lava and inflated channel.
- Lava pond is characterized by low to high TPI values and forms a wave-like pattern. Meanwhile, irregular transitions patterns from low to high TPI values indicate a rough surface that is found on blocky surfaces, i.e. rubbly pāhoehoe to 'ā'a flows and lobes and their margins. These lobes and margins may give the impression of having similar roughness as the "rough" surface on meters scale since this is an "apparent" roughness, On centimeters scale these multitudes of lobes feature coherent and smooth surfaces because they are pāhoehoe.
- Quantitative measures of surface roughness of lava features fall within the H range of 0.30 ± 0.05 (Blocky) to 0.76 ± 0.04 (Inflated lava). This indicates that the lower H tends to have a relatively rougher surface. Meanwhile for the higher H, Indicating relatively smoother surface at large scales relative to small scales.
- In general, the Hurst exponent values in the 2014-2015 lava field at Holuhraun has a strong tendency in 0.5, which has good agreement with early study for geological surface roughness.
- Neighborhood size is a critical component for TPI to quantify the roughness. Small neighborhoods capture small and local features and valleys, while large neighborhoods capture larger-scale features.
- We consider there are at least two factors that affected Hurst exponent values: (1) pixel size and (2) the profile length.
- We recommend in a future study to build series of profiles that are rotated by some number of degrees to capture a wider range of directions around the surface area of interest. The integration of multimodal remote sensing datasets and field measurement also could improve in achieving accurate estimation surface roughness of lava flow in the future.

4 Discussion and Limitations

This chapter will discuss the limitations and recommendations for datasets and methods used in the study.

4.1 Deriving thermal properties

In Paper I, we used TEI to automatically detect thermal domains of the lava field, the signal obtained from Landsat 8 SWIR and TIR data. The hotspot region is defined by $TEI > 0.10$. This method provides encouragement that the TEI yields robust estimates of hotspot anomalies within lava fields during an eruption. Since TEI is determined by empirical technique, it does not directly discriminate between the different types of the hotspot domains that are observed. As a result, the interpretation can be difficult, as the active lava, hot crust and warm crust could be mistaken for eruptive activity. Therefore, accurate lava evolution or knowledge of the area under investigation where the hotspots occur becomes critical for determining the origin of TEI anomaly.

On the other hand, differentiating between thermal domains offers new possibilities to use different T_c setting for each domain to derive subpixel temperature for the dual-band method. However, as explained by Lombardo et al. (2004), the dual-band method provides a rough approximation to the thermal model when only two infrared bands are available. Therefore, we recommend further improvement by using satellite sensors that have more than two infrared bands such as ASTER, EO-1 Hyperion (Abrams et al., 2013; Murphy et al., 2011). This offer possibility to use more than two thermal components for the analysis to improve thermal approximation (Lombardo & Buongiorno, 2006).

4.2 Hyperspectral unmixing

The methods for discriminating the lava surface (Paper II) were only tested on a subset area of the lava field (around vent). In order to apply the method on the entire lava flow area a challenge rises due to three reasons; (1) The high spatial heterogeneity typically gives rise to mixed pixels containing multiple materials and it will increase the number of endmembers detected by SMACC (Grüniger et al., 2004). (2) Different illumination occurs within the different flight lines for the entire lava flow (Figure 2.1b) since the data acquisition time is acquired between 16.56 and 17.58 local times which results in acquisition during very low sun angle. The solution to this problem can be approached by collecting ground truth spectra, extensive calibration, and atmospheric correction using the simultaneous and constrained calibration of multiple hyperspectral images through a new generalized empirical line model purposed by Kizel et al. (2018). (3) The computation time to perform unmixing also must be considered for the entire lava flow field since the area is relatively large (84 km^2) and taking into account that hyperspectral data contains 622 channels with a 3.5-meter spatial resolution. In order to process a data set of this size, we

would need to consider using high-performance computing (HPC) and machine learning (ML) in the future.

Paper II demonstrate that hyperspectral VIS-SWIR image is effective for discrimination of mafic minerals, oxidation, sulfate etc. However, not all the minerals and surface types are always mapped uniquely with VIS-SWIR hyperspectral data. A typical surface such as rock-forming minerals associated with unaltered rocks and alteration minerals associated with altered rocks can be identified with TIR (Thermal Infrared) data (Riley & Hecker, 2013; Schlerf et al., 2012; Vaughan et al., 2003). Image processing methods that have become standard for hyperspectral VNIR/SWIR data analysis also work for hyperspectral TIR data (Vaughan et al., 2003). Pixel classification based on spectral variability within the scene and mineral libraries for matching spectral emissivity features can be used for TIR-derived mineral maps using SEBASS hyperspectral TIR image data (Vaughan et al., 2003). Hyperspectral TIR instruments operational for airborne surveys are also available in the NERC Airborne Research Facility with a Specim AisaOWL sensor (Schlerf et al., 2012). Synergistic use of airborne data from both FENIX (VIS-SWIR) and OWL (TIR) allows great potential for lava discrimination in a future study due to the complementary nature of the reflective (VIS-SWIR) and emissive (TIR) spectral regions. This might significantly improve our understanding of physical lava surface properties. Specifically, VIS-SWIR imaging spectrometers can discriminate surface materials and TIR data acquisitions can help to identify the thermal characteristics of different materials. For instance, combining emissivity spectra with reflectance spectra in a mixing model would improve discriminating lava surfaces (Ball et al., 2008; Harris, 2013b; Ramsey et al., 2016).

4.3 Roughness indicator

Since Hurst exponent is widely used in scientific fields other than earth science, there are a couple of methods available for estimates Hurst exponent. The R/S method is commonly perceived as the most suitable for its estimation because it presents the relationship between irregular (singular) rescaled ranges, signal value and their local statistical properties relative to the scale factor. There is ample evidence for the popularity of this method in various disciplines, like finance, material science, water, signal processing, earth science, etc. (Alvarez-Ramirez et al., 2008; Couillard & Davison, 2005; Fargier et al., 2018; Hamed, 2007; Raoufi & Hosseinpanahi, 2012). However, some studies suggest that the roughness–length method (R-L) (Gong et al., 2016; Malinverno, 1990; Wawszczak, 2005) is the most appropriate for describing the roughness of surfaces. That method is descended from RMS profile analysis (Shepard et al., 2001) and calculates a surface roughness parameter. The R–L method permits the description of profiles as the relationships between local statistical properties (standard deviation) versus the scale factor (length of the part of the profile).

There are also various techniques to estimate H based on moving average (DMA) (Alessio et al., 2002), wavelets and wavelet transform (Alessio et al., 2002; De Assis, 2015), RMS (Neish et al., 2017; Shepard et al., 2001), variogram (Babič et al., 2014; Wawszczak, 2005), etc. The variogram is similar to the roughness–length method because it uses variance for the description of the average trend versus the length of windows (lags). The variogram method is most popular in earth sciences or geomorphology and is very useful

for surface approximations in the case of sparse datasets (Babič et al., 2014; Wawszczak, 2005).

The problem with these methods are that they are based on different bases (aggregation, variance, wavelet transformation, etc.), which in turn lead to different values (Babič et al., 2014; De Assis, 2015; Kuang & Chien, 2011; Martino et al., 2008; Wawszczak, 2005). However, each method has certain advantages and limitations in regard to the captured profile series. Some methods are better for large samples, some for smaller ones (Babič et al., 2014; Hamed, 2007; Wawszczak, 2005). There are also studies that state there is no precise method by which to calculate the Hurst parameter accurately and that it can only be estimated (Babič et al., 2014; Hamed, 2007; Wawszczak, 2005).

These differences lead to a different point of view when interpreting H , especially in the case of roughness. In material science and signal processing, commonly, higher values of the Hurst exponent suggest a relatively smoother surface/profile (Babič et al., 2014; De Assis, 2015; Fargier et al., 2018; Martinez et al., 2014; Sanchez-Ortiz et al., 2015). Meanwhile, when looking at lava flow roughness, H can be defined as how roughness change with scale. That means a Hurst exponent close to zero indicates that the surface becomes smooth as the scale increases. A Hurst exponent close to one indicates that the surface maintains its roughness (or smoothness) as the scale increases. From our point of view, both interpretations have a strong argument because these techniques, scale matters. Despite similar theoretical foundations, the practical implementation of these methods is dependent on the physical nature of the investigated material. In order for future investigation of lava flow roughness, a comparison study of H estimation by use of different techniques (other than RMS) is recommended. This would bridge the knowledge gap between different scientific fields.

5 Concluding remarks

In this thesis, several remote sensing techniques to derive physical properties of the 2014-2015 Holuhraun lava flow field are explored. Data obtained during the eruption, infrared remote sensing based on Landsat 8 satellite images, was used to develop a new spectral index called the thermal eruption index (TEI) based on the SWIR and TIR bands that allow differentiating between thermal domains within the lava flow field. TEI detects hotspots with $TEI > 0.10$: this value indicates that the TEI method yields robust estimates of hotspot anomalies during the eruption. Two main thermal domains were distinguished within the lava flow field. The first is the active lava domain, which is characterized by high TEI (0.51). The second is the crust domain surrounding active lava, characterized by TEI below the active lava domain but exceeding the hotspot threshold (0.10–0.51). The result from 2 December 2014 shows that satellite-derived temperature estimate (1096 °C; occupying area of 3.05 m²) from a lava breakout has a close correspondence with a thermal camera measurement (1047 °C; occupying area of 4.52 m²). Effect of lava surface roughness was also taken into account by using the Hurst coefficient (H) to deriving the radiant flux and the crust thickness. Where the higher H (smoother surface) reflects thinner crust meanwhile, the lower H (rough surface) will reflect thicker crust. Crust thickness in the lava channel during 6 September 2014 (~3.4–7.7 m) is comparable with the lava height measurement in the field (~2.6–6.6 m). The study also shows that the total radiant flux peak is underestimated in comparison to other studies (Bonny et al., 2018; Wright et al., 2015), however, the trend is in good agreement with both field observation and other studies.

In the post-eruption scenario, an application of potential spectral unmixing methods on the lava flow field was presented. In total, fifteen spectral endmembers and their abundances were acquired. The first endmember was chosen as the brightest pixel, which represented saturated incandescent lava. These 15 endmembers were grouped into six groups (basalt, oxidized surface, sulfate mineral, hot material, water, and noise) based on the similarity shape of the endmembers since the amplitude varies due to illumination conditions, spectral variability, and topography. The endmembers represent pure surface materials in a hyperspectral image. A combination of SMACC and LSMA methods offers an optimum and a method for fast selection and discrimination of volcanic product. However, ground-truth spectra are recommended for further analysis. Synergistic use of airborne data from both FENIX (VIS-SWIR) and OWL (TIR) offers potential for lava surface discrimination in future, due to the complementary nature of the reflective (VIS-SWIR) and emissive (TIR) spectral regions. This might significantly improve our understanding of physical lava surface properties and emplacement stories of large lava fields.

For the lava flow roughness, we perform both the topographic position index (TPI) and One-dimensional Hurst Exponent to derived lava flow unit roughness on the 2014-2015 lava field at Holuhraun using both airborne LiDAR and photogrammetry topography datasets. The roughness assessment was acquired from four lava flow features: (1) spiny lava, (2) lava pond, (3) blocky surface, and (4) inflated channel. The TPI patterns on spiny lava and inflated channels show that the intermediate TPI values correspond to a small slope indicating a flat and smooth surface. Lava pond is characterized by low to high TPI

values and forms a wave-like pattern. Meanwhile, irregular transitions patterns from low to high TPI values indicate a rough surface that is found in blocky lava and flow margins. The surface roughness of these lava features falls within the H range of 0.30 ± 0.05 to 0.76 ± 0.04 . The roughest surface is the blocky, and inflated lava flows appear to be the smoothest surface among these four lava units. In general, the Hurst exponent values in the 2014-2015 lava flow field at Holuhraun has a strong tendency towards 0.5, which is in good agreement with earlier studies on geological surface roughness. These techniques could be used on any topographic surface, including terrestrial and planetary lava flow fields. The application of multi remote sensing techniques and datasets to derive physical properties of the 2014-2015 lava flow field at Holuhraun was successfully applied in this thesis.

6 Synthesis

The purpose of this chapter is to synthesize the key findings resulting from this study and to put them into a broader perspective. It is followed by putting the scientific work of this thesis in a broader context and closing with an outlook on future efforts on lava flow remote sensing.

To summarize, the author employed multimodal remote sensing techniques and datasets to develop three studies; (1) deriving thermal properties from satellite infrared remote sensing, (2) differentiating lava surface using airborne hyperspectral remote sensing, and (3) quantifying lava surface roughness from elevation model acquired by airborne LiDAR and photogrammetry. In the first study, we present a new approach based on infrared satellite images to derive thermal properties within the lava field during eruption and then compare the results with field measurement during the eruption. In the second study, we focus on retrieving the lava surface types contributing to the signal recorded by airborne hyperspectral at the very top surface of the lava flow-field. In the third study, we perform a roughness assessment on the part of the lava flow field using both airborne LiDAR and photogrammetry topography datasets. These studies demonstrate the potential multimodal remote sensing data sets and techniques can be used for estimating properties of lava flow fields. Overall, this study provides an important application of remote sensing methods in the monitoring of growing lava flow fields. The application of the techniques can be useful in case of future events and for lava flow hazard assessment, simulation, and mitigation.

However, physical modelling and assumption play a central role in extracting information with those techniques. Almost by definition, remotely sensed data must pass through the atmosphere on its path from the lava flow to the sensor, in this context also the part of atmospheric modelling needs to be considered. Different types of measurements are affected in different ways and by different components. Before accurate values of the required parameters can be obtained, these nuisance parameters must be accounted for using assumptions, external data, or more commonly modelled values (Davies et al., 2008; Harris, 2013a; Vaughan et al., 2003). Obtaining these parameters requires knowledge in the field and how to characterize parameters, what can we measure and what we need to assume. That means that more work integrating field knowledge with that of remote sensing will help us to better understand signals obtained during remote observations and thus enhancing our understanding of remote sensing.

6.1 Future for remote sensing for the volcano, artificial intelligence, and new sensor?

Retrieval of the physical properties of volcanic products has long been crucial for volcanologist since they play a pivotal role in eruption dynamics and could serve as parameters for future volcano hazard assessment. Once volcanic products, such as a lava flow, volcanic ash and gas are ejected, multimodal remote sensing plays an important role in terms of tracking their short-term impacts and assessing their long-term impacts. When

characterizing multimodal remote sensing attended for volcanology application, one must keep in mind that multimodal data differs according to sensors, resolutions, revisit cycle, spectrum, and mode of imaging. The increased use of multimodal remote sensing sensors, ranging from thermal, infrared, hyperspectral, multispectral, radar, LiDAR, optical video, etc., make it desirable to develop more methods for simultaneous use of multiple data sources to improve volcanic surveillance, mapping and physical information on products expelled in case of an eruption.

Such datasets are getting larger since sensors are getting more robust and complicated. In order to handle such datasets, machine learning is an effective empirical approach to analyzing data from complex nonlinear systems. Such systems can be massively multivariate, involving a few or literally thousands of variables. As a broad subfield of artificial intelligence (AI), machine learning (ML) is concerned with algorithms and techniques that allow computers to “learn” by example and interpret the results. This will also enable an analysis of large areas on Earth and other planetary bodies. The major focus of machine learning is to extract information from acquired data automatically by using computational and statistical methods that have been correlated with the actual observed phenomenon. Over the last decade, there has been considerable progress in developing machine learning methodology for a variety of phenomenon, volcanological being on of more promising and high importance due to the similarity between volcanoes and hazard they pose to its surroundings (Anantrasirichai et al., 2019).

In terms of volcanic products, machine learning has been applied to lava flow morphology, lava flow delineation, SO₂ height retrieval and volcanic ash classification (Hajian et al., 2019; Li et al., 2017; Maschmeyer et al., 2019; Waske et al., 2009). All these studies were focused on testing a single sensor (dataset), resulting in biased results. However, multimodal remote sensors might provide a solution to those biases. The integration of spectral information obtained by remote sensors with spatial, contextual, and structural information obtained by field measurement has demonstrated considerable improvements in achieving accurate interpretation and classification of observed phenomenon (Hajian et al., 2019). Future satellite missions and new sensors also will undoubtedly benefit us in term of dataset range and resolution. The invention of new and different sensors will provide new insight into the subject at study. Therefore, from the point of view of remote sensing future is bright, as is the future of knowledge on Earth natural processes and comparative studies. For the future of volcano remote sensing, volcanology, volcano hazard assessment and mitigation to the community, greater studies by remote sensors will surely be of benefit

References

- Abrams, M., Pieri, D., Realmuto, V., & Wright, R. (2013). Using EO-1 hyperion data as hypsIRI preparatory data sets for volcanology applied to Mt Etna, Italy. *IEEE Journal of Selected Topics in Applied Earth Observations and Remote Sensing*, 6(2), 375–385. <https://doi.org/10.1109/JSTARS.2012.2224095>
- Adams, J. B., Sabol, D. E., Kapos, V., Almeida Filho, R., Roberts, D. A., Smith, M. O., & Gillespie, A. R. (1995). Classification of multispectral images based on fractions of endmembers: Application to land-cover change in the Brazilian Amazon. *Remote Sensing of Environment*. [https://doi.org/10.1016/0034-4257\(94\)00098-8](https://doi.org/10.1016/0034-4257(94)00098-8)
- Adams, J. B., Smith, M. O., & Johnson, P. E. (1986). Spectral mixture modeling: A new analysis of rock and soil types at the Viking Lander 1 Site. *Journal of Geophysical Research*. <https://doi.org/10.1029/JB091iB08p08098>
- Alessio, E., Carbone, A., Castelli, G., & Frappietro, V. (2002). Second-order moving average and scaling of stochastic time series. *European Physical Journal B*. <https://doi.org/10.1140/epjb/e20020150>
- Alvarez-Ramirez, J., Echeverria, J. C., & Rodriguez, E. (2008). Performance of a high-dimensional R / S method for Hurst exponent estimation. *Physica A: Statistical Mechanics and Its Applications*, 387(26), 6452–6462. <https://doi.org/10.1016/j.physa.2008.08.014>
- Anantrasirichai, N., Biggs, J., Albino, F., & Bull, D. (2019). A deep learning approach to detecting volcano deformation from satellite imagery using synthetic datasets. *Remote Sensing of Environment*, 230. <https://doi.org/10.1016/j.rse.2019.04.032>
- Anderson, S. W., & Fink, J. H. (1990). The Development and Distribution of Surface Textures at the Mount St. Helens Dome. https://doi.org/10.1007/978-3-642-74379-5_2
- Anderson, Steven W., Stofan, E. R., Plaut, J. J., & Crown, D. A. (1998). Block size distributions on silicic lava flow surfaces: Implications for emplacement conditions. *Bulletin of the Geological Society of America*. [https://doi.org/10.1130/0016-7606\(1998\)110<1258:BSDOSL>2.3.CO;2](https://doi.org/10.1130/0016-7606(1998)110<1258:BSDOSL>2.3.CO;2)
- Arellano, S. R. (2013). Studies of volcanic plumes with spectroscopic remote sensing techniques --- DOAS and FTIR observations at Karymsky, Nyiragongo, Popocatepetl and Tungurahua, 93.
- Aufaristama, M., Höskuldsson, Á., Jónsdóttir, I., & Ólafsdóttir, R. (2016). Mapping and Assessing Surface Morphology of Holocene Lava Field in Krafla (NE Iceland) Using Hyperspectral Remote Sensing. *IOP Conference Series: Earth and Environmental Science*, 29, 1–6. <https://doi.org/10.1088/1755-1315/29/1/012002>

- Awange, J. L., & Kyalo Kiema, J. B. (2013). Fundamentals of remote sensing. In *Environmental Science and Engineering (Subseries: Environmental Science)*. https://doi.org/10.1007/978-3-642-34085-7_7
- Babič, M., Kokol, P., Guid, N., & Panjan, P. (2014). A new method for estimating the Hurst exponent H for 3D objects. *Materiali in Tehnologije*, 48(2), 203–208.
- Ball, M., Pinkerton, H., & Harris, A. J. L. (2008). Surface cooling, advection and the development of different surface textures on active lavas on Kilauea, Hawai'i. *Journal of Volcanology and Geothermal Research*, 173(1–2), 148–156. <https://doi.org/10.1016/j.jvolgeores.2008.01.004>
- Bernstein, L. S., Adler-Golden, S. M., Sundberg, R. L., Levine, R. Y., Perkins, T. C., Berk, A., ... Hoke, M. L. (2005). A new method for atmospheric correction and aerosol optical property retrieval for VIS-SWIR multi- and hyperspectral imaging sensors: QUAC (QUick Atmospheric Correction). In *International Geoscience and Remote Sensing Symposium (IGARSS)*. <https://doi.org/10.1109/IGARSS.2005.1526613>
- Bernstein, Lawrence S. (2012). Quick atmospheric correction code: algorithm description and recent upgrades. *Optical Engineering*, 51(11), 111719. <https://doi.org/10.1117/1.OE.51.11.111719>
- Blackett, M. (2014). Early analysis of landsat-8 thermal infrared sensor imagery of volcanic activity. *Remote Sensing*. <https://doi.org/10.3390/rs6032282>
- Blackett, M., & Matthew. (2017). An Overview of Infrared Remote Sensing of Volcanic Activity. *Journal of Imaging*, 3(2), 13. <https://doi.org/10.3390/jimaging3020013>
- Bonny, E., Thordarson, T., Wright, R., Höskuldsson, A., & Jónsdóttir, I. (2018). The Volume of Lava Erupted During the 2014 to 2015 Eruption at Holuhraun, Iceland: A Comparison Between Satellite- and Ground-Based Measurements. *Journal of Geophysical Research: Solid Earth*. <https://doi.org/10.1029/2017JB015008>
- Bretar, F., Arab-Sedze, M., Champion, J., Pierrot-Deseilligny, M., Heggy, E., & Jacquemoud, S. (2013). An advanced photogrammetric method to measure surface roughness: Application to volcanic terrains in the Piton de la Fournaise, Reunion Island. *Remote Sensing of Environment*. <https://doi.org/10.1016/j.rse.2013.03.026>
- Browning, J., & Gudmundsson, A. (2015). Surface displacements resulting from magma-chamber roof subsidence, with application to the 2014–2015 Bardarbunga-Holuhraun volcanotectonic episode in Iceland. *Journal of Volcanology and Geothermal Research*, 308, 82–98. <https://doi.org/10.1016/j.jvolgeores.2015.10.015>
- Byrnes, J. M., & Crown, D. A. (2002). Morphology, stratigraphy, and surface roughness properties of Venusian lava flow fields. *Journal of Geophysical Research E: Planets*, 107(10), 9–1. <https://doi.org/10.1029/2001je001828>
- Byrnes, J. M., Ramsey, M. S., & Crown, D. a. (2004). Surface unit characterization of the Mauna Ulu flow field, Kilauea Volcano, Hawai'i, using integrated field and remote sensing analyses. *Journal of Volcanology and Geothermal Research*, 135(1–2), 169–193. <https://doi.org/10.1016/j.jvolgeores.2003.12.016>

- Candela, T., Renard, F., Bouchon, M., Brouste, A., Marsan, D., Schmittbuhl, J., & Voisin, C. (2009). Characterization of fault roughness at various scales: Implications of three-dimensional high resolution topography measurements. *Pure and Applied Geophysics*, *166*(10–11), 1817–1851. <https://doi.org/10.1007/s00024-009-0521-2>
- Cashman, K. V., Thornber, C., & Kauahikaua, J. P. (1999). Cooling and crystallization of lava in open channels, and the transition of Pāhoehoe Lava to 'A'ā. *Bulletin of Volcanology*, *61*(5), 306–323. <https://doi.org/10.1007/s004450050299>
- Clark, R. N., & Roush, T. L. (1984). Reflectance spectroscopy: quantitative analysis techniques for remote sensing applications. *Journal of Geophysical Research*. <https://doi.org/10.1029/JB089iB07p06329>
- Coppola, D., Ripepe, M., Laiolo, M., & Cigolini, C. (2017). Modelling satellite-derived magma discharge to explain caldera collapse. *Geology*, *45*(6), 523–526. <https://doi.org/10.1130/G38866.1>
- Couillard, M., & Davison, M. (2005). A comment on measuring the Hurst exponent of financial time series. *Physica A: Statistical Mechanics and Its Applications*. <https://doi.org/10.1016/j.physa.2004.09.035>
- Daskalopoulou, V., Sykioti, O., & Karagiannopoulou, C. (2018). Application of Spectral Unmixing on Hyperspectral data of the Historic volcanic products of Mt . Etna (Italy). *Proceedings*, *2*(April), 1–8. <https://doi.org/10.3390/ecrs-2-05142>
- Daskalopoulou, V., Sykioti, O., Karagiannopoulou, C., Koutroumbas, K., & Rontogiannis, A. (2018). Application of Spectral Unmixing on Hyperspectral Data of the Historic Volcanic Products of Mt. Etna (Italy). *Proceedings* . <https://doi.org/10.3390/ecrs-2-05142>
- Davies, A. G., Calkins, J., Scharenbroich, L., Vaughan, R. G., Wright, R., Kyle, P., ... Tran, D. (2008). Multi-instrument remote and in situ observations of the Erebus Volcano (Antarctica) lava lake in 2005: A comparison with the Pele lava lake on the jovian moon Io. *Journal of Volcanology and Geothermal Research*, *177*(3), 705–724. <https://doi.org/10.1016/j.jvolgeores.2008.02.010>
- De Assis, T. A. (2015). The role of Hurst exponent on cold field electron emission from conducting materials: From electric field distribution to Fowler-Nordheim plots. *Scientific Reports*, *5*(January), 1–13. <https://doi.org/10.1038/srep10175>
- de Michele, M., Raucoules, D., & Arason, T. (2016). Volcanic Plume Elevation Model and its velocity derived from Landsat 8. *Remote Sensing of Environment*, *176*, 219–224. <https://doi.org/10.1016/j.rse.2016.01.024>
- Dozier, J. (1981). A method for satellite identification of surface temperature fields of subpixel resolution. *Remote Sensing of Environment*, *11*(C), 221–229. [https://doi.org/10.1016/0034-4257\(81\)90021-3](https://doi.org/10.1016/0034-4257(81)90021-3)
- Fargier, Y., Dore, L., & Ihamouten, A. (2018). Surface variations effect on electrical resistivity measurement: Aroughness based approach. *Journal of Applied Geophysics*, *159*, 341–349. <https://doi.org/10.1016/j.jappgeo.2018.08.016>

- Ferrucci, F., & Hirn, B. (2016). Automated monitoring of high-temperature volcanic features: from high-spatial to very-high-temporal resolution. *Geological Society, London, Special Publications*, 426(1), 159–179.
- Fink, J. H., & Fletcher, R. C. (1978). Ropy pahoehoe: Surface folding of a viscous fluid. *Journal of Volcanology and Geothermal Research*, 4(1–2), 151–170. [https://doi.org/10.1016/0377-0273\(78\)90034-3](https://doi.org/10.1016/0377-0273(78)90034-3)
- Flynn, L. P., Harris, A. J. L., & Wright, R. (2001). Improved identification of volcanic features using Landsat 7 ETM+. *Remote Sensing of Environment*, 78(1–2), 180–193. [https://doi.org/10.1016/S0034-4257\(01\)00258-9](https://doi.org/10.1016/S0034-4257(01)00258-9)
- Gaddis, L. R., Mougini-Mark, P. J., & Hayashi, J. N. (1990). Lava flow surface textures: SIR-B radar image texture, field observations, and terrain measurements. *Photogrammetric Engineering and Remote Sensing*, v. 56(2), 211–224.
- Ganci, G., James, M. R., Calvari, S., & Negro, C. Del. (2013). Separating the thermal fingerprints of lava flows and simultaneous lava fountaining using ground-based thermal camera and SEVIRI measurements. *Geophysical Research Letters*, 40(19), 5058–5063. <https://doi.org/10.1002/grl.50983>
- Geiger, H., Mattsson, T., Deegan, F. M., Troll, V. R., Burchardt, S., Gudmundsson, Ó., ... Harris, C. (2016). Magma plumbing for the 2014–2015 Holuhraun eruption, Iceland. *Geochemistry, Geophysics, Geosystems*, 17(8), 2953–2968. <https://doi.org/10.1002/2016GC006317>
- Gíslason, S. ., Stefánsdóttir, G., Pfeffer, M. a., Barsotti, S., Jóhannsson, T., Galeczka, I., ... Gudmundsson, M. T. (2015). Environmental pressure from the 2014–15 eruption of Bárðarbunga volcano, Iceland. *Geochemical Perspectives Letters*, 1, 84–93. <https://doi.org/10.7185/geochemlet.1509>
- Gong, Y., Misture, S. T., Gao, P., & Mellott, N. P. (2016). Surface roughness measurements using power spectrum density analysis with enhanced spatial correlation length. *Journal of Physical Chemistry C*. <https://doi.org/10.1021/acs.jpcc.6b06635>
- Graetinger, A. H., Ellis, M. K., Skilling, I. P., Reath, K., Ramsey, M. S., Lee, R. J., ... McGarvie, D. W. (2013). Remote sensing and geologic mapping of glaciovolcanic deposits in the region surrounding Askja (Dyngjufjöll) volcano, Iceland. *International Journal of Remote Sensing*, 34(20), 7178–7198. <https://doi.org/10.1080/01431161.2013.817716>
- Griffiths, R. W., & Fink, J. H. (1992). The morphology of lava flows in planetary environments: Predictions from analog experiments. *Journal of Geophysical Research*, 97(B13), 19739. <https://doi.org/10.1029/92JB01953>
- Gruninger, J. H., Ratkowski, A. J., & Hoke, M. L. (2004). The sequential maximum angle convex cone (SMACC) endmember model. In *Algorithms and Technologies for Multispectral, Hyperspectral, and Ultraspectral Imagery X*, (Vol. 5425, p. 1). Proc. SPIE. <https://doi.org/10.1117/12.543794>

- Gudmundsson, A., Lecoeur, N., Mohajeri, N., & Thordarson, T. (2014). Dike emplacement at Bardarbunga, Iceland, induces unusual stress changes, caldera deformation, and earthquakes. *Bulletin of Volcanology*, 76(10), 1–7. <https://doi.org/10.1007/s00445-014-0869-8>
- Gudmundsson, M. T., Jónsdóttir, K., Hooper, A., Holohan, E. P., Halldórsson, S. A., Ófeigsson, B. G., ... Aiuppa, A. (2016). Gradual caldera collapse at Bárðarbunga volcano, Iceland, regulated by lateral magma outflow. *Science*, 353(6296). <https://doi.org/10.1126/science.aaf8988>
- Guest, J. E., Duncan, A. M., Stofan, E. R., & Anderson, S. W. (2012). Effect of slope on development of pahoehoe flow fields: Evidence from Mount Etna. *Journal of Volcanology and Geothermal Research*. <https://doi.org/10.1016/j.jvolgeores.2012.01.006>
- Guisan, Antoine, Weiss, Stuart B., and Weiss, A. D. (1999). GLM versus CCA spatial modeling of plant species distribution. *Plant Ecology*, 143(1), 107–122. Retrieved from <https://link.springer.com/article/10.1023/a:1009841519580>
- Hajian, A., Cannavò, F., Greco, F., & Nunnari, G. (2019). “classification of mount etna (Italy) volcanic activity by machine learning approaches,,. *Annals of Geophysics*, 62(2 Special Issue), 1–11. <https://doi.org/10.4401/ag-8049>
- Halldórsson, S. A., Bali, E., Hartley, M. E., Neave, D. A., Peate, D. W., Guðfinnsson, G. H., ... Thordarson, T. (2018). Petrology and geochemistry of the 2014–2015 Holuhraun eruption, central Iceland: compositional and mineralogical characteristics, temporal variability and magma storage. *Contributions to Mineralogy and Petrology*, 173(8), 1–25. <https://doi.org/10.1007/s00410-018-1487-9>
- Hamed, K. H. (2007). Improved finite-sample Hurst exponent estimates using rescaled range analysis. *Water Resources Research*, 43(4), 1–9. <https://doi.org/10.1029/2006WR005111>
- Hamilton, C. W., Mougini-Mark, P. J., Sori, M. M., Scheidt, S. P., & Bramson, A. M. (2018). Episodes of Aqueous Flooding and Effusive Volcanism Associated With Hrad Vallis, Mars. *Journal of Geophysical Research: Planets*. <https://doi.org/10.1029/2018JE005543>
- Hargitai, H. (2015). Inflated Lava Flow. In H. Hargitai & Á. Kereszturi (Eds.), *Encyclopedia of Planetary Landforms* (pp. 1029–1034). New York, NY: Springer New York. https://doi.org/10.1007/978-1-4614-3134-3_195
- Harris, A. J. L., Flynn, L. P., Keszthelyi, L., Mougini-Mark, P. J., Rowland, S. K., & Resing, J. A. (1998). Calculation of lava effusion rates from Landstat TM data. *Bulletin of Volcanology*, 60(1), 52–71. <https://doi.org/10.1007/s004450050216>
- Harris, A, Blake, S., Rothery, D. A., & Stevens, N. F. (1997). A chronology of the 1991 to 1993 Mount Etna eruption using advanced very high resolution radiometer data: Implications for real-time thermal volcano monitoring. *Journal of Geophysical Research*, 102(B4), 19. <https://doi.org/10.1029/96JB03388>

- Harris, Andrew. (2013a). *Thermal Remote Sensing of Active Volcanoes: A User's Manual*. Cambridge: Cambridge University Press. <https://doi.org/10.1017/CBO9781139029346>
- Harris, Andrew. (2013b). *Thermal Remote Sensing of Active Volcanoes*. Cambridge: Cambridge University Press. <https://doi.org/10.1017/CBO9781139029346>
- Hartley, M. E., & Thordarson, T. (2013). The 1874-1876 volcano-tectonic episode at Askja, North Iceland: Lateral flow revisited. *Geochemistry, Geophysics, Geosystems*, *14*(7), 2286–2309. <https://doi.org/10.1002/ggge.20151>
- Head, E. M., Maclean, A. L., & Carn, S. A. (2013). Mapping lava flows from Nyamuragira volcano (1967-2011) with satellite data and automated classification methods. *Geomatics, Natural Hazards and Risk*, *4*(2), 119–144. <https://doi.org/10.1080/19475705.2012.680503>
- Hellman, M. J., & Ramsey, M. S. (2004). Analysis of hot springs and associated deposits in Yellowstone National Park using ASTER and AVIRIS remote sensing. *Journal of Volcanology and Geothermal Research*. <https://doi.org/10.1016/j.jvolgeores.2003.12.012>
- Hollingsworth, J., Leprince, S., Ayoub, F., & Avouac, J. P. (2012). Deformation during the 1975-1984 Krafla rifting crisis, NE Iceland, measured from historical optical imagery. *Journal of Geophysical Research: Solid Earth*, *117*(11), 1–24. <https://doi.org/10.1029/2012JB009140>
- Hurst, H. E. (1951). Long-term Storage Capacity of Reservoirs. *Transactions of the American Society of Civil Engineers*.
- James, D. H. (2019). *Comparing Terrestrial and Extraterrestrial Lava Surface Roughness Using Digital Elevation Models From High Resolution Topography and Structure From Motion*. University of Northern Colorado. Retrieved from <https://digscholarship.unco.edu/theses>
- Jennes, J. (2006). Topographic Position Index (tpi_jen.avx) extension for ArcView 3.x, v. 1.3a. *Jeness Enterprises*.
- Jordan, T. M., Cooper, M. A., Schroeder, D. M., Williams, C. N., Paden, J. D., Siegert, M. J., & Bamber, J. L. (2017). Self-affine subglacial roughness: Consequences for radar scattering and basal water discrimination in northern Greenland. *Cryosphere*, *11*(3), 1247–1264. <https://doi.org/10.5194/tc-11-1247-2017>
- Karpouzli, E., & Malthus, T. (2003). The empirical line method for the atmospheric correction of IKONOS imagery. *International Journal of Remote Sensing*. <https://doi.org/10.1080/0143116021000026779>
- Keszthelyi, L. (2002). Classification of mafic lava flows from ODP Leg 183. In *Proc. Ocean Drill, Program Sci. Results* (Vol. 183). Retrieved from http://www-odp.tamu.edu/publications/183_SR/012/012.htm

- Keszthelyi, L., Thordarson, T., McEwen, A., Haack, H., Guilbaud, M. N., Self, S., & Rossi, M. J. (2004). Icelandic analogs to Martian flood lavas. *Geochemistry, Geophysics, Geosystems*, 5(11). <https://doi.org/10.1029/2004GC000758>
- Kilburn, C.R.J. (2000). Lava Flows And Flow Fields. In *Encyclopedia of Volcanoes* (pp. 291–306). Academic Press. <https://doi.org/10.1029/00EO00168>
- Kilburn, Christopher R J. (2000). Lava flows and flow fields. In H. Sigurdsson (Ed.), *Encyclopedia of Volcanoes* (pp. 291–305). San Diego: Academic Press.
- Kizel, F., Benediktsson, J. A., Bruzzone, L., Pedersen, G. B. M., Vilmundardottir, O. K., & Falco, N. (2018). Simultaneous and constrained calibration of multiple hyperspectral images through a new generalized empirical line model. *IEEE Journal of Selected Topics in Applied Earth Observations and Remote Sensing*. <https://doi.org/10.1109/JSTARS.2018.2804666>
- Kolzenburg, S., Jaenicke, J., Münzer, U., & Dingwell, D. B. (2018). The effect of inflation on the morphology-derived rheological parameters of lava flows and its implications for interpreting remote sensing data - A case study on the 2014/2015 eruption at Holuhraun, Iceland. *Journal of Volcanology and Geothermal Research*, 357, 200–212. <https://doi.org/10.1016/j.jvolgeores.2018.04.024>
- Kolzenburg, Stephan, Giordano, D., Thordarson, T., Höskuldsson, A., & Dingwell, D. B. (2017). The rheological evolution of the 2014/2015 eruption at Holuhraun, central Iceland. *Bulletin of Volcanology*, 79(6), 45. <https://doi.org/10.1007/s00445-017-1128-6>
- Kuang, J. H., & Chien, H. L. (2011). The effect of film thickness on mechanical properties of TiN thin films. *Advanced Science Letters*, 4(11–12), 3570–3575. <https://doi.org/10.1166/asl.2011.1856>
- Li, L., Canters, F., Solana, C., Ma, W., Chen, L., & Kervyn, M. (2015). Discriminating lava flows of different age within Nyamuragira's volcanic field using spectral mixture analysis. *International Journal of Applied Earth Observation and Geoinformation*, 40, 1–10. <https://doi.org/10.1016/j.jag.2015.03.015>
- Li, L., Solana, C., Canters, F., Chan, J., & Kervyn, M. (2015). Impact of environmental factors on the spectral characteristics of lava surfaces: field spectrometry of basaltic lava flows on Tenerife, Canary Islands, Spain. *Remote Sensing*, 7(12), 16986–17012. <https://doi.org/10.3390/rs71215864>
- Li, L., Solana, C., Canters, F., & Kervyn, M. (2017). Testing random forest classification for identifying lava flows and mapping age groups on a single Landsat 8 image. *Journal of Volcanology and Geothermal Research*, 345, 109–124. <https://doi.org/10.1016/j.jvolgeores.2017.07.014>
- Lillesand, T. ., & Kiefer, R. . (1987). *Remote Sensing and Image Interpretation* (2nd ed.). Toronto: John Wiley and Sons, Inc. Retrieved from <http://nature.berkeley.edu/~penggong/textbook/reference.htm>

- Lombardo, V., & Buongiorno, M. F. (2006). Lava flow thermal analysis using three infrared bands of remote-sensing imagery: A study case from Mount Etna 2001 eruption. *Remote Sensing of Environment*, 101(2), 141–149. <https://doi.org/10.1016/j.rse.2005.12.008>
- Lombardo, V., Buongiorno, M. F., Pieri, D., & Merucci, L. (2004). Differences in Landsat TM derived lava flow thermal structures during summit and flank eruption at Mount Etna. *Journal of Volcanology and Geothermal Research*, 134(1–2), 15–34. <https://doi.org/10.1016/j.jvolgeores.2003.12.006>
- Lombardo, V., Musacchio, M., & Buongiorno, M. F. (2012). Error analysis of subpixel lava temperature measurements using infrared remotely sensed data. *Geophysical Journal International*, 191(1), 112–125. <https://doi.org/10.1111/j.1365-246X.2012.05632.x>
- Lombardo, Valerio, Merucci, L., & Buongiorno, M. F. (2006). Wavelength influence in sub-pixel temperature retrieval using the dual-band technique. *Annals of Geophysics*, 49(1), 227–234. <https://doi.org/10.4401/ag-3173>
- Lombardo, Valerio, Silvestri, M., & Spinetti, C. (2011). Near real-time routine for volcano monitoring using infrared satellite data. *Annals of Geophysics*, 54(5), 522–534. <https://doi.org/10.4401/ag-5336>
- Lopes, R. M. C., & Kilburn, C. R. J. (1990). Emplacement of lava flow fields: application of terrestrial studies to Alba Patera, Mars. *Journal of Geophysical Research*. <https://doi.org/10.1029/jb095ib09p14383>
- MacKay, M. E., Rowland, S. K., Mouginis-Mark, P. J., & Garbeil, H. (1998). Thick lava flows of Karisimbi Volcano, Rwanda: Insights from SIR-C interferometric topography. *Bulletin of Volcanology*, 60(4), 239–251. <https://doi.org/10.1007/s004450050230>
- Malinverno, A. (1990). A simple method to estimate the fractal dimension of a self-affine series. *Geophysical Research Letters*. <https://doi.org/10.1029/GL017i011p01953>
- Mallonee, H. C., Kobs Nawotniak, S. E., McGregor, M., Hughes, S. S., Neish, C. D., Downs, M., ... Team, F. (2017). Lava flow morphology classification based on measures of roughness. In *48th Lunar and Planetary Science Conference* (p. Abstract 2992).
- Martinez, O. S., Cruz, D. M., Chavarin, J. U., & Bustos, E. S. (2014). Rough Surfaces Profiles and Speckle Patterns Analysis by Hurst Exponent Method, 3(12), 759–766.
- Martino, G. Di, Iodice, A., Riccio, D., & Ruello, G. (2008). Volcano monitoring via fractal modeling of lava flows. *Proceedings of the 2008 2nd Workshop on USE of Remote Sensing Techniques for Monitoring Volcanoes and Seismogenic Areas, USEReST 2008*, 1–5. <https://doi.org/10.1109/USEREST.2008.4740342>

- Maschmeyer, C. H., White, S. M., Dreyer, B. M., & Clague, D. A. (2019). High-silica lava morphology at ocean spreading ridges: Machine-learning seafloor classification at alarcon rise. *Geosciences* (Switzerland), 9(6). <https://doi.org/10.3390/geosciences9060245>
- Mokarram, M., Roshan, G., & Negahban, S. (2015). Landform classification using topography position index (case study: salt dome of Korsia-Darab plain, Iran). *Modeling Earth Systems and Environment*, 1(4), 1–7. <https://doi.org/10.1007/s40808-015-0055-9>
- Moore, R. B., Clague, D. A., Rubin, M., & Bohrsen, W. A. (1987). Volcanism in Hawaii. In *U.S. Geological Survey Professional Paper 1350* (p. 557). [https://doi.org/10.1016/0003-6870\(73\)90259-7](https://doi.org/10.1016/0003-6870(73)90259-7)
- Morgan, H. A. (2012). *Lava Discharge Rate Estimates From Thermal Infrared Satellite Data At Pacaya Volcano, Guatemala*. Michigan Technological University.
- Morris, A. R., Anderson, F. S., Mougini-Mark, P. J., Haldemann, A. F. C., Brooks, B. A., & Foster, J. (2008). Roughness of Hawaiian volcanic terrains. *Journal of Geophysical Research E: Planets*. <https://doi.org/10.1029/2008JE003079>
- Murphy, S. W., Filho, C. R. de S., & Oppenheimer, C. (2011). Monitoring volcanic thermal anomalies from space: Size matters. *Journal of Volcanology and Geothermal Research*, 203(1–2), 48–61. <https://doi.org/10.1016/j.jvolgeores.2011.04.008>
- Murphy, S. W., Oppenheimer, C., Roberto, C., & Filho, D. S. (2003). Calculating radiant flux from thermally heterogeneous targets.
- Neish, C. D., Hamilton, C. W., Hughes, S. S., Nawotniak, S. K., Garry, W. B., Skok, J. R., ... Heldmann, J. L. (2017). Terrestrial analogues for lunar impact melt flows. *Icarus*, 281, 73–89. <https://doi.org/10.1016/j.icarus.2016.08.008>
- Óladóttir, B. A., Larsen, G., & Sigmarsson, O. (2011). Holocene volcanic activity at Grímsvötn, Bárðarbunga and Kverkfjöll subglacial centres beneath Vatnajökull, Iceland. *Bulletin of Volcanology*. <https://doi.org/10.1007/s00445-011-0461-4>
- Oppenheimer, C., Rothery, D. A., Pieri, D. C., Abrams, M. J., & Carere, V. (1993). Analysis of Airborne Visible/Infrared Imaging Spectrometer (AVTRIS) data of volcanic hot spots. *International Journal of Remote Sensing*, 14(16), 2919–2934. <https://doi.org/10.1080/01431169308904411>
- Oppenheimer, Clive. (1991). Lava flow cooling estimated from Landsat Thematic Mapper infrared data: The Lonquimay Eruption (Chile, 1989). *Journal of Geophysical Research: Solid Earth*, 96(B13), 21865–21878. <https://doi.org/10.1029/91JB01902>
- Pedersen, G. B. M., Belart, J. M. C., Magnússon, E., Vilmundardóttir, O. K., Kizel, F., Sigurmundsson, F. S., ... Benediktsson, J. A. (2018). Hekla Volcano, Iceland, in the 20th Century: Lava Volumes, Production Rates, and Effusion Rates. *Geophysical Research Letters*, 45(4), 1805–1813. <https://doi.org/10.1002/2017GL076887>

- Pedersen, G. B. M., Hoskuldsson, A., Durig, T., Thordarson, T., Jónsdóttir, I., & Riishuus, M. . (2016). Lava field evolution and emplacement dynamics of the Holuhraun 2014-2015 eruption, Iceland.
- Pedersen, G. B. M., Höskuldsson, A., Dürig, T., Thordarson, T., Jónsdóttir, I., Riishuus, M. S., ... Schmith, J. (2017). Lava field evolution and emplacement dynamics of the 2014–2015 basaltic fissure eruption at Holuhraun, Iceland. *Journal of Volcanology and Geothermal Research*. <https://doi.org/10.1016/j.jvolgeores.2017.02.027>
- Pieri, D. C., Glaze, L. S., & Abrams, M. J. (1990). Thermal radiance observations of an active lava flow during the June 1984 eruption of Mount Etna. *Geology*, *18*(10), 1018–1022.
- Piscini, a., & Lombardo, V. (2014). Volcanic hot spot detection from optical multispectral remote sensing data using artificial neural networks. *Geophysical Journal International*, *196*(3), 1525–1535. <https://doi.org/10.1093/gji/ggt506>
- Pyle, D. M., Mather, T. A., & Biggs, J. (2013). Remote sensing of volcanoes and volcanic processes: Integrating observation and modelling-introduction. *Geological Society Special Publication*, *380*(1), 1–13. <https://doi.org/10.1144/SP380.14>
- Ramsey, F. S., & Fink, J. . (1999). Estimating silicic lava vesicularity with thermal remote sensing : a new technique for volcanic mapping and monitoring. *Bull Volcanol*, *61*, 32–39.
- Ramsey, M. S., & Harris, A. J. L. (2013). Volcanology 2020: How will thermal remote sensing of volcanic surface activity evolve over the next decade? *Journal of Volcanology and Geothermal Research*, *249*, 217–233. <https://doi.org/10.1016/j.jvolgeores.2012.05.011>
- Ramsey, M. S., Harris, A. J. L., & Crown, D. A. (2016). What can thermal infrared remote sensing of terrestrial volcanoes tell us about processes past and present on Mars? *Journal of Volcanology and Geothermal Research*, *311*, 198–216. <https://doi.org/10.1016/j.jvolgeores.2016.01.012>
- Raoufi, D., & Hosseinpanahi, F. (2012). Surface Morphology Dynamics in ITO Thin Films. *Journal of Modern Physics*, *03*(08), 645–651. <https://doi.org/10.4236/jmp.2012.38088>
- Read, J. ., & Torrado, M. (2009). *International encyclopedia of human geography*. (R. Kitchin & N. Thrift, Eds.), *International Encyclopedia of Human Geography*. Elsevier Science. <https://doi.org/10.5860/choice.48-0052>
- Reynolds, H. I., Gudmundsson, M. T., Högnadóttir, T., Magnússon, E., & Pálsson, F. (2017). Subglacial volcanic activity above a lateral dyke path during the 2014–2015 Bárðarbunga-Holuhraun rifting episode, Iceland. *Bulletin of Volcanology*, *79*(6), 38. <https://doi.org/10.1007/s00445-017-1122-z>

- Riley, D., & Hecker, C. (2013). Mineral Mapping with Airborne Hyperspectral Thermal Infrared Remote Sensing at Cuprite, Nevada, USA. In C. Kuenzer & S. Dech (Eds.), *Thermal Infrared Remote Sensing: Sensors, Methods, Applications* (Vol. 17, pp. 495–514). Springer Netherlands. https://doi.org/10.1007/978-94-007-6639-6_24
- Rothery, D. A., Francis, P. W., & Wood, C. A. (1988). Volcano monitoring using short wavelength infrared data from satellites. *Journal of Geophysical Research*, 93(B7), 7993. <https://doi.org/10.1029/JB093iB07p07993>
- Rowan, L. C., Mars, J. C., & Simpson, C. J. (2005). Lithologic mapping of the Mordor, NT, Australia ultramafic complex by using the Advanced Spaceborne Thermal Emission and Reflection Radiometer (ASTER). *Remote Sensing of Environment*. <https://doi.org/10.1016/j.rse.2004.11.021>
- Rowland, S. K., & Walker, G. P. (1990). Pahoehoe and aa in Hawaii: volumetric flow rate controls the lava structure. *Bulletin of Volcanology*. <https://doi.org/10.1007/BF00301212>
- Sanchez-Ortiz, W., Andrade-Gómez, C., Hernandez-Martinez, E., & Puebla, H. (2015). Multifractal hurst analysis for identification of corrosion type in AISI 304 stainless steel. *International Journal of Electrochemical Science*, 10(2), 1054–1064.
- Schlerf, M., Rock, G., Lagueux, P., Ronellenfitsch, F., Gerhards, M., Hoffmann, L., & Udelhoven, T. (2012). A hyperspectral thermal infrared imaging instrument for natural resources applications. *Remote Sensing*, 4(12), 3995–4009. <https://doi.org/10.3390/rs4123995>
- Schmidt, A., Leadbetter, S., Theys, N., Carboni, E., Witham, C. S., Stevenson, J. A., ... Shepherd, J. (2015). Satellite detection, long-range transport, and air quality impacts of volcanic sulfur dioxide from the 2014–2015 flood lava eruption at Bárðarbunga (Iceland). *Journal of Geophysical Research*, 120(18), 9739–9756. <https://doi.org/10.1002/2015JD023638>
- Shepard, M. K., Campbell, B. A., Bulmer, M. H., Farr, T. G., Gaddis, L. R., & Plaut, J. J. (2001). The roughness of natural terrain: A planetary and remote sensing perspective. *Journal of Geophysical Research: Planets*, 106(E12), 32777–32795. <https://doi.org/10.1029/2000JE001429>
- Smets, B., Wauthier, C., & d'Oreye, N. (2010). A new map of the lava flow field of Nyamulagira (D.R. Congo) from satellite imagery. *Journal of African Earth Sciences*, 58(5), 778–786. <https://doi.org/10.1016/j.jafrearsci.2010.07.005>
- Spinetti, C., Mazzarini, F., Casacchia, R., Colini, L., Neri, M., Behncke, B., ... Pareschi, M. T. (2009). Spectral properties of volcanic materials from hyperspectral field and satellite data compared with LiDAR data at Mt. Etna. *International Journal of Applied Earth Observation and Geoinformation*, 11(2), 142–155. <https://doi.org/10.1016/j.jag.2009.01.001>
- Swanson, D. A. (1973). Pahoehoe flows from the 1969–1971 mauna ulu eruption, kilauea volcano, Hawaii. *Bulletin of the Geological Society of America*. [https://doi.org/10.1130/0016-7606\(1973\)84<615:PFFTMU>2.0.CO;2](https://doi.org/10.1130/0016-7606(1973)84<615:PFFTMU>2.0.CO;2)

- Tayebi, M. H., Tangestani, M. H., Vincent, R. K., & Neal, D. (2014). Spectral properties and ASTER-based alteration mapping of Masahim volcano facies, SE Iran. *Journal of Volcanology and Geothermal Research*, 287, 40–50. <https://doi.org/10.1016/j.jvolgeores.2014.09.013>
- Thordarson, T., & Larsen, G. (2007). Volcanism in Iceland in historical time: Volcano types, eruption styles and eruptive history. *Journal of Geodynamics*, 43(1), 118–152. <https://doi.org/10.1016/j.jog.2006.09.005>
- Thordarson, Thorvaldur, & Höskuldsson, Á. (2008). Postglacial volcanism in Iceland. *JÖKULL*, (58), 197–228.
- Torres-Argüelles, V., Oleschko, K., Tarquis, A. M., Korvin, G., Gaona, C., Parrot, J. F., & Ventura-Ramos, E. (2010). Fractal Metrology for biogeosystems analysis. *Biogeosciences*, 7(11), 3799–3815. <https://doi.org/10.5194/bg-7-3799-2010>
- Tubman, K. M., & Crane, S. D. (1995). Vertical versus Horizontal Well Log Variability and Application to Fractal Reservoir Modeling. *Fractals in Petroleum Geology and Earth Processes*, 279–293. https://doi.org/10.1007/978-1-4615-1815-0_13
- Vaughan, R. G., Calvin, W. M., & Taranik, J. V. (2003). SEBASS hyperspectral thermal infrared data: Surface emissivity measurement and mineral mapping. *Remote Sensing of Environment*, 85(1), 48–63. [https://doi.org/10.1016/S0034-4257\(02\)00186-4](https://doi.org/10.1016/S0034-4257(02)00186-4)
- Warren, M. A., Taylor, B. H., Grant, M. G., & Shutler, J. D. (2014). Data processing of remotely sensed airborne hyperspectral data using the Airborne Processing Library (APL): Geocorrection algorithm descriptions and spatial accuracy assessment. *Computers and Geosciences*, 64, 24–34. <https://doi.org/10.1016/j.cageo.2013.11.006>
- Waske, B., Benediktsson, J. A., Árnason, K., & Sveinsson, J. R. (2009). Mapping of hyperspectral AVIRIS data using machine-learning algorithms. *Canadian Journal of Remote Sensing*, 35(SUPPL. 1). <https://doi.org/10.5589/m09-018>
- Wawszczak, J. (2005). Methods for estimating the Hurst exponent. The analysis of its value for fracture surface research. *Materials Science- Poland*, 23(2), 585–591.
- Whelley, P. L., Glaze, L. S., Calder, E. S., & Harding, D. J. (2014). LiDAR-derived surface roughness texture mapping: Application to mount St. Helens pumice plain deposit analysis. *IEEE Transactions on Geoscience and Remote Sensing*, 52(1), 426–438. <https://doi.org/10.1109/TGRS.2013.2241443>
- Wright, R., Blackett, M., & Hill-Butler, C. (2015). Some observations regarding the thermal flux from Earth's erupting volcanoes for the period of 2000 to 2014. *Geophysical Research Letters*, 42(2), 282–289. <https://doi.org/10.1002/2014GL061997>
- Wright, R., Flynn, L., Garbeil, H., Harris, A., & Pilger, E. (2002). Automated volcanic eruption detection using MODIS. *Remote Sensing of Environment*, 82, 135–155. [https://doi.org/10.1016/S0034-4257\(02\)00030-5](https://doi.org/10.1016/S0034-4257(02)00030-5)

- Wright, R., & Flynn, L. P. (2003). On the retrieval of lava-flow surface temperatures from infrared satellite data. *Geology*, *31*(10), 893–896. <https://doi.org/10.1130/G19645.1>
- Wright, R., Garbeil, H., & Davies, A. G. (2010). Cooling rate of some active lavas determined using an orbital imaging spectrometer. *Journal of Geophysical Research: Solid Earth*, *115*(6), 1–14. <https://doi.org/10.1029/2009JB006536>
- Zakšek, K., Hort, M., & Lorenz, E. (2015). Satellite and ground based thermal observation of the 2014 effusive eruption at Stromboli Volcano. *Remote Sensing*, *7*(12), 17190–17211. <https://doi.org/10.3390/rs71215876>
- Zhang, J., Rivard, B., & Sanchez-Azofeifa, A. (2004). Derivative spectral unmixing of hyperspectral data applied to mixtures of lichen and rock. *IEEE Transactions on Geoscience and Remote Sensing*. <https://doi.org/10.1109/TGRS.2004.832239>
- Zhang, J., Rivard, B., & Sánchez-Azofeifa, A. (2005). Spectral unmixing of normalized reflectance data for the deconvolution of lichen and rock mixtures. *Remote Sensing of Environment*. <https://doi.org/10.1016/j.rse.2004.11.019>
- Zhang, X., Shang, K., Cen, Y., Shuai, T., & Sun, Y. (2014). Estimating ecological indicators of karst rocky desertification by linear spectral unmixing method. *International Journal of Applied Earth Observation and Geoinformation*, *31*(1), 86–94. <https://doi.org/10.1016/j.jag.2014.03.009>
- Zimbelman, J. R., Garry, W. B., Johnston, A. K., & Williams, S. H. (2008). Emplacement of the 1907 Mauna Loa basalt flow as derived from precision topography and satellite imaging. *Journal of Volcanology and Geothermal Research*, *177*(4), 837–847. <https://doi.org/10.1016/j.jvolgeores.2008.01.042>

**Paper I: New Insights for Detecting
and Deriving Thermal Properties of
Lava Flow Using Infrared Satellite
during 2014–2015 Effusive Eruption at
Holuhraun, Iceland**

Article

New Insights for Detecting and Deriving Thermal Properties of Lava Flow Using Infrared Satellite during 2014–2015 Effusive Eruption at Holuhraun, Iceland

Muhammad Afaristama ^{1,*} , Armann Hoskuldsson ¹, Ingibjorg Jonsdottir ¹, Magnus Orn Ulfarsson ²  and Thorvaldur Thordarson ^{1,3}

¹ Institute of Earth Sciences, University of Iceland, Sturlugata 7, 101 Reykjavík, Iceland; armh@hi.is (A.H.); ij@hi.is (I.J.); torvth@hi.is (T.T.)

² Faculty of Electrical and Computer Engineering, University of Iceland, Hjardarhagi 2-7, 107 Reykjavík, Iceland; mou@hi.is

³ Faculty of Earth Sciences, University of Iceland, Sturlugata 7, 101 Reykjavík, Iceland

* Correspondence: mua2@hi.is; Tel.: +354-855-1242

Received: 14 November 2017; Accepted: 17 January 2018; Published: 20 January 2018

Abstract: A new lava field was formed at Holuhraun in the Icelandic Highlands, north of Vatnajökull glacier, in 2014–2015. It was the largest effusive eruption in Iceland for 230 years, with an estimated lava bulk volume of $\sim 1.44 \text{ km}^3$ covering an area of $\sim 84 \text{ km}^2$. Satellite-based remote sensing is commonly used as preliminary assessment of large scale eruptions since it is relatively efficient for collecting and processing the data. Landsat-8 infrared datasets were used in this study, and we used dual-band technique to determine the subpixel temperature (T_h) of the lava. We developed a new spectral index called the thermal eruption index (TEI) based on the shortwave infrared (SWIR) and thermal infrared (TIR) bands allowing us to differentiate thermal domain within the lava flow field. Lava surface roughness effects are accounted by using the Hurst coefficient (H) for deriving the radiant flux (Φ_{rad}) and the crust thickness (Δh). Here, we compare the results derived from satellite images with field measurements. The result from 2 December 2014 shows that a temperature estimate ($1096 \text{ }^\circ\text{C}$; occupying area of 3.05 m^2) from a lava breakout has a close correspondence with a thermal camera measurement ($1047 \text{ }^\circ\text{C}$; occupying area of 4.52 m^2). We also found that the crust thickness estimate in the lava channel during 6 September 2014 ($\sim 3.4\text{--}7.7 \text{ m}$) compares closely with the lava height measurement from the field ($\sim 2.6\text{--}6.6 \text{ m}$); meanwhile, the total radiant flux peak is underestimated ($\sim 8 \text{ GW}$) compared to other studies ($\sim 25 \text{ GW}$), although the trend shows good agreement with both field observation and other studies. This study provides new insights for monitoring future effusive eruption using infrared satellite images.

Keywords: effusive eruption; Landsat-8; TEI; SWIR; TIR; Hurst coefficient; dual-band; radiant flux; crust thickness

1. Introduction

Holuhraun is a lava field in the Icelandic Highlands, north of Vatnajökull (Figure 1). The 2014–2015 Holuhraun lava field was created by basaltic fissure eruptions [1,2]. The eruptions lasted from 31 August 2014 to 27 February 2015 and formed a lava flow field covering 84 km^2 , with a bulk volume of 1.44 km^3 [1,2]. This eruption is the largest effusive eruption observed in the last 230 years in Iceland. Field observation during the 2014–2015 eruption has been documented in detail, i.e., Pedersen et al. [1] compiled a detailed evolution of the lava field and created a corresponding database containing information of the lava flows. Most of these field observations are related to the modes of lava

transport and emplacement and thermal camera measurement, along with the mapping of the flow field growth and evolution [1,3]. This eruption offers an opportunity to improve our understanding of large effusive eruptions using satellite-based remote sensing. Here we present a new approach based on infrared satellite images to derive thermal properties within the lava field during eruption and then compare the results with field measurement.

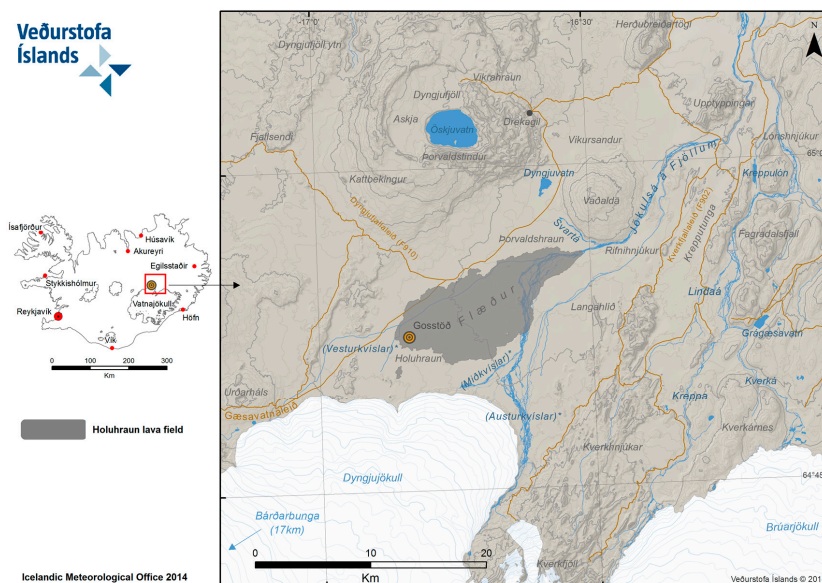


Figure 1. The new Holuhraun lava field map by Icelandic Meteorological Office (after modification) [4]. The Holuhraun lava field is situated on the flood plain, which is situated south of Askja volcano and north of Dyngjajökull, which is an outlet glacier from the Vatnajökull ice cap [1].

Study Area

Iceland is one of the most active volcanic regions on Earth; volcanic eruptions occur, on average, every four to five years, and produce more than 5 km³ magma per century [5]. The 6-month long eruption at Holuhraun 2014–2015 was the largest effusive eruption in Iceland in 230 years, with an estimated bulk lava volume of about 1.44 km³. The 2014–2015 Holuhraun lava flows are emplaced on the floodplain 0–6 km from the Dyngjajökull glacier (Figure 1) occupying a relatively flat area. The eruption had an average discharge of about 77 m³/s, making it the longest effusive eruption observed in modern times with such a flux [1,6]. According to the study of Pedersen et al. [1], the eruption was divided into three phases based on the lava field evolution, as follows:

Phase 1: Open channel lava pathways: 31 August to mid-October (Figure 2a);

Phase 2: Lava pond formation: Mid-October to end-November (Figure 2b);

Phase 3: Tube-fed lava pathways: early December to 27 February (Figure 2c).

The first phase of the 2014–2015 Holuhraun eruption was dominated by open lava channels. This phase had a discharge ~350–100 m³/s. The eruption began on a 1.8 km long fissure feeding up to 500 m wide, incandescent sheets of slabby pahoehoe [1,2]. Apart from fire fountaining in the first few weeks, in 15 days, the volcanic activity had formed an open channels lava flow that advanced 17–18 km towards NNE and subsequently the lava morphology changed to rubbly and aa types [1,7]. The second phase had a discharge ranging from 50 to 100 m³/s [1,6]. During this time, a lava pond <1 km² was formed at a distance of 0.8 km east of the vents [1]. This pond became the main point of

lava distribution, controlling the emplacement of the lava flows [1,2]. Towards the end of this phase, the open channel in the first phase was inflated due to new lava injections into the previously active lava channel lifting the channel [1]. The final (third) phase from December to the end of February had a mean discharge $<50 \text{ m}^3/\text{s}$. In this phase, the lava transport was confined to closed lava pathways within flows. Over 19 km^2 of the flow field was resurfaced via surface breakouts from the closed pathways [1].

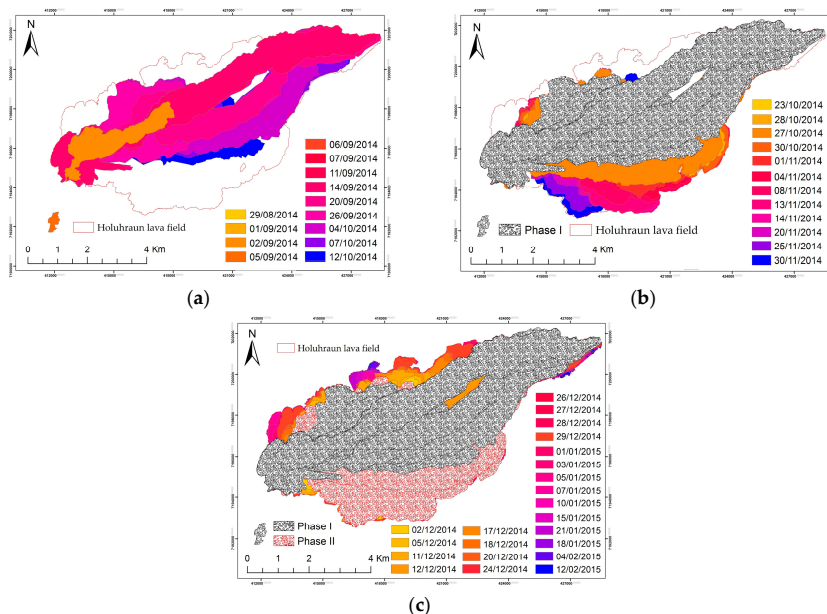


Figure 2. 2014–2015 Holuhraun eruption evolution: (a) First phase (b) second phase; (c) final (third) phase of eruption.

2. Infrared Remote Sensing in Volcanoes

Satellite-based infrared remote sensing data are increasingly being used to monitor active volcanoes around the world [8–10]. Monitoring volcanoes by infrared remote sensing is essential to improve understanding of active volcanoes. For example, thermal monitoring of volcanoes is necessary in order to understand the volcanic eruption processes. Effusive eruption activity can change rapidly over time as new lava flow form and develop. In many cases, thermal observations of active eruptions from both ground and aircraft are risky and difficult, especially when the lava covers a large area. Satellite-based remote sensing provides high temporal resolution infrared data that are suitable for monitoring long effusive eruption such as in the new lava field at Holuhraun, Iceland. Such a tool provides data in which effusive events are detectable and changes in the eruption style and evolution of activity can be identified regardless of the coarse spatial resolution of the data [11]. Satellite-based remote sensing can be used to monitor thermal activity within lava fields [9]. In the last 25 years, there have been several methods that have been used for deriving eruption activity information from infrared remotely-sensed data to estimate the thermal structures of hot volcanic features such as active lava flows [12–16], heat flux [11,17,18], effusive rate [10,11,17,18] and crust thickness [10,11]. In 1981, Dozier [19] developed a method involving a solution of simultaneous equations that allows the calculation of the ‘sub-pixel’ coverage and temperature of cool and hot components. This method is called the dual-band method, and involves two distinct infrared bands to formulate a system of two equations from the simultaneous solution of the Planck equation in each band as shown below:

$$R_x = pR(\lambda_x, T_h) + (1 - p)R(\lambda_x, T_c) \quad (1)$$

$$R_y = pR(\lambda_y, T_h) + (1 - p)R(\lambda_y, T_c) \quad (2)$$

where R_x and R_y are the radiances in bands x and y , respectively, ($\text{Wm}^{-2} \text{sr}^{-1} \text{m}^{-1}$) after adjusting for atmospheric effects and surface emissivity; p is the pixel portion occupied by the hot component; $R(\lambda_x, T_h)$ and $R(\lambda_y, T_c)$ are the radiances ($\text{Wm}^{-2} \text{sr}^{-1} \text{m}^{-1}$) emitted for wavelengths λ_x and λ_y , at surface temperatures T_h (hot component) and T_c (cool component), respectively. The dual-band method can be applied if the two bands of the short-wave infrared (SWIR) and the thermal infrared (TIR) data are available [20], whereby any two of the unknowns, T_c , T_h and p , can be estimated if the third is assumed. This method has been successfully applied by several researchers [5–10,13,14]. Harris et al. and Lombardo et al. [11,16] used dual band method to retrieve the crust and the hot cracks temperature for active lava flows in Mt. Etna. They used band 5 (1.55–1.75 μm) and 7 (2.08–2.35 μm) from Landsat Thematic Mapper (TM) and assumed T_h to estimate T_c and p . In this study, we develop a new spectral index for Landsat 8, named the thermal eruption index (TEI), based on the SWIR and TIR bands (bands 6 and 10). The purpose of the TEI consists mainly of two parts: (1) as a threshold for differentiating between different thermal domains; and (2) applying a dual-band method to estimate subpixel temperature within thermal domains and differentiating between the types of lava surface. The active lava surface has thermal domain complexity and could contain more than one thermal component [13,21]; here we use two thermal component scenarios, with T_h as temperature of lava surface and T_c as temperature surrounding the lava for different thermal domains. The remainder of this manuscript is organized as follows. Section 3 describes the datasets and the preprocessing. The proposed methodology for TEI, the dual-band method, the estimation of radiant flux (Φ_{rad}), and the crust thickness model of lava flow (Δh) is explained in Section 4. We also discuss the effect of lava surface roughness using Hurst coefficient (H) on Φ_{rad} and Δh . Further results are arranged in Section 5, and in Section 6 we give a brief discussion. In Section 7, we give a summary of our work.

3. Datasets and Preprocessing

3.1. Datasets

Remote sensing observations were made using Landsat 8 Level 1 product band 6 (1.56–1.66 μm) and band 10 (10.60–11.19 μm). The eruption was well monitored from Landsat 8, and although Landsat 8 only has a temporal resolution of once every 16 days (making it of limited value for making time series studies of the eruption), the spatial resolution makes it a good tool to derive thermal properties within the lava flow. Landsat 8 has different spatial resolution for band 6 and band 10: band 6 has 30 m spatial resolution and band 10 has 100 m spatial resolution (resampled to 30 m). The selection of band 6 and 10 are considered to minimize oversaturation effects over active lava flows. According to Blackett [22], Landsat 8 has an enhanced dynamic range compared to Landsat ETM+: this means that temperatures of up to 747.9 K can be detected without saturation in band 6 as compared with those for the corresponding ETM+ band 724.5 K. Acquisition dates are selected according to the availability and quality of data covering the eruption (Table 1), we only took the data where cloud coverage is minimal. The data can be downloaded from the U.S Geological Survey (USGS) website (<https://earthexplorer.usgs.gov>). In our work, we subset Landsat 8 images into 562 by 333 and then converted the satellite-recorded digital numbers (DN) to sensor radiance for both SWIR and TIR bands. In this study, we use radar Sentinel 1A data from 18 October 2014 to derive Hurst coefficient from the lava. This data represents roughness of the lava and can be downloaded from the website (<https://scihub.copernicus.eu/dhus/#/home>). We also use thermal camera (FLIR) measurement during 2 December 2014 that overlaps with the satellite data and theodolite lava height measurement in the field for result comparison.

Table 1. Product ID and the dates of the Landsat 8 datasets that were used in this study.

Product ID	Date
LC82170152014249LGN00	6 September 2014
LC82180142014272LGN00	29 September 2014
LC82180142014288LGN00	15 October 2014
LC80642292014297LGN00	24 October 2014
LC80642302014329LGN00	25 November 2014
LC80652292014336LGN00	2 December 2014
LC80652292014352LGN00	18 December 2014
LC80652292015003LGN00	3 January 2015
LC82180142015035LGN00	4 February 2015

3.2. Atmospheric and Emissivity Correction

The MODTRAN model atmosphere is used for atmospheric correction in this study [13,23]. Since emissivity and atmospheric effects will vary by wavelength [20], corrections are needed for both SWIR and TIR as follows:

$$R_{\text{SWIR}} = [L(\lambda_{\text{SWIR}}) - L_{\text{R}}(\lambda_{\text{SWIR}})] / \tau \varepsilon \quad (3)$$

$$R_{\text{TIR}} = [L(\lambda_{\text{TIR}}) - L_{\text{U}}(\lambda_{\text{TIR}})] / \tau \varepsilon \quad (4)$$

where R_{SWIR} and R_{TIR} are the corrected spectral radiances at wavelength λ_{SWIR} and λ_{TIR} , respectively, $L(\lambda_{\text{SWIR}})$ and $L(\lambda_{\text{TIR}})$ are the spectral radiances at the sensor, $L_{\text{U}}(\lambda_{\text{TIR}})$ is the atmospheric upwelling radiance, $L_{\text{R}}(\lambda_{\text{SWIR}})$ is the atmospheric reflected radiance, τ is atmospheric transmissivity, and ε is the surface emissivity. In this case, we set the emissivity at 0.97 for the Holuhraun basaltic lava. R_{SWIR} and R_{TIR} will be used in Sections 4.1 and 4.2 both as an input for the calculation of TEI and for the dual-band method.

4. Method

4.1. Thermal Eruption Index (TEI)

In this study, TEI is developed by using the SWIR and the TIR bands from the medium spatial resolution satellite Landsat 8. The method uses the sensitivity difference between SWIR (band 6) and TIR (band 10) to detect pixel hot spots instead of using mid-infrared (MIR) as in NTI (Normalized Thermal Index) [22,24]. The objective of TEI is to provide a new variant for a hotspot thermal index derived by using data from the medium spatial resolution satellite Landsat 8. We derive TEI based on image observation and define the empirical formula for this observation. TEI is based on the principle that the SWIR spectral radiance (R_{SWIR}) on the crust will be less than in the TIR spectral radiance (R_{TIR}) and vice versa on the active lava ($R_{\text{SWIR}} > R_{\text{TIR}}$) as shown in Figure 3a. Figure 3b shows band 6 and band 10 of Landsat 8 from the 6 September 2014 Holuhraun eruption, the active lava pixels are emitting more spectral radiance in both band 6 and band 10; meanwhile the crust pixels are emitting more spectral radiance only in TIR. Therefore TEI has higher values in the active lava than in crust. This index uses the square of the TIR spectral radiance and the maximum of the SWIR spectral radiance to differentiate between the thermal domains. TEI is expressed as

$$\text{TEI} = \frac{R_{\text{SWIR}} - \frac{(R_{\text{TIR}})^2}{10 R_{\text{SWIR MAX}}}}{R_{\text{SWIR}} + \frac{(R_{\text{TIR}})^2}{10 R_{\text{SWIR MAX}}} \left(\frac{R_{\text{SWIR MAX}}}{3} \right)^2} \quad (5)$$

where R_{SWIR} and R_{TIR} are the pixel corrected spectral radiances detected in the band 6 and band 10, respectively and $R_{\text{SWIR MAX}}$ are the maximum spectral radiances detected in band 6 for each scene. In this study, we applied the dual band method to automatically calculate the hot component temperature

within the region defined by the hotspot threshold ($TEI > 0.10$). This selected value is explained in more detail in Sections 5.1 and 5.3.

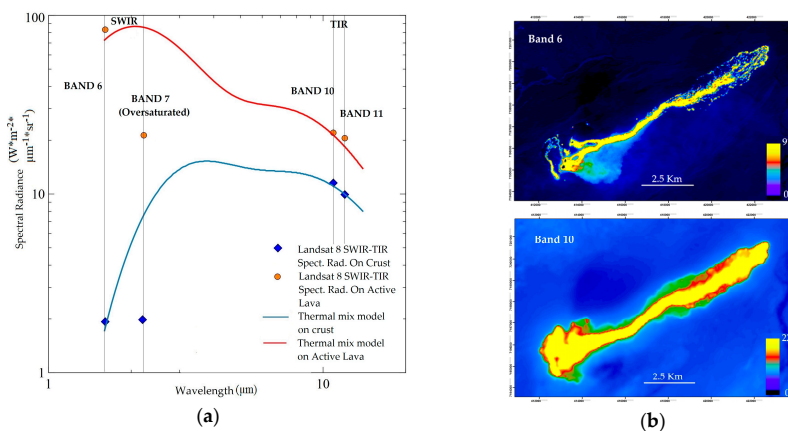


Figure 3. R_{SWIR} and R_{TIR} from Landsat 8 of the lava flow at Holuhraun, Iceland, on 6 September 2014. (a) Spectral radiances plot of SWIR (Band 6 and 7)–TIR (Band 10 and 11) and thermal mix model (hybrid Planck curve for the mixed pixel) (b) the band 6 detects the emissions from active lava (yellow-orange color); band 10 detects the emissions both from active lava and crust (red-green color).

4.2. Dual-Band Method

The dual-band method relies on a system of two equations (Equations (1) and (2)) and requires the assumption of one of three unknowns, T_h , T_c and p . In term of this study, we consider that T_h relates to the temperature of recently active lava and recently crusted lava, while T_c relates to the surrounding temperature that is influenced by the eruption processes (Figure 4). both of these can be assumed; meanwhile, p is typically difficult to assume accurately and therefore has to be derived [22].



Figure 4. The pixel mixture of the cool and the hot components. The region defined by the hot component temperature (T_h) has pixel portion (p) and the region defined by the cool component temperature (T_c) has pixel portion ($1-p$): (a) A picture taken by Armann Hoskuldsson in Holuhraun, in 13 September 2014 showing the hot and the cool components; (b) The model of Landsat 8 mixed thermal pixel with 30 m pixel resolution.

In this study, we set T_c equal to the lowest brightness temperature detected in TIR for each thermal domain considered, with $T_c = 25$ °C in the surrounding warm crust, $T_c = 50$ °C in the surrounding hot crust, and $T_c = 85$ °C in the active lava. These assumptions will be suitable in situations where

different thermal domains (active lava and crust) within the lava flow are clearly separable. We solve p by iterating on T_h , until $p(R_{SWIR}) = p(R_{TIR})$ then we can rearrange Equations (1) and (2) into

$$p(R_{SWIR}) = \frac{R_{SWIR} - R(\lambda_{SWIR}, T_c)}{R(\lambda_{SWIR}, T_h) - R(\lambda_{SWIR}, T_c)} \quad (6)$$

$$p(R_{TIR}) = \frac{R_{TIR} - R(\lambda_{TIR}, T_c)}{R(\lambda_{TIR}, T_h) - R(\lambda_{TIR}, T_c)} \quad (7)$$

4.3. Radiant Flux Estimation

Radiation is the most direct heat flux to estimate. For rough lava surface (aa and brecciated surface), not all the radiation can escape from the lava surface because of surface scattering. Therefore, in this paper, we propose to use the Hurst coefficient (H) [25,26] to describe the surface roughness of lava, so that the actual radiation emitted is reduced due to the fractal model. Following this model, the radiant flux (Φ_{rad}) for each pixel that contains lava can be estimated as

$$\Phi_{rad} = \varepsilon \sigma H A T_e^4 \quad (8)$$

where Φ_{rad} is the radiant flux (W), σ is the Stefan–Boltzmann constant ($5.67 \times 10^{-8} \text{ W m}^{-2} \text{ K}^{-4}$), and A is the Landsat 8 pixel area, which is 900 m^2 . In this approach, we use the effective temperature model (T_e), expressed as

$$T_e = \left(p T_h^4 + (1 - p) T_c^4 \right)^{1/4} \quad (9)$$

which is the average surface temperature of lava for the two thermal components present on the lava flow surface [27,28]. H is the Hurst coefficient ($0 < H < 1$), where a higher H means a smoother surface. We set H for each thermal domain within lava field as shown in Table 2, these values were derived from radar image speckle pattern transect (H') [29] and we normalized with 0.5 according to the study by Shepard et al. [30]. Further details about the derivation of H from radar image are explained in Appendix A.

Table 2. The values of the Hurst coefficient for different thermal domains.

H'	H (after Normalized)	Description	Thermal Domain
0.43	0.21	Very rough surface (Aa flow, large, tilted, spinny pates [30]).	Warm crust
0.70	0.35	Rough surface (Aa flow, small spinny plates [30]).	Hot crust
0.89	0.44	Smooth surface (Sheet pahoehoe flow, channel, roppy structure [30]).	Active lava

4.4. Convective Flux Estimation

Convective flux (Φ_{conv}) is estimated for the entire lava-flow field with a similar approach as above for Φ_{rad} , i.e., given surface temperature T_e and surfaces roughness H , Φ_{conv} is calculated using the free convection formula given by [11,14] which is given by

$$\Phi_{conv} = A h_c H (T_e - T_a) \quad (10)$$

where the unit of Φ_{conv} is W, $h_c = 5 \text{ W m}^{-2} \text{ K}^{-1}$ is the heat transfer coefficient for free convection [11], and T_a is the ambient air temperature that is unaffected by eruption processes. In this work we use $T_a = 25 \text{ }^\circ\text{C}$.

4.5. Crust Thickness Model

The crust thickness Δh is calculated by assuming that the conductive flux density across the surface crust is equal to the total of the radiative and convective flux densities leaving the same surface of lava [20,23], so that

$$M_{\text{rad}} + M_{\text{conv}} = -k \frac{T_i - T_e}{\Delta h} \quad (11)$$

Then, re-arranged for Δh :

$$\Delta h = -k \frac{\Delta T}{M_{\text{rad}} + M_{\text{conv}}} \quad (12)$$

where Δh is the crust thickness (m), M_{rad} and M_{conv} are radiative and convective flux densities (W m^{-2}), respectively, k is the thermal conductivity, where we use $2.5 \text{ W m}^{-1} \text{ K}^{-1}$ [14,31], and T_i is the temperature of the lava flow interior. In this study, we use an interior temperature of $1128 \text{ }^\circ\text{C}$ (for lava outside vent) and $1200 \text{ }^\circ\text{C}$ (for lava surrounding vent); these values were selected according to thermocouple measurements for freshly exposed patches of lava in Holuhraun on the 19 and 20 November 2014 [3]. M_{rad} and M_{conv} are obtained by dividing Φ_{rad} and Φ_{conv} by the pixel area A . Figure 5 depicts the physical meaning of Δh [10,20]. On rough surface (aa and brecciated surface) Δh is the thickness of the thermal boundary beneath a thermally mixed surface rubble [10,20]. Meanwhile, since there is no surface rubble in smooth surface (brittle layer and thin), we can assume that Δh is the complete thickness of the thermal boundary of the lava surface [10,20].

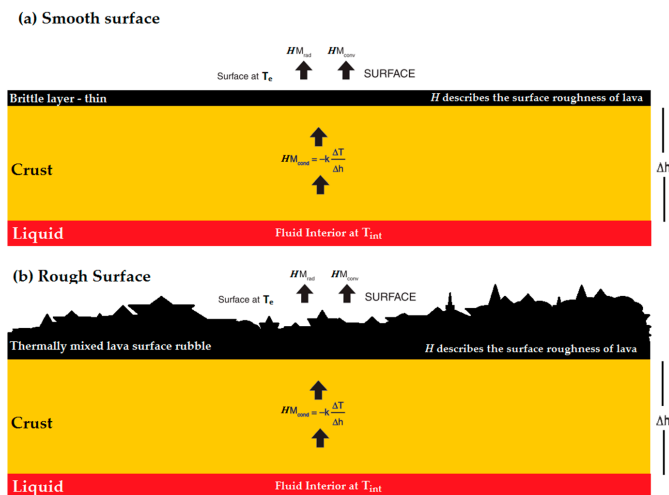


Figure 5. Conductive model of the surface of lava and the basal thermal boundary layers for (a) an active smooth surface lava flow and (b) a crusted rough surface lava flow. (Adapted and modified from Harris [20] p. 222).

5. Results

5.1. TEI Hotspots Anomaly

We detected different types of hotspots associated with the 2014–2015 Holuhraun eruption by using TEI. In this section, we review some of these results to illustrate the utility of the TEI for differentiating thermal anomalies within the lava field. As noted in Section 4.1, TEI detects hotspots with $\text{TEI} > 0.10$, but it does not discriminate between the different types of the hotspot domains that occurs in the lava field. As a result, the interpretation can be difficult, as the active lava, hot crust and warm crust could be mistaken for eruptive activity. Therefore, accurate lava evolution where the

hotspots occur becomes critical for determining the domain of TEI anomaly. Thus, we selected the image from 6 September 2014 to assess the TEI value, since the image has a clear difference between active lava and recently emplaced crust. Figure 6a shows the spatial distribution of TEI on 6 September 2014. In general, TEI values detect hotspots in the range from 0.10 to 0.53. We distinguish the two main thermal domains within the lava flow field. The first is the active lava domain, which is characterized by high TEI. The second is the crust domain surrounding active lava, characterized by TEI below active lava domain but exceeding the hotspot threshold (>0.10). Figure 6b shows that the active lava domains have TEI value of >0.51 : this value is related to high emitted radiance in SWIR and TIR, whilst crust domains have value ranging from 0.10 to 0.51. The crust zone itself is divided into two sub-domains: (1) hot crust domain, having values ranging from 0.21 to 0.51; (2) warm crust domain, having values ranging from 0.10 to 0.21. This also can be seen during 29 September and 24 October (See Appendix B). Clearly, TEI allows better discrimination within the lava flow; active lava, crust and non-volcanic hotspot, offering the possibility that different mode of lava flows can be automatically discriminated based of TEI threshold as will be discussed in Section 5.3.

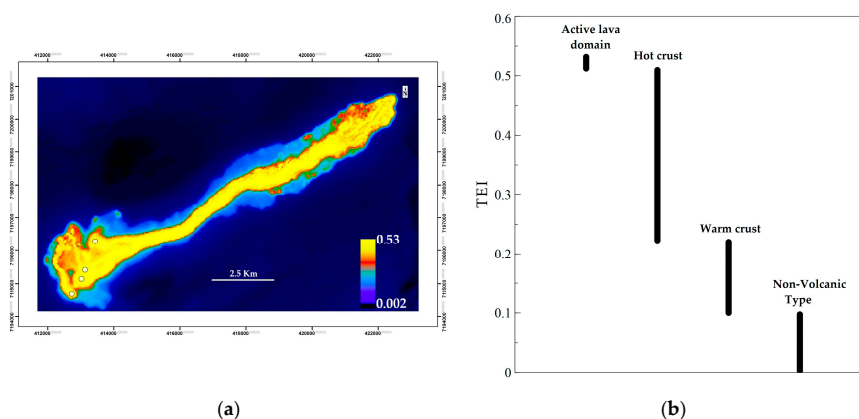


Figure 6. (a) Spatial distribution of thermal eruption index (TEI) during the 6 September 2014 eruption: the four white dots show the location of the vents during the first phase of eruption [1]; (b) TEI differentiates four different thermal domains within the Holuhraun lava flow on 6 September 2014. TEI allows the active lava domain to be distinguished from crust domain and the non-volcanic hotspot domain.

5.2. Spatial Distribution of T_h and p

Table 3 shows the hot component temperature (T_h) and the pixel portion of the hot component (p) computed by using the TEI based dual band-method for nine Landsat 8 time series during the eruption. Our solutions of T_h ranges between 344 °C and 1208 °C, and p ranges between 0.10 and 13% with an average of 769 °C and 1.5%, respectively. Figure 7 shows the spatial distribution map of T_h , and p obtained from the Landsat 8 time series. The highest T_h and lowest p mostly relate to active lava locations such as channels, lava ponds and breakouts. Meanwhile, the lowest T_h and highest p corresponds to crust zone in the edge of active lava and flow fronts that indicates lava cooling and formed thick crust, as lava cools the crust component increases and progressively thickens from the vent towards the distal end. Such results are broadly consistent with observed emplacement processes of aa flows on the 6 September 2014. The result points out that lowest p (0.10–0.17%) of a pixel, equivalent to 0.90–1.53 m², can be occupied by small freshly exposed lava patches or breakouts; this will be discussed further in Section 6.

Table 3. Maximum, minimum and mean T_h , p , and TEI values derived from the Landsat 8 time series.

Date	T_h min (°C)	T_h max (°C)	T_h average (°C)	p Min	p Max	P Average	TEI Min	TEI Max
6 September 2014	346	1185	685	0.14%	13%	2.2%	0.102	0.53
29 September 2014	442	1199	885	0.10%	6%	1%	0.100	0.53
15 October 2014	526	1195	816	0.11%	5%	1.2%	0.101	0.53
24 October 2014	347	1195	705	0.13%	13%	2%	0.100	0.53
25 November 2014	392	1201	901	0.11%	7%	0.08%	0.102	0.53
2 December 2014	368	1208	770	0.10%	10%	1.4%	0.101	0.53
18 December 2014	358	1191	677	0.17%	10%	2.1%	0.100	0.53
3 January 2015	344	1176	689	0.15%	13%	2%	0.102	0.53
4 February 2015	487	1154	790	0.12%	4%	1%	0.101	0.53

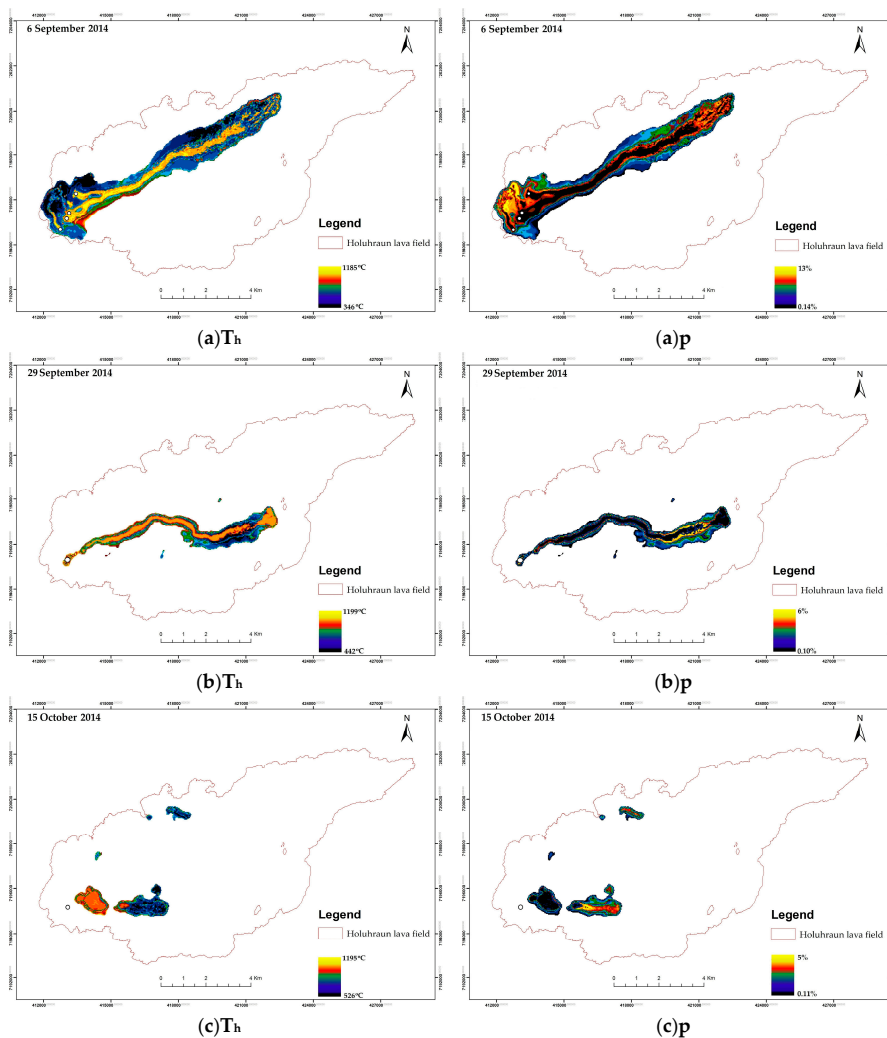


Figure 7. Cont.

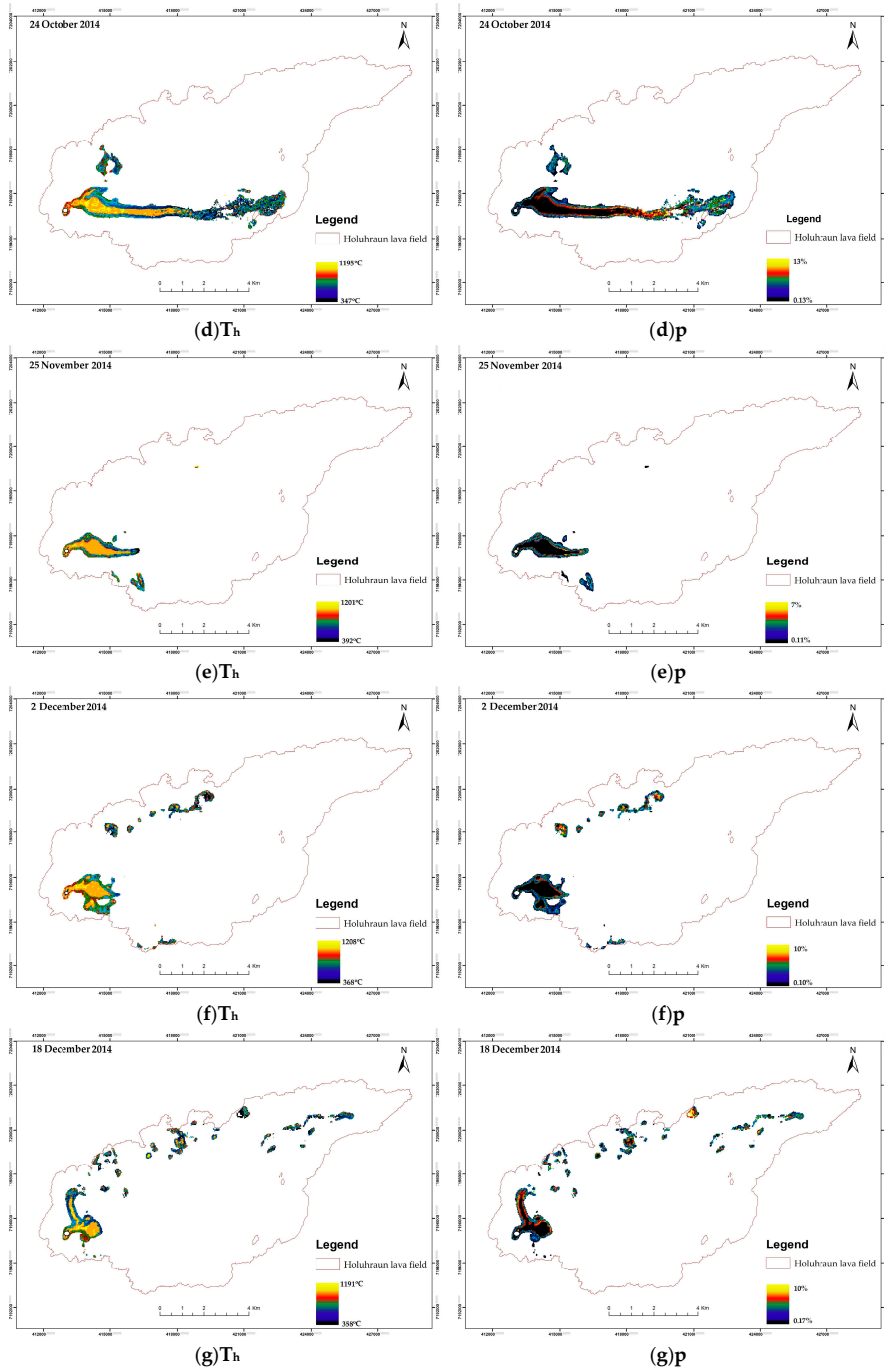


Figure 7. Cont.

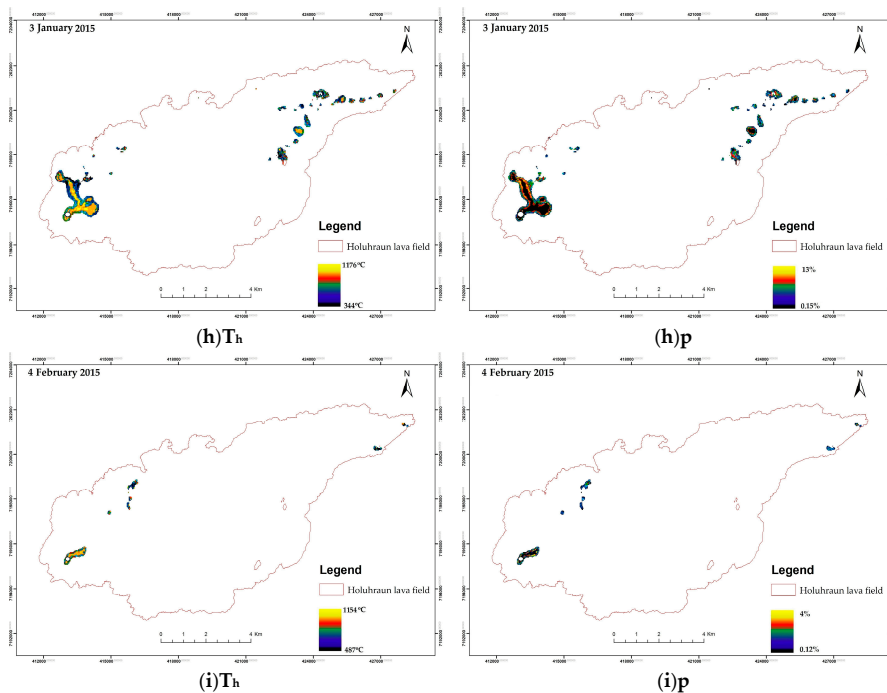


Figure 7. Spatial distribution map of T_h and p during 2014–2015 Holuhraun eruption: (a) 6 September 2014; (b) 29 September 2014; (c) 15 October 2014; (d) 24 October 2014; (e) 25 November 2014; (f) 2 December 2014; (g) 18 December 2014; (h) 3 January 2015; and (i) 4 February 2015. White dot show vent locations.

5.3. Trend T_h vs. p and TEI

We plotted T_h as a function of p and TEI, respectively for 6 September 2014, as shown in Figure 8a,b, respectively. The scatter plot of T_h vs. p shows a logarithmic decrease in T_h as p increases: this means that the higher the temperature, the smaller the pixel portion. This general trend is in good agreement with theoretical models [13,14,16,21]. There are three sub-trends (x , y and z) identified on the scatter plots (Figure 8a,b), and these sub trends allow for classification of lava thermal domain as shown in Figure 8c. The same trends are observed on open channel flow during 29 September and 24 October (See Appendix C). This classification shows that the active lava domain is associated with T_h in the range 901–1208 °C and p in the range 0.1–0.13% with TEI > 0.51, while the hot crust domain is in the range of 400–900 °C and p in the range of 0.20–7.5% with TEI 0.21–0.51 and warm crust domain is in the range of 346–750 °C and p is in the range of 0.30–13% with TEI 0.10–0.22. This classification result has good agreement with lava flow field observations. In Figure 8a, we observe a nearly linear decrease for sub-trend x ; on the other hand, the scatter plot associated with sub-trend y and z show logarithmic decrease as in the general trend. The scatter distribution for sub-trend x has its support in region enclosed by T_h between 901 and 1185 °C and p between 0.10% and 1.30%. For sub-trend y , T_h ranges between 400 and 900 °C while p in the range 0.10–7.5% and for sub-trend z , T_h ranges between 346 and 750 °C while p remains in the range 0.10–13%. These trends are also apparent in scatter plots of T_h versus TEI. The trends show large variation in T_h within the sub-trends. Examination of the scatter distribution for sub-trend y exhibits wide range of T_h (346–1150 °C) being associated with a range 0.10–0.21 of TEI. For sub-trend z , T_h ranges between 400 and 1160 °C while TEI is in the range 0.21–0.51. Meanwhile for sub-trend x , T_h ranges between 901 and 1185 °C while exhibiting narrow

range of TEI between 0.51 and 0.53. One can note from these results that maximum T_h could occur in $TEI < 0.51$. This can happen for several reasons: (a) The effect of plumes from the eruption that mix within the lava pixels. This means that, due to the sensibility of band 6 [32], the plume was detected as high radiance in band 6. This makes $TEI > 0.1$ (hotspot threshold) and the dual-band produces very high temperatures, while $TEI < 0.51$: (b) A different spatial resolution between band 6 (30 m) and band 10 (100 m) causes lower TEI value due to the small fragments of high emission lava in band 6 that is not detected in band 10.

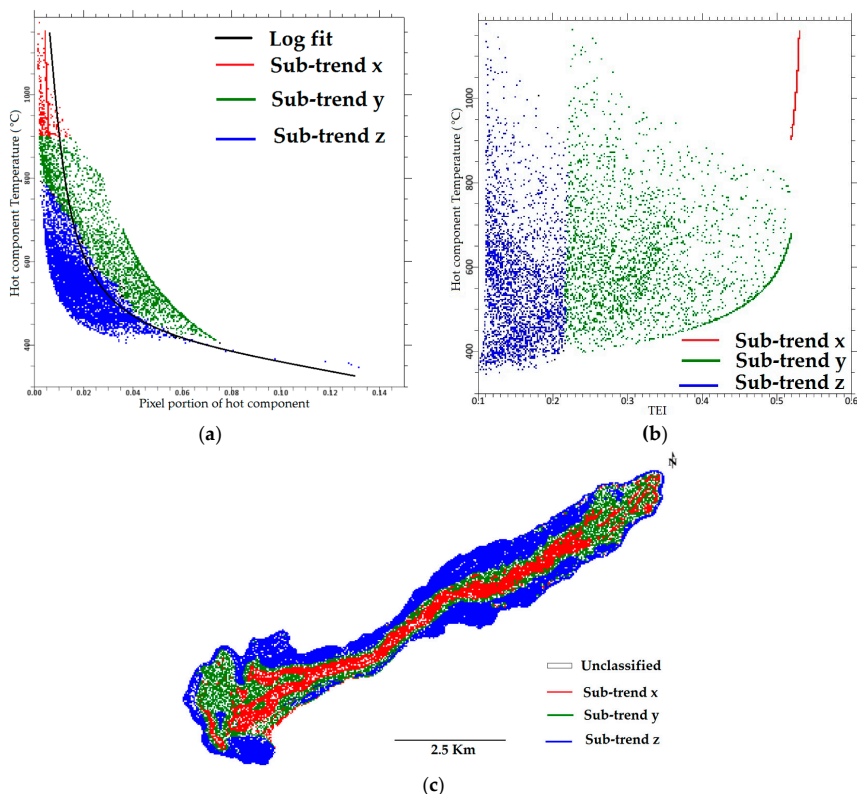


Figure 8. (a) Scatter plot of T_h vs. p ; (b) Scatter plot of T_h vs. TEI; (c) classification of lava thermal domain on 6 September 2014.

5.4. Radiant Flux Time Series during 2014–2015 Holuhraun Eruption

Figure 9 depicts the temporal evolution of the radiant flux (total energy radiated) for nine observations of the 2014–2015 Holuhraun effusive eruptions. As mentioned in Section 3.1, Landsat 8 has limited value for making time series studies of the eruption, since the temporal resolution is low and there are quite a lot of flux gaps. However, the trend shows good agreement with results from MODIS done by Wright et al. [33] during the first 101 days of eruption, although our total radiant flux peak is underestimated compared to Wright et al. [33] since we consider the effect of the Hurst coefficient (H) parameter that affects the total flux value (discussed in Section 6). The maximum peak detected is on day 7 of the eruption (6 September 2014), with a total flux of 7.8 GW, and then it continues to decline until it reaches a low level of 1.6 GW on day 46 before it rises again to a new peak of 3.2 GW on day 55. It then decreases to a new low on day 87 with 1.3 GW and then it increases to a new peak on day 110 with 1.6 GW. Then, it continues to decrease until day 158 with 0.2 GW, indicating

that the eruption has almost stopped. This total flux peak trend is also in good agreement with field observations [1,2]: the first phase of eruption is related to the evolution of the vent system from a fissure with discrete vents distributed along the length of the fissure (day 7) decreasing in number with time to eruption from a single source vent (day 30) and formed a lava pond in the second phase (day 46) (Figure 7a–c). Then, on day 55, the pond becomes the main lava distributor and the pond size continues to decrease [1,2] until the final phase of eruption starts on day 110 (Figure 7d–f). In the final phase of eruption, during days 110, 126 and 158, the flow field was mostly formed via surface breakouts [1,2] until the eruption stopped (Figure 7g–i).

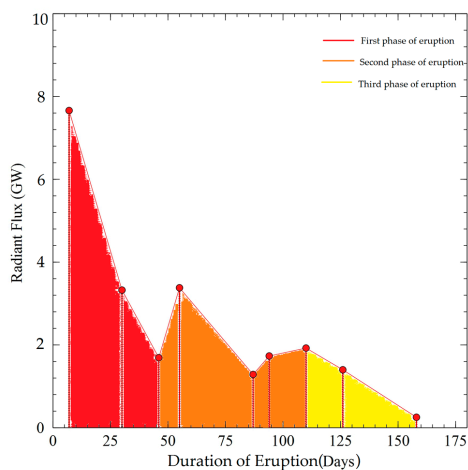


Figure 9. Time series of the total radiant flux estimated from Landsat 8 for the 2014–2015 Holuhraun eruption.

5.5. Crust Thickness Model of Lava Flow

Figure 10a shows the crust thickness estimate of lava flow for 6 September 2014. The thickness estimates range from 2 to 15 m. The thickest crust is located along the edge of lava flow and in lava flow front. Meanwhile the thinnest part is mostly located in the active lava flow (lava channel and breakouts). This result also has a good agreement with Rossi et al. [34] that shows using TanDEM-X data, that the thickness in the lava field ranges between 0 and 15 m during 9 September 2014 with the thicker part along the edge and the thinner parts in the middle of the channel. For comparison, 15 points of lava height measurement were done using Theodolite during 3 to 4 September 2014 (location measurement points are in Appendix D). Figure 10b shows the comparison between thickness measurement from the field and the satellite derived estimate. We found that the ground-based thickness measurement are closer to the satellite derived estimates in the middle of lava channel. Meanwhile, along the edge of lava flow, the satellite derived thickness estimates are thicker than the ground-based measurements. Presumably, this is because the lava in the edge cools down and fully develops into crust on satellite, since there are temporal gaps between the field observations and the satellite derived estimates. On the other hand, the lava in the middle of the channel is still active and has not completely cooled, and this leads to small thickness difference between the field measurement and the satellite derived estimates. We also note that we only derive the crust thickness and not complete thickness of the lava, since there are still have fluid interior layer beneath the crust, especially for active lava flow, as seen in Figure 5.

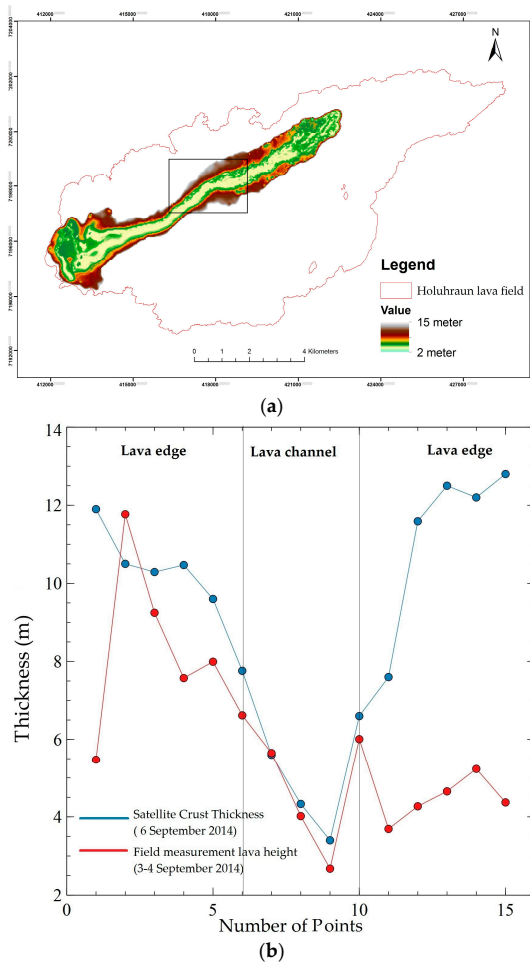


Figure 10. (a) Crust thickness estimate derived from Landsat 8 by using the dual-band method during the eruption on 6 September 2014 (The black box shows the location of the field measurement; further details are given in Appendix D); (b) Thickness comparison between the satellite derived estimates and field measurements.

6. Discussions

In Section 5.1, Sections 5.2 and 5.3, we have used TEI to automatically detect and derive thermal properties from infrared remotely-sensed data within the hotspot region defined by $TEI > 0.10$. This value provides encouragement that the TEI method yields robust estimates of hotspot anomalies during eruption. On the other hand, differentiating between thermal domains offers new possibilities to use different T_c setting for each domain to derive sub pixel temperature using the dual-band method. However, as explained by Lombardo and Buongiorno [13], the dual-band method provides a rough approximation to the thermal model when only two infrared bands are available. Figure 11a,b show comparison of active lava temperature obtained from satellite and forward looking infrared (FLIR) camera measurements during 2 December 2014 lava breakout in $64^{\circ}54.644'N$, $16^{\circ}42.931'W$. This comparison shows a good agreement for both satellite and field measurements. Satellite measurement yields T_h of $1096^{\circ}C$ in an area of $3.05 m^2$ which is 0.33% of the pixel size, meanwhile FLIR shows a

maximum temperature around 1047 °C for an area of 4.52 m². However, this comparison is a rough estimation, since the temperature is not uniform within the active lava. Therefore, we recommend further improvement by using more than two thermal components. We also performed an experiment to study the effect of different T_c on T_h for different thermal domains in this area. Figure 12 shows a logarithmic increase in T_h as T_c increases [28]; therefore, T_c is an important parameter for deriving precise temperature estimates from the dual-band method.

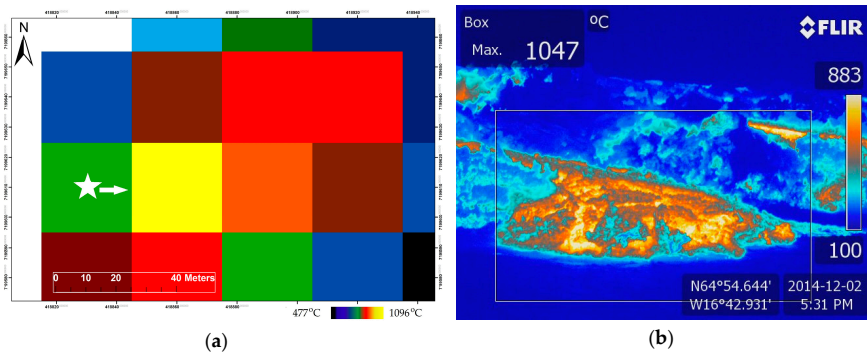


Figure 11. (a) Lava breakout (yellow pixel) temperature from satellite from 2 December 2014, white star and arrow show the measurement location and the camera direction, respectively; (b) Lava breakout temperature measurement from a FLIR camera on 2 December 2014. The box shows the area of interest.

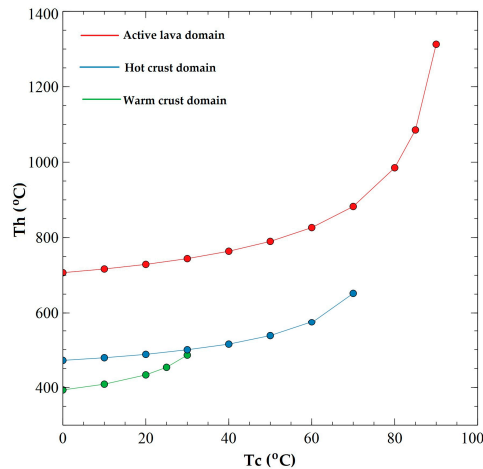


Figure 12. T_h as function of T_c on 2 December 2014. Dots and solid lines are the solutions from dual-band method and the logarithmic fitting respectively.

In Sections 5.4 and 5.5, we found that both the radiant flux estimate and crust thickness estimate agree closely with the field observations trends. In Figure 13a,b, we conduct an experiment by varying H: for very rough lava (H = 0.3), rough lava (H = 0.7) and perfectly smooth lava (H = 1). Smoother lava will produce the highest total radiant flux, but on the other hand, the crust becomes thinner. The higher H (0.7–1) agrees with the radiant flux peak result of Wright et al. [33] (~25 GW), since the effect of surface roughness are not accounted in their study. Interestingly, in the channel and northern part of the crust (Figure A4, points 1 to 6) results are produced that are closer to the field measurements; this means that the lava in those thermal domains is mostly dominated by rough surface (lower H). This is

in good agreement with field observations that show that brecciated surface is dominant in Holuhraun. Meanwhile, the southern part of the crust (Figure A4, points 10 to 15) is overestimated, which means that the H is higher (smoother surface) than we estimate. Simply, as we mentioned earlier, this is due to the temporal gap between field measurement and satellite. In Figure 14a,b, it is shown that the temperature of the channel decreases with distance from the vents and crust thickness increases from the vents on 6 September 2014 (Figure 7a); This trend has good agreement with past work from Oppenheimer during the Lonquimay eruption (Chile, 1989) [10] which showed such trends. However, the H parameter is still open for discussion, and we recommend performing an alternative method to determine H (e.g., airborne light detection and ranging (LIDAR) and terrestrial laser scanning) and varying H based on LIDAR model during future eruption in order to get a better estimate.

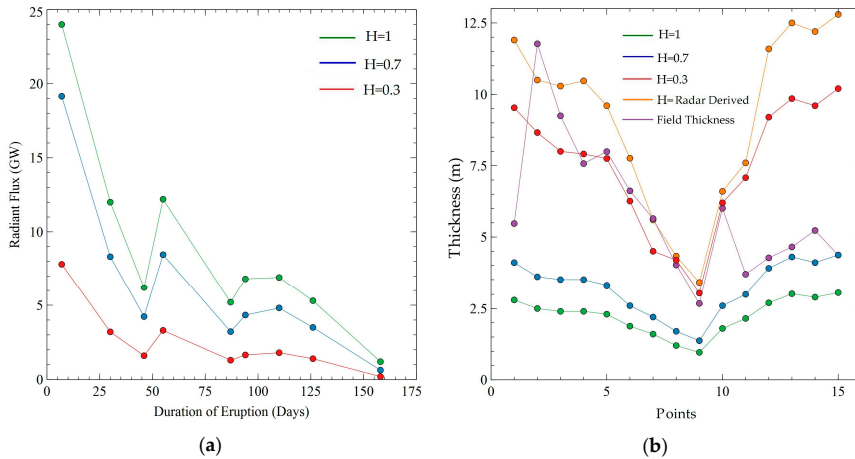


Figure 13. Different values of H comparison for (a) radiant flux; (b) crust thickness, with the ground-based thickness in purple.

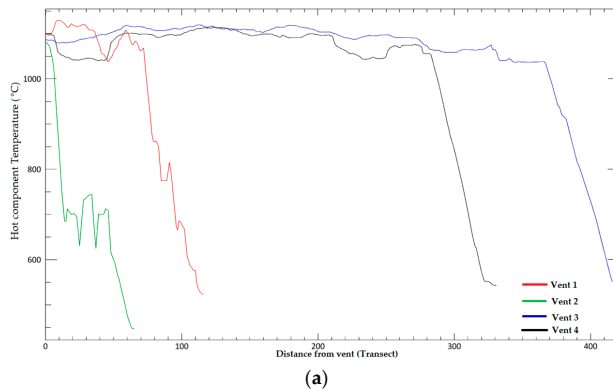


Figure 14. Cont.

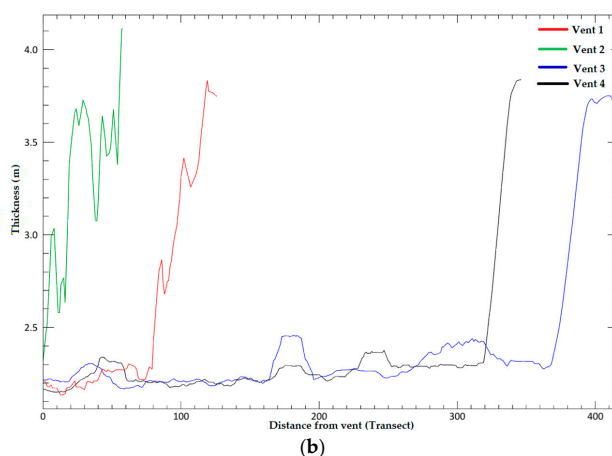


Figure 14. Trend for open channel lava flow on 6 September 2014 (a) temperature decrease as distance from the vent increases; (b) crust thickness increases as distance from the vent increases.

7. Conclusions

In this paper, we introduce a new spectral index called the thermal eruption index (TEI) based on the SWIR and TIR bands, allowing us to differentiate thermal domains within the lava flow field. TEI detects hotspots with $TEI > 0.10$: this value provides encouragement that the TEI method yields robust estimates of hotspot anomalies during eruption. Two main thermal domains were distinguished within the lava flow field. The first is the active lava domain, which is characterized by high TEI (0.51). The second is the crust domain surrounding active lava, characterized by TEI below active lava domain but exceeding the hotspot threshold (0.10–0.51). The result from 2 December 2014 shows that a temperature estimate (1096 °C; occupying area of 3.05 m²) from a lava breakout has a close correspondence with a thermal camera measurement (1047 °C; occupying area of 4.52 m²). This paper also considered effect of lava surface roughness effects by using the Hurst coefficient (H) for deriving the radiant flux (Φ_{rad}) and the crust thickness (Δh), where the higher H (smoother surface) produce thinner crust meanwhile the lower H (rough surface) will produce thicker crust. Crust thickness in the lava channel during 6 September 2014 (~3.4–7.7 m) compares closely with the lava height measurement from the field (~2.6–6.6 m); meanwhile, the total radiant flux peak is underestimated (~8 GW) compared to other studies (~25 GW), although the trend shows good agreement with both field observation and other studies. These results show that the proposed techniques were successfully applied to Landsat 8 on SWIR and TIR datasets from 2014–2015 Holuhraun eruptions. In future work, the proposed methods will be applied to other satellite/airborne datasets which have both SWIR and TIR band and consider alternative method to determined H (e.g., airborne LIDAR and terrestrial laser scanning). This study provides new insights for monitoring future effusive eruption using infrared satellite images.

Acknowledgments: The first author has been supported by the Indonesia Endowment Fund for Education (LPDP), Institute of Earth Science and Vinir Vatnajökuls during his Ph.D. project. Authors also would also like to thank anonymous reviewers for their constructive comments for the manuscript.

Author Contributions: All authors contributed to the work presented in this paper. Muhammad AUFARISTAMA, Magnus Orn Ulfarsson, and Ingibjorg Jonsdottir were in charge in remote sensing analysis and signal processing. Armann Hoskuldsson and Thorvaldur Thordarson were in charge in geological interpretation and field observation.

Conflicts of Interest: The authors declare no conflict of interest.

Appendix A

We derived the Hurst coefficient (H) using rescaled range analysis, known as the R/S technique [29], from a radar signal backscattering transects (H'). In this study we use Sentinel 1A VH polarization data that have been calibrated, speckle filtered and terrain corrected. Equation (A1) below models the relation between R/S and H' as

$$H' = \frac{\log(\frac{R}{S})}{\log(\tau)} \quad (\text{A1})$$

where R is the maximum and minimum value detected in the transect, S is the standard deviation of the time series, and τ is the measured time period. Here, we assume that surface roughness represents the lava thermal domain, active lava is smooth, hot crust is rough, and warm crust domain is very rough. This situation also can be seen clearly in radar backscattering on 18 October 2014 (Figure A1A). The lava channel has low backscattering (dark signal) due to smooth surface, on the other way very rough lava has strong backscattering (bright signal). We pick random transects from Figure A1A that represent the roughness shown in Figure A1B. These transect lines are then used to derive H' . We normalized H' by multiplying it by 0.5, since the study from Shepard et al. [30] shows that geological surface has a strong tendency to cluster around $H = 0.5$. According to this technique active lava has $H = 0.44$, hot crust has $H = 0.35$ and warm crust has $H = 0.21$.

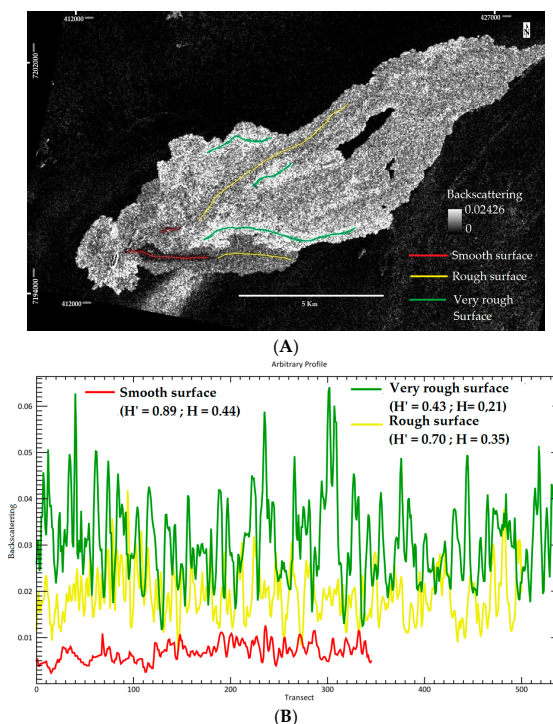


Figure A1. (A) Sentinel 1A VH polarization backscattering from 18 October 2014. The red, yellow and green transect represent smooth, rough and very rough surface, respectively; (B) Transect and Hurst coefficient that are derived from (A). According to this technique active lava has $H = 0.44$, hot crust has $H = 0.35$ and warm crust has $H = 0.21$.

Appendix B

Figure A2A–D show TEI anomaly on open channel flow during 29 September and 24 October.

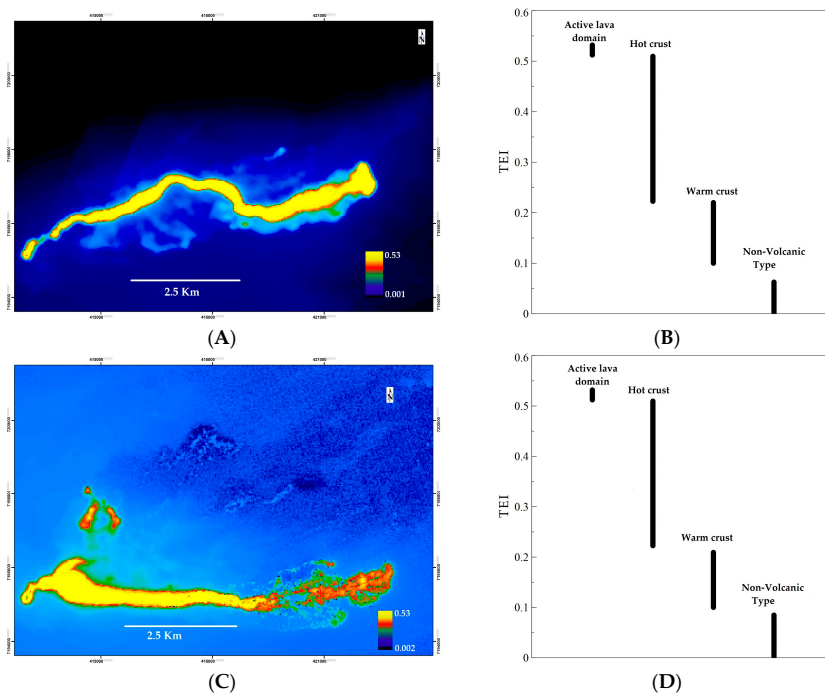


Figure A2. (A) Spatial distribution of TEI during 29 September 2014 eruption; (B) TEI differentiates four different thermal domains within the Holuhraun lava flow at 29 September 2014. TEI allows the active lava domain to be distinguished from crust domain and the non-volcanic hotspot domain. (C) Spatial distribution of TEI during 24 October 2014 eruption (D) TEI differentiates four different thermal domains within the Holuhraun lava flow at 24 October 2014. TEI allows the active lava domain to be distinguished from crust domain and the non-volcanic hotspot domain.

Appendix C

Here we plot T_h as a function of p and TEI with classification, respectively for 29 September 2014 and 24 October 2014, as shown in Figure A3A–F.

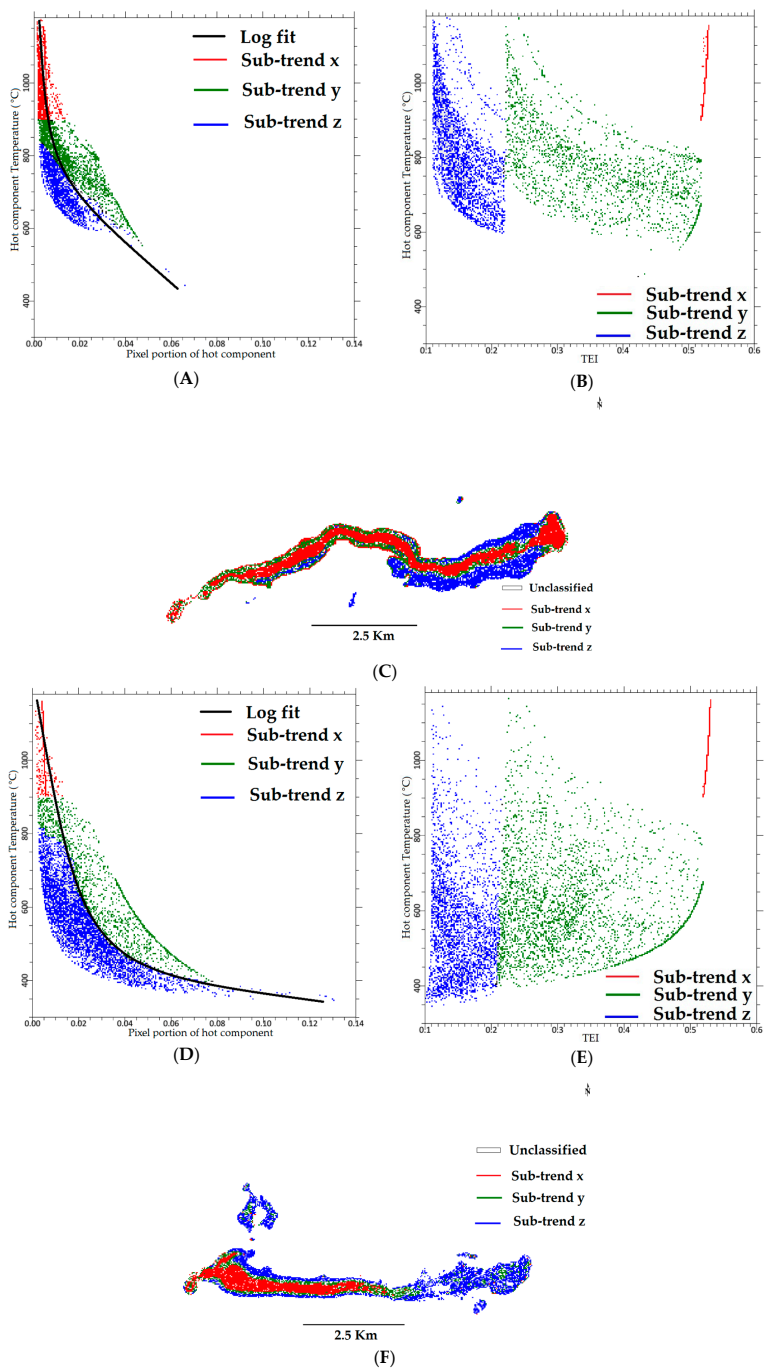


Figure A3. (A) Scatter plot of T_h vs. p ; (B) Scatter plot of T_h vs. TEI; (C) classification of lava thermal domain on 29 September 2014; (D) Scatter plot of T_h vs. p ; (E) Scatter plot of T_h vs. TEI; (F) classification of lava thermal domain on 24 October 2014.

Appendix D

The locations of the thickness measurement points are shown in Figure A4, where the arrows represent the order of points. The measurements were done using theodolite with certain distance and dates for each point. Table A1 shows the detailed acquisition from Figure A4 and a comparison with the satellite derived crust thickness estimate on 6 September 2014.

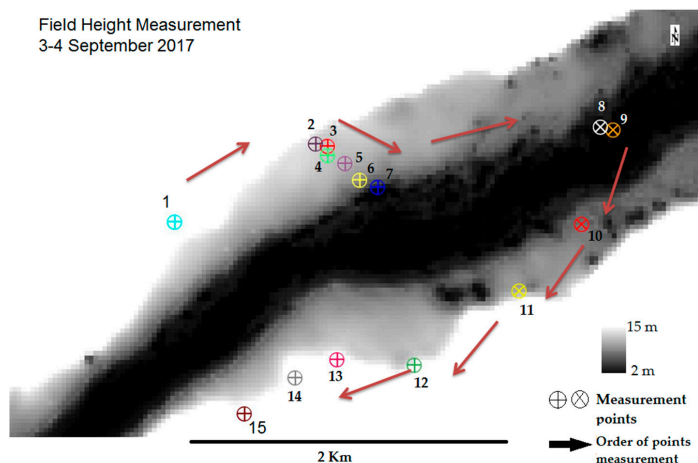


Figure A4. The Location of thickness measurement points, the arrows represent the order of points from 1 to 15.

Table A1. Detail of the lava height measurement during 3–4 September 2014 and a comparison with satellite derived crust thickness measurement on 6 September 2014.

Points	Height	Crust Thickness in 6 September 2014 from Satellite	Distance Points to Lava	Date
1	5.47336	11.9	72	2014-09-03T08:39:40Z
2	11.76946	10.5	144	2014-09-03T07:59:53Z
3	9.24672	10.29	144	2014-09-03T07:59:53Z
4	7.573852	10.47	84	2014-09-03T08:15:07Z
5	7.993413	9.6	90	2014-09-03T08:20:59Z
6	6.618929	7.76	35	2014-09-03T08:25:16Z
7	5.647851	5.6	41	2014-09-03T08:32:52Z
8	4.018422	4.33	21	2014-09-04T07:52:11Z
9	2.676691	3.4	13.3	2014-09-04T07:44:08Z
10	6.007832	6.6	34.1	2014-09-04T07:35:15Z
11	3.691354	7.6	16.7	2014-09-04T07:27:34Z
12	4.269408	11.59	17.4	2014-09-04T07:16:23Z
13	4.651991	12.5	23.7	2014-09-04T07:11:51Z
14	5.230504	12.2	24.5	2014-09-04T07:03:49Z
15	4.36857	12.8	20	2014-09-04T06:57:22Z

References

1. Pedersen, G.B.M.; Höskuldsson, A.; Dürig, T.; Thordarson, T.; Jónsdóttir, I.; Riishuus, M.S.; Óskarsson, B.V.; Dumont, S.; Magnusson, E.; Gudmundsson, M.T.; et al. Lava field evolution and emplacement dynamics of the 2014–2015 basaltic fissure eruption at Holuhraun, Iceland. *J. Volcanol. Geotherm. Res.* **2017**, *340*, 155–169. [[CrossRef](#)]

2. Pedersen, G.; Höskuldsson, A.; Riishuus, M.S.; Jónsdóttir, I.; Thórdarson, T.; Gudmundsson, M.T.; Durmont, S. Emplacement dynamics and lava field evolution of the flood basalt eruption at Holuhraun, Iceland: Observations from field and remote sensing data. In *EGU General Assembly*; European Geosciences Union: Vienna, Austria, 2016; Volume 18, p. 13961.
3. Kolzenburg, S.; Giordano, D.; Thordarson, T.; Höskuldsson, A.; Dingwell, D.B. The rheological evolution of the 2014/2015 eruption at Holuhraun, central Iceland. *Bull. Volcanol.* **2017**, *79*, 45. [[CrossRef](#)]
4. Icelandic Meteorological Office Holuhraun. Available online: <http://en.vedur.is/earthquakes-and-volcanism/articles/nr/3122> (accessed on 11 May 2017).
5. Thordarson, T.; Höskuldsson, Á. Postglacial volcanism in Iceland. *Jökull* **2008**, *58*, 197–228.
6. Dürig, T.; Gudmundsson, M.; Högnadóttir, T.; Jónsdóttir, I. Estimation of lava flow field volumes and volumetric effusion rates from airborne radar profiling and other data: Monitoring of the Nornahraun (Huluhraun) 2014/15 eruption in Iceland. In *European Geosciences Union, General Assembly*; European Geosciences Union: Vienna, Austria, 2015; Volume 17, p. 8519.
7. Gíslason, S.; Stefánsdóttir, G.; Pfeffer, M.A.; Barsotti, S.; Jóhannsson, T.; Galeczka, I.; Bali, E.; Sigmarsson, O.; Stefánsson, A.; Keller, N.S.; et al. Environmental pressure from the 2014–15 eruption of Bárðarbunga volcano, Iceland. *Geochem. Perspect. Lett.* **2015**, *1*, 84–93. [[CrossRef](#)]
8. Wright, R.; Rothery, D.A.; Blake, S.; Harris, A.J.L.; Pieri, D.C. Simulating the response of the EOS Terra ASTER sensor to high-temperature volcanic targets. *Geophys. Res. Lett.* **1999**, *26*, 1773–1776. [[CrossRef](#)]
9. Urai, M. Heat discharge estimation using satellite remote sensing data on the Iwodake volcano in Satsuma-Iwojima, Japan. *Earth Planets Space* **2002**, *54*, 211–216. [[CrossRef](#)]
10. Oppenheimer, C. Lava flow cooling estimated from Landsat Thematic Mapper infrared data: The Lonquimay Eruption (Chile, 1989). *J. Geophys. Res. Solid Earth* **1991**, *96*, 21865–21878. [[CrossRef](#)]
11. Harris, A.; Blake, S.; Rothery, D.A.; Stevens, N.F. A chronology of the 1991 to 1993 Mount Etna eruption using advanced very high resolution radiometer data: Implications for real-time thermal volcano monitoring. *J. Geophys. Res.* **1997**, *102*, 7985–8003. [[CrossRef](#)]
12. Abrams, M.; Pieri, D.; Realmuto, V.; Wright, R. Using EO-1 hyperion data as hyspIRI preparatory data sets for volcanology applied to Mt Etna, Italy. *IEEE J. Sel. Top. Appl. Earth Obs. Remote Sens.* **2013**, *6*, 375–385. [[CrossRef](#)]
13. Lombardo, V.; Buongiorno, M.F. Lava flow thermal analysis using three infrared bands of remote-sensing imagery: A study case from Mount Etna 2001 eruption. *Remote Sens. Environ.* **2006**, *101*, 141–149. [[CrossRef](#)]
14. Lombardo, V.; Silvestri, M.; Spinetti, C. Near real-time routine for volcano monitoring using infrared satellite data. *Ann. Geophys.* **2011**, *54*, 522–534.
15. Wright, R.; Garbeil, H.; Harris, A.J.L. Using infrared satellite data to drive a thermo-rheological/stochastic lava flow emplacement model: A method for near-real-time volcanic hazard assessment. *Geophys. Res. Lett.* **2008**, *35*, 1–5. [[CrossRef](#)]
16. Lombardo, V.; Buongiorno, M.F.; Pieri, D.; Merucci, L. Differences in Landsat TM derived lava flow thermal structures during summit and flank eruption at Mount Etna. *J. Volcanol. Geotherm. Res.* **2004**, *134*, 15–34. [[CrossRef](#)]
17. Wright, R.; Garbeil, H.; Davies, A.G. Cooling rate of some active lavas determined using an orbital imaging spectrometer. *J. Geophys. Res. Solid Earth* **2010**, *115*, 1–14. [[CrossRef](#)]
18. Piscini, A.; Lombardo, V. Volcanic hot spot detection from optical multispectral remote sensing data using artificial neural networks. *Geophys. J. Int.* **2014**, *196*, 1525–1535. [[CrossRef](#)]
19. Dozier, J. A method for satellite identification of surface temperature fields of subpixel resolution. *Remote Sens. Environ.* **1981**, *11*, 221–229. [[CrossRef](#)]
20. Harris, A. *Thermal Remote Sensing of Active Volcanoes: A User's Manual*; Cambridge University Press: Cambridge, UK, 2013.
21. Lombardo, V.; Merucci, L.; Buongiorno, M.F. Wavelength influence in sub-pixel temperature retrieval using the dual-band technique. *Ann. Geophys.* **2006**, *49*, 227–234.
22. Blackett, M. An Overview of Infrared Remote Sensing of Volcanic Activity. *J. Imaging* **2017**, *3*, 13. [[CrossRef](#)]
23. Oppenheimer, C.; Rothery, D.A.; Pieri, D.C.; Abrams, M.J.; Carere, V. Analysis of Airborne Visible/Infrared Imaging Spectrometer (AVTRIS) data of volcanic hot spots. *Int. J. Remote Sens.* **1993**, *14*, 2919–2934. [[CrossRef](#)]
24. Wright, R.; Flynn, L.; Garbeil, H.; Harris, A.; Pilger, E. Automated volcanic eruption detection using MODIS. *Remote Sens. Environ.* **2002**, *82*, 135–155. [[CrossRef](#)]

25. Di Martino, G.; Iodice, A.; Riccio, D.; Ruello, G. Volcano monitoring via fractal modeling of lava flows. In Proceedings of the 2008 2nd Workshop on Use of Remote Sensing Techniques for Monitoring Volcanoes and Seismogenic Areas, USReST 2008, Naples, Italy, 11–14 November 2008.
26. Dharmawan, I.A.; Ulhag, R.Z.; Endyana, C.; AUFARISTAMA, M. Numerical Simulation of non-Newtonian Fluid Flows through Fracture Network. *IOP Conf. Ser.* **2016**, *29*, 12030. [[CrossRef](#)]
27. Pieri, D.C.; Glaze, L.S.; Abrams, M.J. Thermal radiance observations of an active lava flow during the June 1984 eruption of Mount Etna. *Geology* **1990**, *18*, 1018–1022. [[CrossRef](#)]
28. Ferrucci, F.; Hirn, B. Automated monitoring of high-temperature volcanic features: From high-spatial to very-high-temporal resolution. *Geol. Soc. Lond. Spec. Publ.* **2016**, *426*, 159–179. [[CrossRef](#)]
29. Martinez, O.S.; Cruz, D.M.; Chavarin, J.U.; Bustos, E.S. Rough Surfaces Profiles and Speckle Patterns Analysis by Hurst Exponent Method. *J. Mater. Sci. Eng.* **2014**, *3*, 759–766.
30. Shepard, M.K.; Campbell, B.A.; Bulmer, M.H.; Farr, T.G.; Gaddis, L.R.; Plaut, J.J. The roughness of natural terrain: A planetary and remote sensing perspective. *J. Geophys. Res. Planets* **2001**, *106*, 32777–32795. [[CrossRef](#)]
31. Reynolds, H.I.; Gudmundsson, M.T.; Högnadóttir, T.; Magnússon, E.; Pálsson, F. Subglacial volcanic activity above a lateral dyke path during the 2014–2015 Bárðarbunga-Holuhraun rifting episode, Iceland. *Bull. Volcanol.* **2017**, *79*, 38. [[CrossRef](#)]
32. Rothery, D.A.; Francis, P.W.; Wood, C.A. Volcano monitoring using short wavelength infrared data from satellites. *J. Geophys. Res.* **1988**, *93*, 7993–8008. [[CrossRef](#)]
33. Wright, R.; Blackett, M.; Hill-Butler, C. Some observations regarding the thermal flux from Earth’s erupting volcanoes for the period of 2000 to 2014. *Geophys. Res. Lett.* **2015**, *42*, 282–289. [[CrossRef](#)]
34. Rossi, C.; Minet, C.; Fritz, T.; Eineder, M.; Bamler, R. Temporal monitoring of subglacial volcanoes with TanDEM-X—Application to the 2014-2015 eruption within the Bárðarbunga volcanic system, Iceland. *Remote Sens. Environ.* **2016**, *181*, 186–197. [[CrossRef](#)]




© 2018 by the authors. Licensee MDPI, Basel, Switzerland. This article is an open access article distributed under the terms and conditions of the Creative Commons Attribution (CC BY) license (<http://creativecommons.org/licenses/by/4.0/>).

Paper II: The 2014–2015 Lava Flow Field at Holuhraun, Iceland: Using Airborne Hyperspectral Remote Sensing for Discriminating the Lava Surface

Article

The 2014–2015 Lava Flow Field at Holuhraun, Iceland: Using Airborne Hyperspectral Remote Sensing for Discriminating the Lava Surface

Muhammad Aumaristama ^{1,*}, Armann Hoskuldsson ¹, Magnus Orn Ulfarsson ²,
Ingibjorg Jonsdottir ^{1,3} and Thorvaldur Thordarson ^{1,3}

¹ Institute of Earth Sciences, University of Iceland, Sturlugata 7, 101 Reykjavík, Iceland; armh@hi.is (A.H.); ij@hi.is (I.J.); torvth@hi.is (T.T.)

² Faculty of Electrical and Computer Engineering, University of Iceland, Hjardarhagi 2-7, 107 Reykjavik, Iceland; mou@hi.is

³ Faculty of Earth Sciences, University of Iceland, Sturlugata 7, 101 Reykjavík, Iceland

* Correspondence: mua2@hi.is; Tel.: +354-855-1242

Received: 31 January 2019; Accepted: 18 February 2019; Published: 26 February 2019



Abstract: The Holuhraun lava flow was the largest effusive eruption in Iceland for 230 years, with an estimated lava bulk volume of $\sim 1.44 \text{ km}^3$ and covering an area of $\sim 84 \text{ km}^2$. The six month long eruption at Holuhraun 2014–2015 generated a diverse surface environment. Therefore, the abundant data of airborne hyperspectral imagery above the lava field, calls for the use of time-efficient and accurate methods to unravel them. The hyperspectral data acquisition was acquired five months after the eruption finished, using an airborne FENIX-Hyperspectral sensor that was operated by the Natural Environment Research Council Airborne Research Facility (NERC-ARF). The data were atmospherically corrected using the Quick Atmospheric Correction (QUAC) algorithm. Here we used the Sequential Maximum Angle Convex Cone (SMACC) method to find spectral endmembers and their abundances throughout the airborne hyperspectral image. In total we estimated 15 endmembers, and we grouped these endmembers into six groups; (1) basalt; (2) hot material; (3) oxidized surface; (4) sulfate mineral; (5) water; and (6) noise. These groups were based on the similar shape of the endmembers; however, the amplitude varies due to illumination conditions, spectral variability, and topography. We, thus, obtained the respective abundances from each endmember group using fully constrained linear spectral mixture analysis (LSMA). The methods offer an optimum and a fast selection for volcanic products segregation. However, ground truth spectra are needed for further analysis.

Keywords: hyperspectral; FENIX; lava field; SMACC; LSMA

1. Introduction

Lava flow emplacement is an important constructive geological process that contributes to reshaping natural landscapes [1–3]. To assess the hazards and long-term impacts posed by lava flows, it is vital to understand aspects such as the return period of effusive eruptions, to map the areas covered by eruptions in the past and to characterize the evolution of lava flow surfaces after emplacement [4,5]. In high eruption frequency areas, lava flows often overlap each other. If the overlapping lava flows erupt within a short time span and have similar chemical and surface characteristics, discrimination will be further complicated by their similar spectral signatures. Spectral reflectance plays an important role in visible and shortwave infrared (VIS-SWIR) remote sensing. Each material absorbs and reflects the incoming radiation in a characteristic way. In the 400–2500 nm range, minerals display absorption features due to the interaction of light with cations (Fe, Mg, Al) and anions (OH, CO₃) [6]. Reflectance spectra provide information about the specific material and their composition. They are used for

different applications such as classification of remotely sensed data, identification of mineral features of rock, and environmental assessment [7,8]. The interest in reflectance spectra of volcanic rocks has increased recently as they can play an important role as planetary analogues. In fact, these spectra can be used to identify compounds by data acquired by ongoing solar system exploration missions [9,10].

Characterization of surface spectral reflectance by satellite remote sensing is constrained by the spectral range and resolution (i.e., number of spectral bands) as well as by the spatial resolution of the imagery. Whereas multispectral imagery can be acquired at very high spatial resolution (e.g., WorldView [11,12]); the spatial resolution of hyperspectral satellite data remains low (e.g., EO-1 Hyperion with a ground resolution of 30 m × 30 m); and spectral mixing is thus a major issue [13]. The spectral reflectance of lava of different compositions has also been documented using laboratory spectrometry with decimeter-size samples [14]. For accessible volcanic terrains, field spectrometry offers a useful alternative approach for characterizing the spectral reflectance of contrasted lava surfaces and for documenting its spatial variation at different spatial scales [5,14]. The great variety of morphologies observed in the 2014–2015 Holuhraun lava flows [1,15] encouraged a detailed study of their spectral characteristics, to obtain information about lava composition and detect possible differences in the spectra of the flow. In spectroscopy, the identification of the mineral constituents of major rock types is typically approached using spectral unmixing methods [5,16]. Usually, in the visible and near-infrared spectral range, mafic rocks are characterized by very low reflectance due to the presence of large amounts of dark mafic minerals [14]. The 2014–2015 lava flow at Holuhraun in NE Iceland offers an excellent diverse surface environment for investigating and characterizing lava deposits. Its intense volcanic activity [1,17–19], geomorphological complexity [20], and well-documented flank eruptions [1] perplex the remote sensing monitoring of the bulk volcanic edifice. However, the detailed field mapping of lithologies is frequently obstructed by difficulties in accessibility, the scale of lava flow fields, topography, while remote sensing has become increasingly important in mapping volcanic terrains and specifically in mapping lava flows. Mapping individual lava flows using satellite remote sensing is challenging for at least three reasons: vegetation cover, spatial overlapping, and spectral similarity [3,4]. Moreover, a high eruption frequency often leads to lava flows overlapping each other. If the overlapping lava flows are erupted within a short period and have similar chemical and surface characteristics, discrimination will be further complicated by their similar spectral signatures.

Hyperspectral remote sensing provides information on hundreds of distinct and contiguous channels of the electromagnetic spectrum, thus enabling the identification of multiple ground objects through their detailed spectral profiles. However, restrictions on the spatial resolution of hyperspectral data, the multiple scattering of the incident light between objects, and microscopic material mixing form the mixed pixel problem. Pixels are identified as mixed when they are composed of the spectral signatures of more than one ground object. Therefore, we adopted linear spectral mixture analysis (LSMA) techniques [8,21], which model the pixel spectra as a combination of pure components (endmembers) weighted by the fractions (abundances) that contribute to the total reflectance of the mixed pixel [22]. Ideally, each selected endmember from the hyperspectral image under study has the maximum possible abundance of a single physical material present and minimum abundance of the rest of the physical materials. Spectral unmixing typically consists of two main substages: (a) endmember extraction; and (b) abundance estimation [22]. In this paper, we focus on both endmember extraction and estimation of fractional abundances of the lava field products on 2014–2015 Holuhraun lava fields. For this purpose, an airborne hyperspectral image with an AisaFENIX sensor on board a NERC Airborne Research Facility (Natural Environment Research Council Airborne Research Facility) campaign was acquired at Holuhraun after the eruption and for the sub-pixel analysis we used the sequential maximum angle convex cone (SMACC) algorithm to identify the spectral image endmembers while the LSMA method was employed to retrieve the abundances. Our approach was narrowed to the eruptive fissure vent part since it is considered to have a more diverse surface. The resulting abundances from the LSMA method were both quantitatively and qualitatively compared with the spectral indices technique, aerial and field photographs, respectively. The objective was to

retrieve the main lava surface type contributing to the signal recorded by airborne hyperspectral at the very top surface of Holuhraun.

2. The 2014–2015 Eruption at Holuhraun

The eruption took place in the tectonic fissure swarm between the Bárðarbunga-Veiðivötn and the Askja volcanic systems (Figure 1a). It lasted about six months (31 August 2014 to 27 February 2015) and produced a bulk volume $\sim 1.44 \text{ km}^3$ of basaltic lava [1]. Lava effusion rates during the eruption period range from 320 to $10 \text{ m}^3/\text{s}$. Averaged values are ~ 250 , 100, and $50 \text{ m}^3/\text{s}$ during the initial (August–September 2014), intermediate (October–December 2014) and final phase (December 2014 to February 2015), respectively [1,17] (Figure 1b). The lava was emplaced on the sandur plains (glacial outwash sediment plains) north of the Vatnajökull/Dyngjufjökull glacier, partially covering the previous two Holuhraun lava flow fields south of the Askja caldera [1]. The area is gently sloping (average inclination $<0.5\%$; i.e., $\sim 0.3^\circ$) to the east-northeast. The shallow gradient resulted in low topographic forcing of the flow and, therefore, rather slow lava flow advance. During its emplacement history, the lava field was initially dominated by channels and horizontal expansion. Then it transitioned to grow in volume primarily by inflation, tube-fed flow (i.e., transport of lava through roofed over partially or filled channels) and vertical stacking of lava-lobes. The 2014–2015 effusive eruption products originate from intense activity in the vent, in which high oxidation occurs in this area. The main lava channel shows significant inflation (5–10 m). Lava advancement rates were generally low $\sim 0.0167 \text{ m/s}$ during the initial eruption phase [1] and dropped to $\sim 0.0017 \text{ m/s}$ during the middle of November 2014 [23]. The six-month-long effusive eruption features diverse surface structures and morphologies. The 2014–2015 lava flow at Holuhraun in NE Iceland offers an excellent diverse surface environment to investigate and characterize lava deposits.

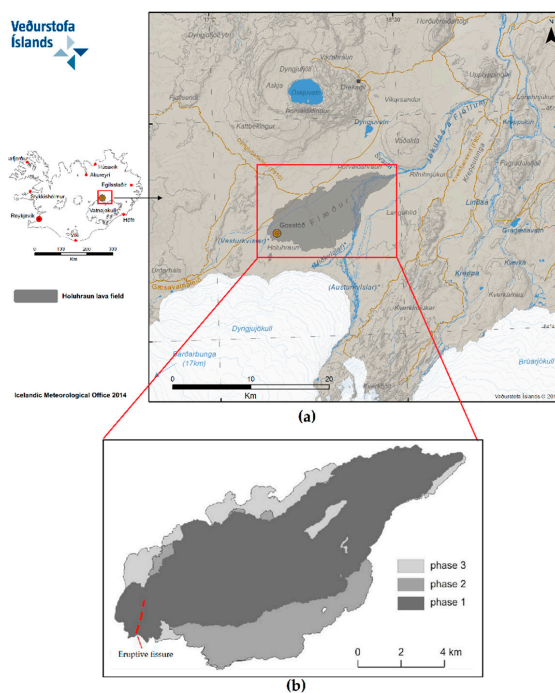


Figure 1. Bárðarbunga volcano and the Holuhraun lava flow field. (a) geological setting by the Icelandic Meteorological Office (after modification) [24], (b) coverage of the three main phases after Pedersen et al [1].

3. Spectral Unmixing on Lava

Various spectroscopy studies [2,5,7,14,25] over the volcanic area have examined the mineralogical composition of the extensive lava fields. Usually, in the visible (VIS) and near-infrared (NIR) spectral range, mafic rocks are characterized by very low reflectance due to the presence of large amounts of dark mafic minerals [14]. Spectral indices provide the first efficient way to emphasize subtle spectral variations at the surface [26]. More elaborate methods have been developed to discriminate and quantify mixtures of mafic minerals. They have been used to derive composition maps of mafic minerals [27–29]. However, some lava flows can have a similar chemical/mineralogical composition but dissimilar spectral behaviour due to the different grain size, surface texture, and presence of weathering [13,14]. The main components of igneous rocks do not display any peculiar spectral features in the visible and near infrared spectral range. In the case of basalts, the only spectral feature commonly found is an absorption peak, due to iron, located around 1000 nm [26]. However, in the case of hydrothermal alteration, hydroxyl bearing minerals show distinctive absorption features in the 2000–2500 nm spectral region [30]. Because of the heterogeneity of the lava surface, mixed pixels are very common which is illustrated in Figure 2a,b.

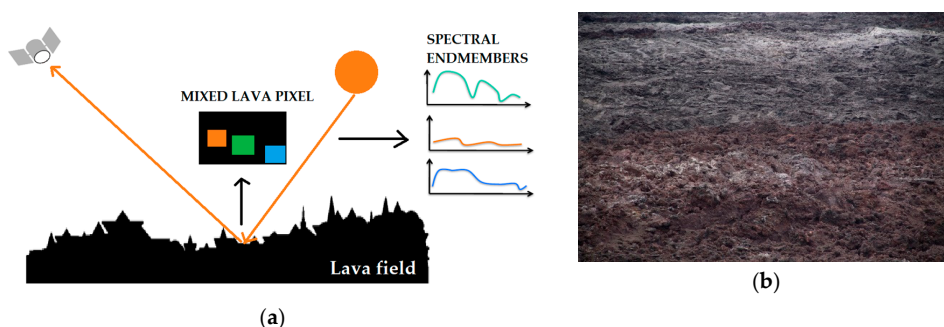


Figure 2. Illustration of (a) the mixed pixel in the lava surface caused by the presence of small, sub-pixel targets within the area; (b) variability of lava surfaces in Holuhraun lava field which include the oxidizing surface, sulfate mineral, and lava.

Spectral Mixing Analysis (SMA) has been specifically developed to account for mixtures [10]. Analysis of the data sample can simply be performed on these abundance fractions rather than the sample itself. This method is well-suited for spectroscopic analysis because most of the spectral shapes are due to different materials. The signal detected by a sensor at a single pixel is frequently a combination of numerous disparate signals. Unmixing techniques were applied to the volcano of Nyamuragira for discriminating lava flows of different ages by Li et al. [5]. The most recent study by Daskalopoulou et al. [16], used unmixing techniques to segregate lava flows and related products from the historical Mt. Etna. Nonetheless, there are no findings concerning lava flow delineation through unmixing in Iceland.

4. Data Acquisitions and Methods

4.1. Airborne Hyperspectral Data Acquisitions

Airborne hyperspectral data were acquired on 4 September 2015 between 16.56 and 17.58 (local time) with an AisaFENIX sensor (Specim, Spectral Imaging Ltd, <http://www.specim.fi>) [31] on board a NERC Airborne Research Facility (Natural Environment Research Council Airborne Research Facility <http://www.bas.ac.uk/nerc-arf>) aircraft [32]. Pushbroom VNIR and SWIR sensor, are two separate detectors with common fore-optics. The hyperspectral data contain 622 channels with spectral range from ~400 nm to 2500 nm (break at ~970 nm). The pixel size of this data is explained in Section 4.2.2.

In total, eight flights were acquired at the Holuhraun lava flow during this period with an average altitude of 2.4 km (Figure 3a). The data are delivered as level 1b ENVI BIL format files which means that radiometric calibration algorithms have been applied and navigation information has been synced to the image data (Figure 3b). In this study, we subset the data to focus on the area around the eruptive fissures vent (Figure 3c) which is thought to have a diverse surface and has field photographs. Very high-resolution aerial photographs of the lava field (0.5 m spatial resolution) from Loftmyndir ehf (<http://www.loftmyndir.is/>) [33] were used for comparison and validation of the unmixing results.

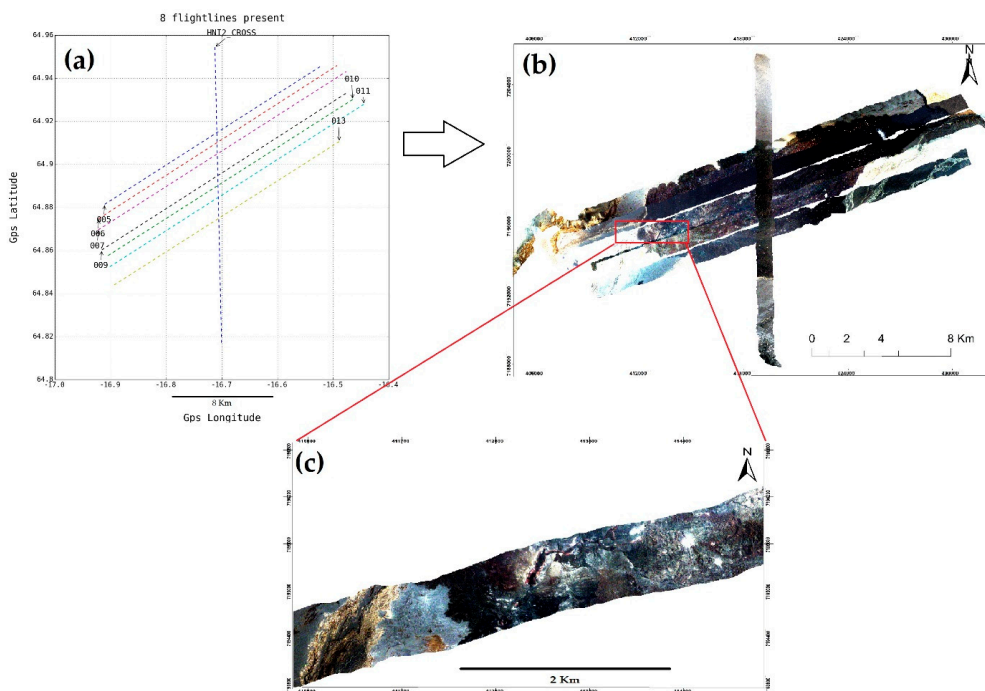


Figure 3. (a) Map showing line acquisition of FENIX hyperspectral image in the Holuhraun lava field; (b) Image mosaic from eight FENIX lines collected during the campaign (red box shows the image subset location); (c) Image subset of the focusing study area in the eruptive fissure vent of Holuhraun.

4.2. Spectral Unmixing and Abundance Retrieval

The processing workflow towards unmixing and generating abundance consists of four steps: (1) Atmospheric correction to retrieve surface reflectance; (2) Data masking, geocorrection, reprojection, and resampling; (3) An endmember selection algorithm was adopted to select the endmembers; then a linear spectral mixing analysis method was employed to retrieve the abundance (Figure 4).

4.2.1. Atmospheric Correction

Remote-sensing applications require removing the atmospheric effect from the imagery, to retrieve the spectral reflectance of the surface materials. In this study, the data were atmospherically corrected using the quick atmospheric correction (QUAC) algorithm [34,35], since we had no prior knowledge to perform empirical calibration [36,37]. QUAC is an in-scene approach, requiring only an approximate specification of sensor band locations (i.e., central wavelengths) and their radiometric calibration; no additional metadata is required [35]. QUAC does not involve first principles radiative transfer calculations, and therefore it is significantly faster than physics-based methods; however, it is also more approximate [35].

4.2.2. Data Masking, Geocorrection, Reprojection, and Resampling

In this study, we use the Airborne Processing Library (APL) software for processing the data [38]. The first step of the APL processing is to apply the mask of bad channels to atmospherically corrected data, creating a new file with bad channels set to zero (Appendix A on Figure A1). The next step uses the navigation file, the view vector file, and the digital elevation file (DEM) to calculate the ground position for each pixel then change the projection to UTM (Universal Transverse Mercator) Zone 28N [38]. We used satellite-based ASTER sensor for the DEM. In the final step we resampled output pixel size to ~3.5 m according to the height above ground level (AGL) that is given by the theoretical pixel size chart that can be found in Appendix A on Figure A2 (<https://nerc-arf-dan.pml.ac.uk/trac/wiki/Processing/PixelSize>) [39].

4.2.3. Endmembers Selection

The conventional image-based endmember selection approach based on scatterplots of the image bands may not be effective in identifying a sufficient number of endmembers. In this paper, we employed the sequential maximum angle convex cone (SMACC) algorithm [34] to identify spectral image endmembers. Endmembers are spectra that represent pure surface materials in a spectral image. The extreme points were used to determine a convex cone, which defined the first endmember. A constrained oblique projection was applied to the existing cone to derive the next endmember. The cone was then increased to include a new endmember [8,40]. This process was repeated until a projection derived an endmember that already existed within the convex cone, or until a specified number of endmembers was satisfied [21]. When implemented with SMACC, the output endmember number was set as 5, 10, 15, 20, and 30 respectively. Better endmembers could be identified easily from the 15 endmembers output (more detail in Section 6.2). Then, we used the selected 15 endmembers for deriving the abundance.

4.2.4. Linear Spectral Mixture Analysis

The linear spectral mixture analysis (LSMA) approach was adopted to calculate the abundance of endmembers for each pixel. LSMA assumes that the spectrum measured by a sensor is a linear combination of the spectra of all components (endmembers) within the pixel, and the spectral proportions of the endmembers (i.e., their abundance) reflect the proportion of area covered by distinct features on the ground [8,21]. The general equation for linear spectral mixing can be expressed as:

$$R_{ij,\lambda} = \sum_{n=1}^N p_{ij,n} R_{n,\lambda} + E_{\lambda} \quad (1)$$

where $R_{ij,\lambda}$ is the measured reflectance at wavelength λ for pixel ij , where i is the column pixel number, and j is the line pixel number; $p_{ij,n}$ is the fraction of endmembers n contributing to the image spectrum of pixel ij ; N is the total number of endmembers; $R_{n,\lambda}$ is the reflectance of endmember n at wavelength λ ; and E_{λ} is the error at wavelength λ of the fit of N spectral endmembers. The fraction $p_{ij,n}$ can be solved using a least-square method with fully constrained unmixing. Fully constrained unmixing means that the sum of the endmember fractional (abundance) values for each pixel must equal unity, which requires a complete set of endmembers. Therefore, it should meet the following two conditions:

$$0 \leq p_{ij,n} \leq 1 \quad (2)$$

$$\sum_{n=1}^N p_{ij,n} = 1 \quad (3)$$

In the majority of cases, the unmixing is only partially constrained because the extracted endmember set is incomplete for the image and only term (2) (i.e., Equation (2)) is satisfied. In this

study, fully constrained LSMA were applied to the FENIX image to obtain the abundance result and both SMACC and LSMA were executed by ENVI 5.3 and IDL 8.5 language programming.

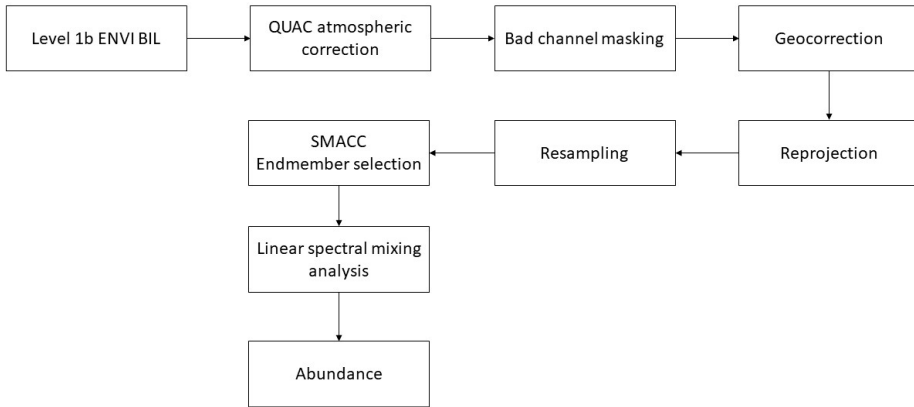


Figure 4. The workflow processing to derive an abundance map from the FENIX hyperspectral data

5. Results

5.1. Endmember Groups

The approximate locations of the 15 endmembers selected are shown in Figure 5a. SMACC first finds the brightest spectral in the image and defines it as the first endmember. In this study, the first endmember (endmember 1) represented saturated hot material. We grouped these 15 endmembers into six groups; (1) basalt; (2) hot material; (3) oxidized surface; (4) sulfate mineral; (5) water; and (6) noise (Figure 5b–g). These groups were based on the similar shape of the endmembers with the USGS spectral library; however, the amplitude of the endmembers within a group vary due to illumination conditions, spectral variability, and topography. We added up the abundances within the group to derive the abundance according to this endmembers group.

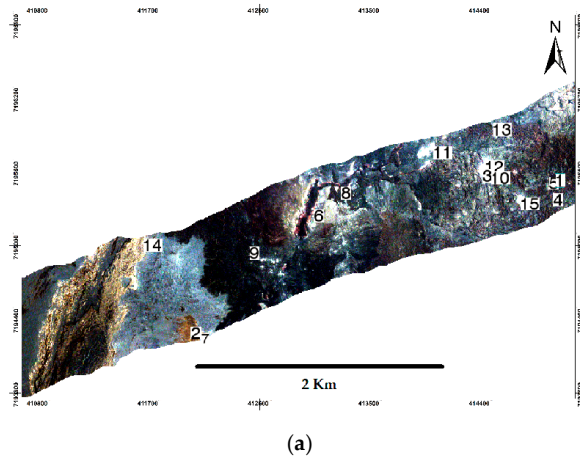


Figure 5. Cont.

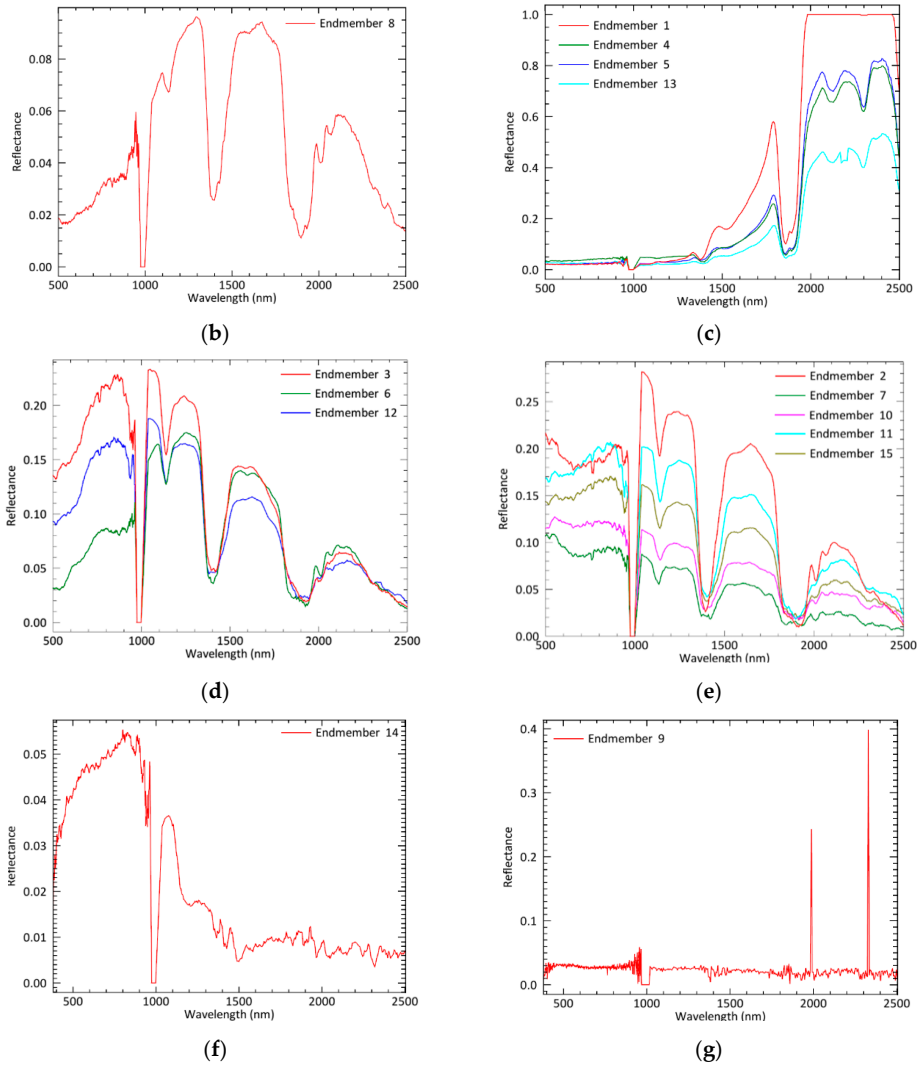


Figure 5. (a) The spatial distribution of 15 endmembers extracted by SMACC; The numbers on the image indicate the approximate location of the pixels selected as the represented endmembers of (b) basalt; (c) hot material; (d) oxidized surface; (e) sulfate mineral; (f) water; and (g) noise, extracted by SMACC.

5.2. Basalt Abundance

Figure 6a indicates the presence of the dominant basalt abundance pixel throughout the image. This abundance is associated with endmember 8 which is characterized by very low reflectance (Figure 5b) due to the presence of large amounts of dark mafic rock since the study area is dominated by basaltic lava (Figure 6b).

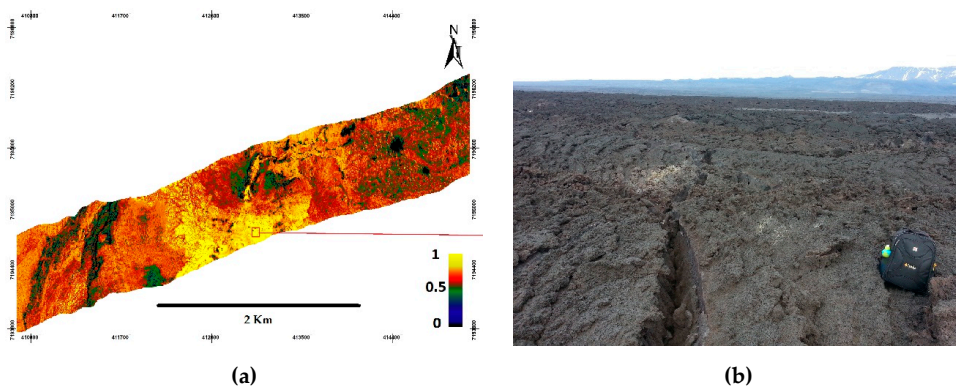


Figure 6. (a) The abundance map for basalt endmember, yellow areas indicate the highest fraction of basalt meanwhile the black areas indicate the lowest fraction of basalt (the red box shows the approximate location of the field photo); (b) field photograph of basaltic lava field of the Holuhraun.

5.3. Hot Material Abundance

As shown in Figure 7a, the hot material abundance map is very sparse. This abundance is described as blends of the endmember 1, 4, 5, and 13 which are characterized by very high reflectance in the SWIR due to the presence of hot material (Figure 5c). Figure 5a shows that endmembers 1, 4, 5, and 13 are located in the lower right corner and the upper part of the image, Figure 7b shows a false color (NIR-SWIR) image which agrees with the abundance map, i.e., some patches of hot material (red-yellow color) exist in the area. The false color image is created by stacking R: 2200 nm; G: 1600 nm, and B: 896 nm. This indicates that the lava field is still emitting hot material during the data acquisition.

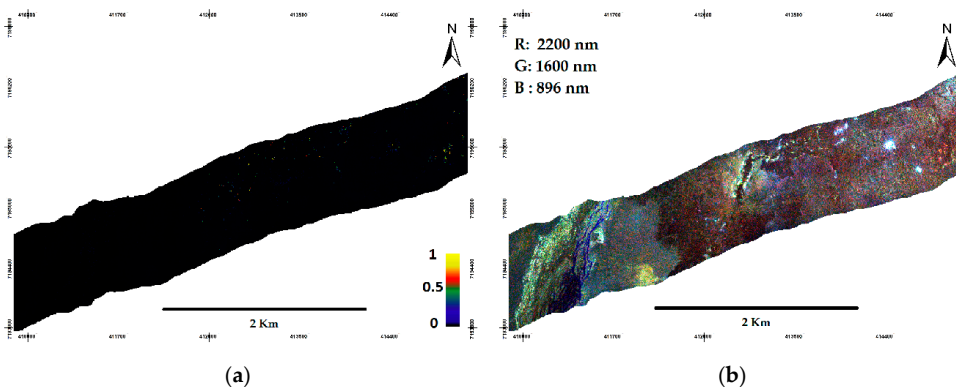


Figure 7. (a) Abundance map for the hot material endmember, yellow areas indicate the highest fraction of hot material meanwhile the black areas indicate the lowest fraction of incandescent lava; (b) The false color (NIR-SWIR) image show that hot material (red-yellow color) exists in the area.

5.4. Oxidized Surface Abundance

The oxidized surface endmembers (3, 6, and 12) have the highest abundance fraction at the vent as shown in Figure 8a. This agrees with a field observation shown in Figure 8b which highlights the matching dominant oxidized surface at the vent wall.

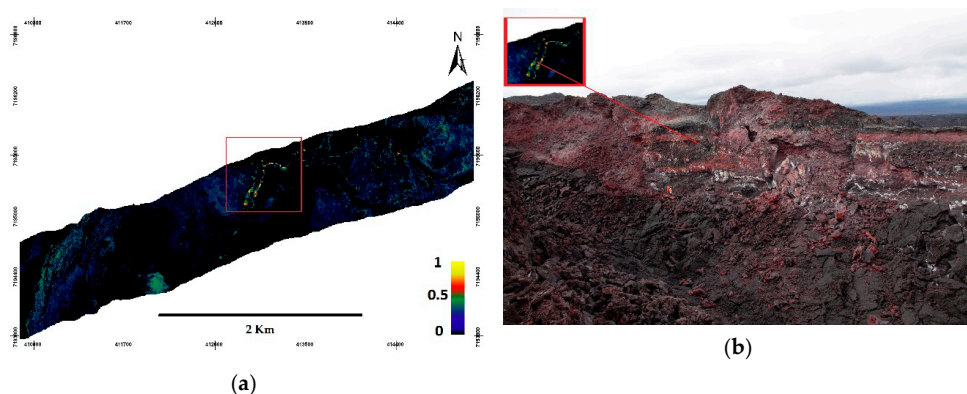


Figure 8. (a) Abundance map oxidized surface endmember; yellow areas indicate the highest fraction of oxidized surface meanwhile the black areas indicate the lowest fraction of oxidized surface; (b) Field photograph of an oxidized surface of the vent wall (red box and the line shows the approximate location of the field photograph)

5.5. Sulfate Mineral Abundance

The sulfate mineral endmembers (2, 7, 10, 11, and 15) have the highest abundance fraction around the lava pond and there are four most prominent areas for the sulfate (Figure 9a). This surface mineral looked as if it had been dusted by snow (white color) commonly identified as *thernadite* (Na_2SO_4) [41]. This can be directly seen from a true color image. This mineral formed as the flow cooled, a thin sublimate coating formed on the surface of the lava [41]. Figure 9b,c shows the *thernadite* formed in surface lava at Holuhraun.

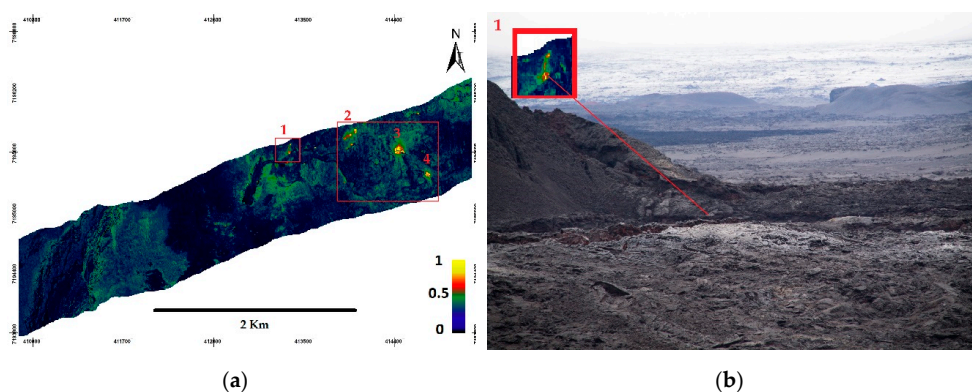
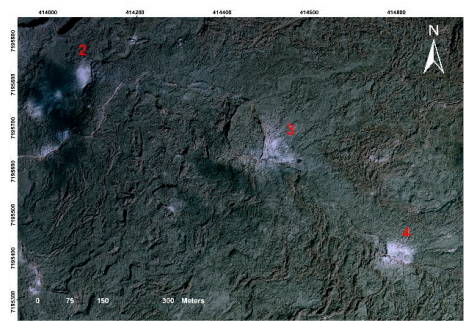


Figure 9. Cont.



(c)

Figure 9. (a) The Abundance map for the sulfate mineral endmember, the yellow areas indicate the highest fraction of sulfate mineral meanwhile the black areas indicate the lowest fraction of the sulfate mineral; (b) Field photograph of sulfate mineral (white surface) formed on the surface of lava (the red boxes and lines show the approximate location of the field and aerial photo respectively); (c) aerial photograph of sulfate mineral (white surface) formed on the surface of lava (The numbers on the image indicate the approximate location of the sulfate for both the abundance and photograph).

5.6. Water Abundance

The water abundance (Figure 10a) has the highest abundance fraction at the location mainly recognized as a glacial river (Figure 10b). Endmember 14 represents water which is characterized by a relatively low reflectance and has the highest reflectance in the blue wavelength. Water has high absorption and virtually no reflectance in the NIR-SWIR wavelengths range (Figure 5f).

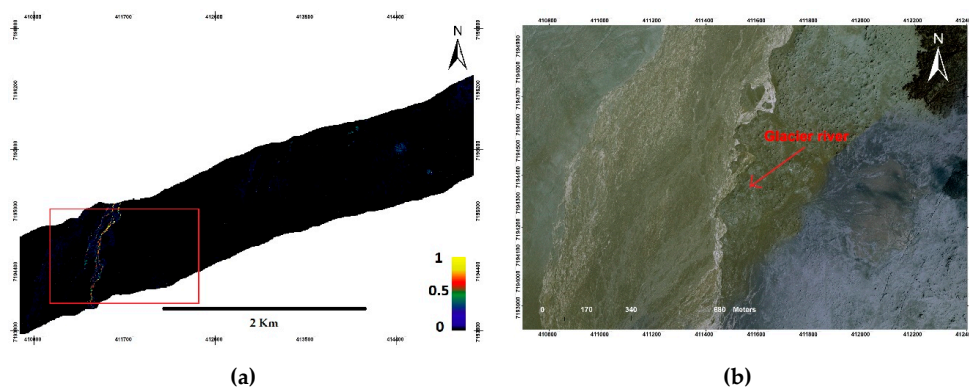


Figure 10. (a) The abundance map for water endmember, the highest abundance fraction indicated by a yellow color, and the lowest abundance fraction indicated by a black red box shows the approximate location of the aerial photograph); (b) aerial photograph of the glacial river.

5.7. Noise Abundance

Figure 11 shows the abundance map corresponding to endmember 9. We consider this endmember as representing noise due to an unrecognized spectral signature since this spectrum is characterized by saturated reflectance in channels ~ 2000 nm and ~ 2400 nm (Figure 5g). The saturated reflectance could be due to corrupted bands in some pixels.

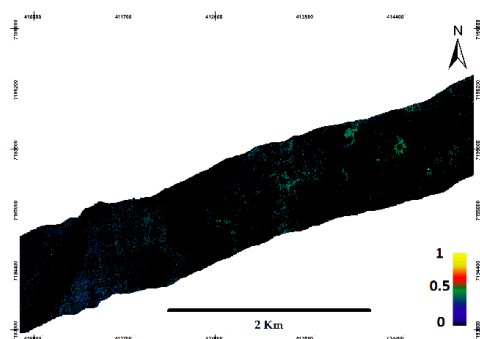


Figure 11. The abundance map for the noise endmember, the highest abundance fraction is indicated by the yellow color, and the lowest abundance fraction is indicated by the black color.

5.8. False Color Abundance

The abundance results depicted as false color (R: Oxidized surface; G: Sulfate mineral; B: Basalt) images show that the majority of rocks or minerals in the study area are dominated by basalt as shown in the blue color in Figure 12a. The other colors such as magenta and yellow indicate a mixture. The mixture phenomenon is illustrated in Figure 12b, as the surface has 0.25 oxidized surface mix with 0.75 basalt resulting in the magenta color; and 0.25 oxidized surface mix with 0.75 sulfate mineral resulting in the yellow color pixel.

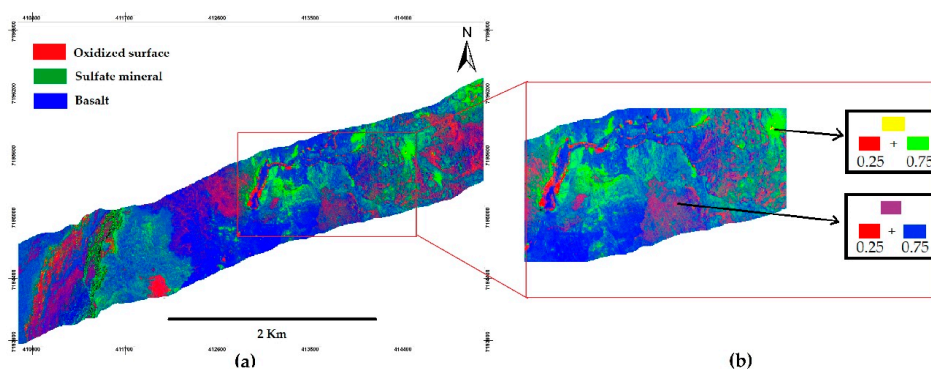


Figure 12. (a) False color of abundance highlighting for R: oxidized surface; G: sulfate mineral; and B: Basalt; (b) Illustration of the mixed pixels in the area, 0.25 oxidized surface mix with 0.75 basalt resulting in the magenta color; and 0.25 oxidized surface mix with 0.75 sulfate mineral resulting in the yellow color pixel.

5.9. Validation

The very high-resolution aerial photograph was used for ground truth. The aerial photograph was classified into oxidized surface, sulfate, basalt, and water using visual image interpretation and used for validation of the unmixing results. We only validate three endmembers for basalt—oxidized, sulfate, and water—since the noise and hot material cannot be detected based on visual interpretation. We classified the endmembers that have fractional abundance > 0.5 . Validation was based on 150 randomly generated point samples within each class. Table 1 show the validation results, with a resulting mean overall accuracy 79% and mean Kappa index of 0.73. This result shows that the abundances have moderate agreement with the sample points.

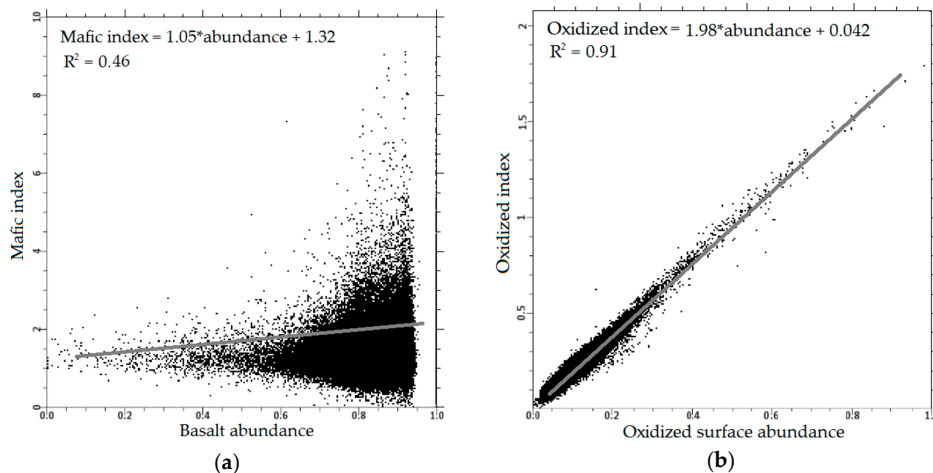
Table 1. Validation of the endmembers that have abundance > 0.5.

Class	Overall Accuracy	Kappa Index	Mean Overall Accuracy	Mean Kappa Index
Basalt/Non-Basalt	70%	0.62		
Sulfate/Non-Sulfate	93%	0.89	79%	0.73
Oxidized/Non-Oxidized	77%	0.72		
Water/Non-Water	76%	0.70		

6. Discussion

6.1. Comparison with the Existing Spectral Index Technique

The correlation between the spectral index images and the abundance image was analyzed. We only correlated the three endmembers since there are no reference spectral indices for sulfate mineral, hot material, and noise. Here we compared the basalt, oxidized, and water abundance images with the mafic, oxidized, and water index images proposed by Inzana et al., Podwysocicki et al. and Xu respectively [42–44] (Appendix B). We applied these indices to the hyperspectral image and compared them with the result from each abundance. Figure 13a–c shows the scatter plots results. The R^2 values were 0.46, 0.91, and 0.77 for the basalt, oxidized surface, and water, respectively. The oxidized surface and water indicate a good correlation with the indices (Figure 13b,c). This suggests that both oxidation and water generated from a spectral index are properly validated [2,44]. Meanwhile, basalt shows a low correlation with the mafic index (Figure 13a) suggesting that the estimates of the basalt surface from the unmixing technique is an overestimation, since the basalt abundance shows the older lava flows as mafic with a relatively high fraction compared to the mafic index that only showed for fresh lava flow. This being due to a full spectrum of hyperspectral can easily differentiate between basalt surface and non-basalt.

**Figure 13.** Cont.

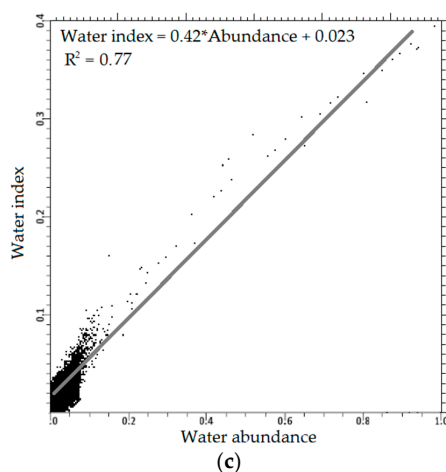


Figure 13. Linear regression analysis between the spectral index images and the (a) basalt abundance; (b) oxidized surface abundance; and (c) water index.

6.2. Number of Endmembers

The determination of the number of endmembers is critical, since underestimation may result in a poor representation of the mixed pixels, whereas overestimation may result in an overly segregated area [16]. Table 2 shows the relationship between the number of endmember and the number of pixels that have fractional abundance > 0.5 and the mean correlation with mafic, oxidized, and water index. We considered abundance > 0.5 as high abundance. As the number of endmembers increase, the number of pixels also increases for an oxidized surface, sulfate mineral, water, and noise abundances, respectively. This is due to an increase of endmembers that is detected for each group. Meanwhile, the basalt abundance shows the opposite, as the endmembers increase the number of pixels with abundance > 0.5 decreases. These results show that as more endmembers are considered the mixing of basalt with other endmembers increases resulting in a decrease of the fractional abundance of basalt. According to the results, we considered the 15 endmembers as an optimum number for this study since they have the highest mean correlation with mafic, oxidized, and water index. Clearly, the selection of appropriate endmembers in such a diverse volcanic environment, considering the particularities of the FENIX dataset, is of great importance in order to obtain accurate unmixing results. In addition, since only a small number of the available materials spectra are expected to be present in a single pixel, the abundance vectors are often sparse [45].

Table 2. Comparison number of pixels that have abundance > 0.5, $\overline{R^2}$ and number of endmembers.

Number of Endmembers	Number of Pixels Abundance						$\overline{R^2}$
	Oxidized Surface	Sulfate Mineral	Hot Material	Water	Noise	Basalt	
5	19	57	19	0	0	522481	0.27
10	86	115	19	0	2	522406	0.35
15	91	215	34	373	2	522266	0.71
20	95	232	36	373	5	522046	0.67
30	97	250	40	373	7	521707	0.69

6.3. Size of Lava Field Area

As the methods were only tested on a subset area of the lava field vent, to apply the methods for the entire lava flow is challenging for several reasons. (1) The high spatial heterogeneity typically gives rise to mixed pixels containing multiple materials and it will increase the number of endmembers detected by SMACC [40]. (2) Different illumination occurs within the different flight lines for the entire

lava flow (Figure 3b) since the data acquisition time is acquired between 16.56 and 17.58 local times which results from the very low sun angle during the acquisition. This problem can be approached by collecting ground truth spectra, extensive calibration, and atmospheric correction using simultaneous and constrained calibration of multiple hyperspectral images through a new generalized empirical line model purposed by Kizel et al. [37]. (3) The computation time to perform unmixing also must be considered for the entire lava field since the area is relatively large (84 km²) and the hyperspectral data contains 622 channels with a 3.5-meter spatial resolution. In order to process the full set of data we need to consider using high performance computing (HPC) [46].

6.4. Using Full Optical Region for Mapping Recent Lava Flow (VIS-SWIR-TIR)

Hyperspectral VIS-SWIR image data is effective for discrimination mafic, oxidation, sulfate etc. However, not all the minerals and surface type are always mapped uniquely with VIS-SWIR hyperspectral data. A typical surface such as rock forming minerals associated with unaltered rocks and alteration minerals associated with altered rocks can be identified with TIR (Thermal Infrared) data [47–49]. Image processing methods that have become standard for hyperspectral VNIR/SWIR data analysis also work for hyperspectral TIR data [47]. Vaughan et al [47] showed that pixel classification techniques based on spectral variability within the scene and mineral libraries for matching spectral emissivity features can be used for TIR-derived mineral maps using SEBASS hyperspectral TIR image data. Hyperspectral TIR instruments operational for airborne surveys are also available in the NERC Airborne Research Facility with a Specim AisaOWL sensor [48]. A synergistic use of airborne data from both FENIX (VIS-SWIR) and OWL (TIR) allows great potential for lava discrimination in future study due to the complementary nature of the reflective (VIS-SWIR) and emissive (TIR) spectral regions. This might significantly improve our understanding of physical lava surface properties. Specifically, VIS-SWIR imaging spectrometers can discriminate surface materials and TIR data acquisitions can help to identify the thermal characteristics of different materials [47–49]. For instance, combining emissivity spectra with reflectance spectra in a mixing model would improve discriminating lava from surfaces [50–52].

7. Conclusions

In this study, an application of potential spectral unmixing methods on 2014–2015 Holuhraun lava flow field was presented. In total, we acquired fifteen spectral endmembers and their abundances. The first endmember was chosen as the brightest pixel which represented saturated incandescent lava. We grouped these 15 endmembers into six groups (basalt, oxidized surface, sulfate mineral, hot material, water, and noise) based on the shape of the endmembers since the amplitude varies due to illumination conditions, spectral variability, and topography. The endmembers represent pure surface materials in a hyperspectral image. We concluded that the selection of appropriate endmembers in such a diverse volcanic environment, considering the particularities of the FENIX dataset, is of great importance in order to obtain accurate unmixing results. Combination of SMACC and LSMA methods offers an optimum and a fast selection for volcanic products segregation. However, ground-truthing spectra are recommended for further analysis. A synergistic use of airborne data from both FENIX (VIS-SWIR) and OWL (TIR) gives a great potential for lava discrimination in future study due to the complementary nature of the reflective (VIS-SWIR) and emissive (TIR) spectral regions. This might significantly improve our understanding of physical lava surface properties.

Author Contributions: Conceptualization, M.A.; Supervision, A.H., M.O.U., I.J. and T.T.

Funding: The first author was supported by the Indonesia Endowment Fund for Education (LPDP) Grant No. 20160222025516, European Network of Observatories and Research Infrastructures for Volcanology (EUROVOLC), The European Facility for Airborne Research (EUFAR) and Vinir Vatnajökuls during his Ph.D. project.

Acknowledgments: Authors would like to thank Robert Askew and Catherine Gallagher from the Institute of Earth Sciences, University of Iceland for the fieldwork photos around the lava field. Authors also would also like to thank anonymous reviewers for their constructive comments for the manuscript.

Conflicts of Interest: The authors declare no conflict of interest.

Appendix A

The bad channels in this data are located at 968 nm and 1014 nm. Figure A1 show the spectral reflectance before masking (Figure A1A) and after channel masking (Figure A1B).

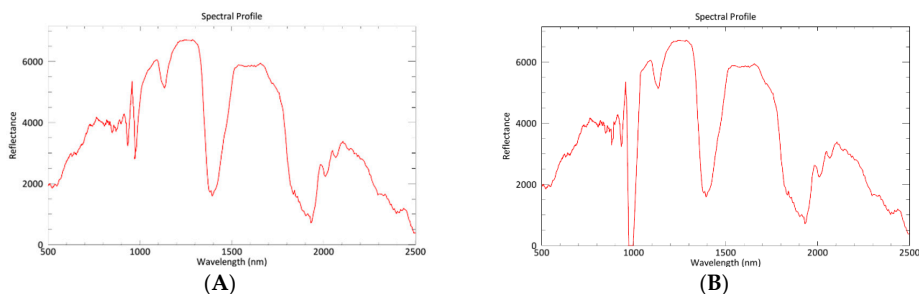


Figure A1. Spectral reflectance of material (A) before masking; (B) after channel masking.

Figure A2. This shows the theoretical pixel size at the nadir for Fenix. The pixel size will be larger at the edges of the swath, in this study, the AGL is ~ 2400 m so according to the graph the optimal pixel size resample for the FENIX is ~3.5 m.

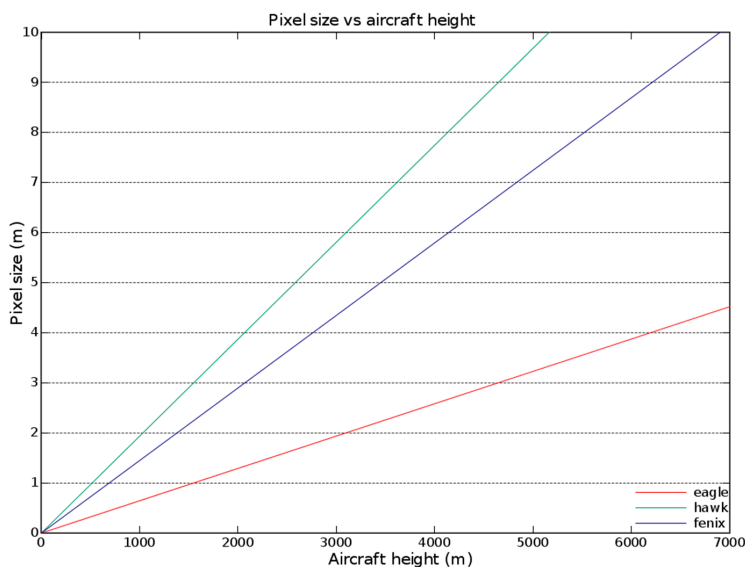


Figure A2. The theoretical pixel size at the nadir for FENIX, EAGLE, and HAWK. In this study we used FENIX airborne for data acquisition [39].

Appendix B

The mafic indices originated, developed by Inzana et al. [42] to distinguish mafic from non-mafic rocks are from Landsat TM image, expressed as follows:

$$\text{Mafic index} = \frac{\rho_{1600\text{nm}}}{\rho_{860\text{nm}}} * \frac{\rho_{640\text{nm}}}{\rho_{860\text{nm}}} \quad (\text{A1})$$

where $\rho_{1600\text{nm}}$ is the measured reflectance at wavelength 1600 nm, $\rho_{640\text{nm}}$ is the measured reflectance at wavelength 640 nm, and $\rho_{860\text{nm}}$ is the measured reflectance at wavelength 860 nm.

The oxidized index originated designed any multispectral sensor with bands that fall within the red channel and blue channel [43], expressed as follows:

$$\text{Oxidized index} = \frac{\rho_{640\text{nm}}}{\rho_{500\text{nm}}} \quad (\text{A2})$$

where $\rho_{500\text{nm}}$ is the measured reflectance at wavelength 500 nm.

We calculated the water index using the Modified Normalized Difference Water Index (MNDWI) [44]. This index enhances open water features while suppressing noise from built-up land, vegetation, and soil. This is expressed as follows:

$$\text{Water index} = \frac{\rho_{600\text{nm}} - \rho_{1600\text{nm}}}{\rho_{600\text{nm}} + \rho_{1600\text{nm}}}$$

where $\rho_{600\text{nm}}$ is the measured reflectance at wavelength 600 nm.

References

- Pedersen, G.B.M.; Höskuldsson, A.; Dürig, T.; Thordarson, T.; Jónsdóttir, I.; Riisshuus, M.S.; Óskarsson, B.V.; Dumont, S.; Magnússon, E.; Gudmundsson, M.T.; et al. Lava field evolution and emplacement dynamics of the 2014–2015 basaltic fissure eruption at Holuhraun, Iceland. *J. Volcanol. Geotherm. Res.* **2017**. [[CrossRef](#)]
- Li, L.; Solana, C.; Canters, F.; Chan, J.; Kervyn, M. Impact of environmental factors on the spectral characteristics of lava surfaces: field spectrometry of basaltic lava flows on Tenerife, Canary Islands, Spain. *Remote Sens.* **2015**, *7*, 16986–17012. [[CrossRef](#)]
- Li, L.; Solana, C.; Canters, F.; Kervyn, M. Testing random forest classification for identifying lava flows and mapping age groups on a single Landsat 8 image. *J. Volcanol. Geotherm. Res.* **2017**, *345*, 109–124. [[CrossRef](#)]
- Head, E.M.; Maclean, A.L.; Carn, S.A. Mapping lava flows from Nyamuragira volcano (1967–2011) with satellite data and automated classification methods. *Geomatics, Nat. Hazards Risk* **2013**, *4*, 119–144. [[CrossRef](#)]
- Li, L.; Canters, F.; Solana, C.; Ma, W.; Chen, L.; Kervyn, M. Discriminating lava flows of different age within Nyamuragira's volcanic field using spectral mixture analysis. *Int. J. Appl. Earth Obs. Geoinf.* **2015**, *40*, 1–10. [[CrossRef](#)]
- Amici, S.; Piscini, A.; Neri, M. Reflectance Spectra Measurements of Mt. Etna: A Comparison with Multispectral / Hyperspectral Satellite. *Adv. Remote Sens.* **2014**, *3*, 235–245. [[CrossRef](#)]
- Graettinger, A.H.; Ellis, M.K.; Skilling, I.P.; Reath, K.; Ramsey, M.S.; Lee, R.J.; Hughes, C.G.; McGarvie, D.W. Remote sensing and geologic mapping of glaciovolcanic deposits in the region surrounding Askja (Dyngjufjöll) volcano, Iceland. *Int. J. Remote Sens.* **2013**, *34*, 7178–7198. [[CrossRef](#)]
- Zhang, X.; Shang, K.; Cen, Y.; Shuai, T.; Sun, Y. Estimating ecological indicators of karst rocky desertification by linear spectral unmixing method. *Int. J. Appl. Earth Obs. Geoinf.* **2014**, *31*, 86–94. [[CrossRef](#)]
- Combe, J.P.; Le Mouélic, S.; Sotin, C.; Gendrin, A.; Mustard, J.F.; Le Deit, L.; Launeau, P.; Bibring, J.P.; Gondet, B.; Langevin, Y.; et al. Analysis of OMEGA/Mars Express data hyperspectral data using a Multiple-Endmember Linear Spectral Unmixing Model (MELSUM): Methodology and first results. *Planet. Space Sci.* **2008**, *56*, 951–975. [[CrossRef](#)]
- Adams, J.B.; Smith, M.O.; Johnson, P.E. Spectral mixture modeling: A new analysis of rock and soil types at the Viking Lander 1 Site. *J. Geophys. Res.* **1986**. [[CrossRef](#)]
- Kruse, F.A.; Perry, S.L. Mineral mapping using simulated worldview-3 short-wave-infrared imagery. *Remote Sens.* **2013**, *6*, 2688–2703. [[CrossRef](#)]
- Sun, Y.; Tian, S.; Di, B. Extracting mineral alteration information using WorldView-3 data. *Geosci. Front.* **2017**. [[CrossRef](#)]
- Aufaristama, M.; Höskuldsson, Á.; Jónsdóttir, I.; Ólafsdóttir, R. Mapping and Assessing Surface Morphology of Holocene Lava Field in Krafla (NE Iceland) Using Hyperspectral Remote Sensing. *IOP Conf. Ser. Earth Environ. Sci.* **2016**, *29*, 1–6. [[CrossRef](#)]
- Spinetti, C.; Mazzarini, F.; Casacchia, R.; Colini, L.; Neri, M.; Behncke, B.; Salvatori, R.; Buongiorno, M.F.; Pareschi, M.T. Spectral properties of volcanic materials from hyperspectral field and satellite data compared with LiDAR data at Mt. Etna. *Int. J. Appl. Earth Obs. Geoinf.* **2009**, *11*, 142–155. [[CrossRef](#)]

15. Kolzenburg, S.; Jaenicke, J.; Münzer, U.; Dingwell, D.B. The effect of inflation on the morphology-derived rheological parameters of lava flows and its implications for interpreting remote sensing data - A case study on the 2014/2015 eruption at Holuhraun, Iceland. *J. Volcanol. Geotherm. Res.* **2018**, *357*, 200–212. [[CrossRef](#)]
16. Daskalopoulou, V.; Sykioti, O.; Karagiannopoulou, C. Application of Spectral Unmixing on Hyperspectral data of the Historic volcanic products of Mt. Etna (Italy). *Multidiscip. Digit. Publ. Inst. Proc.* **2018**, *2*, 329. [[CrossRef](#)]
17. Coppola, D.; Ripepe, M.; Laiolo, M.; Cigolini, C. Modelling satellite-derived magma discharge to explain caldera collapse. *Geology* **2017**, *45*, 523–526. [[CrossRef](#)]
18. Aufaristama, M.; Hoskuldsson, A.; Jonsdottir, I.; Ulfarsson, M.; Thordarson, T. New Insights for Detecting and Deriving Thermal Properties of Lava Flow Using Infrared Satellite during 2014–2015 Effusive Eruption at Holuhraun, Iceland. *Remote Sens.* **2018**, *10*, 151. [[CrossRef](#)]
19. Rossi, C.; Minet, C.; Fritz, T.; Eineder, M.; Bamler, R. Temporal monitoring of subglacial volcanoes with TanDEM-X - Application to the 2014–2015 eruption within the Bardarbunga volcanic system, Iceland. *Remote Sens. Environ.* **2016**, *181*, 186–197. [[CrossRef](#)]
20. Dirscherl, M.; Rossi, C. Geomorphometric analysis of the 2014–2015 Bárðarbunga volcanic eruption, Iceland. *Remote Sens. Environ.* **2018**. [[CrossRef](#)]
21. Adams, J.B.; Sabol, D.E.; Kapos, V.; Almeida Filho, R.; Roberts, D.A.; Smith, M.O.; Gillespie, A.R. Classification of multispectral images based on fractions of endmembers: Application to land-cover change in the Brazilian Amazon. *Remote Sens. Environ.* **1995**. [[CrossRef](#)]
22. Quintano, C.; Fernández-Manso, A.; Shimabukuro, Y.E.; Pereira, G. Spectral unmixing. *Int. J. Remote Sens.* **2012**. [[CrossRef](#)]
23. Kolzenburg, S.; Giordano, D.; Thordarson, T.; Höskuldsson, A.; Dingwell, D.B. The rheological evolution of the 2014/2015 eruption at Holuhraun, central Iceland. *Bull. Volcanol.* **2017**, *79*, 45. [[CrossRef](#)]
24. Icelandic Meteorological Office Holuhraun. Available online: <http://en.vedur.is/earthquakes-and-volcanism/articles/nr/3122> (accessed on 11 May 2017).
25. Tayebi, M.H.; Tangestani, M.H.; Vincent, R.K.; Neal, D. Spectral properties and ASTER-based alteration mapping of Masahim volcano facies, SE Iran. *J. Volcanol. Geotherm. Res.* **2014**, *287*, 40–50. [[CrossRef](#)]
26. Clark, R.N.; Roush, T.L. Reflectance spectroscopy: quantitative analysis techniques for remote sensing applications. *J. Geophys. Res.* **1984**. [[CrossRef](#)]
27. Zhang, J.; Rivard, B.; Sánchez-Azofeifa, A. Spectral unmixing of normalized reflectance data for the deconvolution of lichen and rock mixtures. *Remote Sens. Environ.* **2005**. [[CrossRef](#)]
28. Zhang, J.; Rivard, B.; Sanchez-Azofeifa, A. Derivative spectral unmixing of hyperspectral data applied to mixtures of lichen and rock. *IEEE Trans. Geosci. Remote Sens.* **2004**.
29. Rowan, L.C.; Mars, J.C.; Simpson, C.J. Lithologic mapping of the Mordor, NT, Australia ultramafic complex by using the Advanced Spaceborne Thermal Emission and Reflection Radiometer (ASTER). *Remote Sens. Environ.* **2005**. [[CrossRef](#)]
30. Hellman, M.J.; Ramsey, M.S. Analysis of hot springs and associated deposits in Yellowstone National Park using ASTER and AVIRIS remote sensing. *J. Volcanol. Geotherm. Res.* **2004**. [[CrossRef](#)]
31. Hyperspectral Imaging Cameras And Systems - Specim. Available online: <http://www.specim.fi/> (accessed on 1 December 2018).
32. NERC Airborne Research Facility - British Antarctic Survey. Available online: <https://www.bas.ac.uk/polar-operations/sites-and-facilities/facility/nerc-airborne-research-facility-2/> (accessed on 3 December 2018).
33. Loftmyndir ehf. Available online: <http://www.loftmyndir.is/> (accessed on 12 February 2019).
34. Bernstein, L.S.; Adler-Golden, S.M.; Sundberg, R.L.; Levine, R.Y.; Perkins, T.C.; Berk, A.; Ratkowski, A.J.; Felde, G.; Hoke, M.L. A new method for atmospheric correction and aerosol optical property retrieval for VIS-SWIR multi- and hyperspectral imaging sensors: QUAC (QUick Atmospheric Correction). *IGRSS* **2005**, *5*. [[CrossRef](#)]
35. Bernstein, L.S. Quick atmospheric correction code: algorithm description and recent upgrades. *Opt. Eng.* **2012**, *51*, 111719. [[CrossRef](#)]
36. Karpouzli, E.; Malthus, T. The empirical line method for the atmospheric correction of IKONOS imagery. *Int. J. Remote Sens.* **2003**. [[CrossRef](#)]

37. Kizel, F.; Benediktsson, J.A.; Bruzzone, L.; Pedersen, G.B.M.; Vilmundardottir, O.K.; Falco, N. Simultaneous and constrained calibration of multiple hyperspectral images through a new generalized empirical line model. *IEEE J. Sel. Top. Appl. Earth Obs. Remote Sens.* **2018**. [CrossRef]
38. Warren, M.A.; Taylor, B.H.; Grant, M.G.; Shutler, J.D. Data processing of remotely sensed airborne hyperspectral data using the Airborne Processing Library (APL): Geocorrection algorithm descriptions and spatial accuracy assessment. *Comput. Geosci.* **2014**, *64*, 24–34. [CrossRef]
39. Processing/PixelSize. Available online: <https://nerc-arf-dan.pml.ac.uk/trac/wiki/Processing/PixelSize> (accessed on 31 December 2018).
40. Gruninger, J.H.; Ratkowski, A.J.; Hoke, M.L. The sequential maximum angle convex cone (SMACC) endmember model. *SPIE* **2004**, *5425*, 1.
41. Moore, R.B.; Clague, D.A.; Rubin, M.; Bohrsen, W.A. Volcanism in Hawaii. In *U.S. Geological Survey Professional Paper 1350*; USGS: Reston, VA, USA, 1987; p. 557. ISBN 3663537137.
42. Inzana, J.; Kusky, T.; Higgs, G.; Tucker, R. Supervised classifications of Landsat TM band ratio images and Landsat TM band ratio image with radar for geological interpretations of central Madagascar. *J. African Earth Sci.* **2003**, *37*, 59–72. [CrossRef]
43. Podwysocki, M.H.; Segal, D.B.; Abrams, M.J. Use of multispectral scanner images for assessment of hydrothermal alteration in the Marysvale, Utah, mining area. *Econ. Geol.* **1983**. [CrossRef]
44. Xu, H. Modification of normalised difference water index (NDWI) to enhance open water features in remotely sensed imagery. *Int. J. Remote Sens.* **2006**. [CrossRef]
45. Giampouras, P.V.; Themelis, K.E.; Rontogiannis, A.A.; Koutroumbas, K.D. Simultaneously Sparse and Low-Rank Abundance Matrix Estimation for Hyperspectral Image Unmixing. *IEEE Trans. Geosci. Remote Sens.* **2016**. [CrossRef]
46. Plaza, A.; Du, Q.; Chang, Y.; King, R.L. High Performance Computing for Hyperspectral Remote Sensing. *IEEE J. Sel. Top. Appl. Earth Obs. Remote Sens.* **2011**, *4*, 528–544. [CrossRef]
47. Vaughan, R.G.; Calvin, W.M.; Taranik, J.V. SEBASS hyperspectral thermal infrared data: Surface emissivity measurement and mineral mapping. *Remote Sens. Environ.* **2003**, *85*, 48–63. [CrossRef]
48. Schlerf, M.; Rock, G.; Lagueux, P.; Ronellenfitsch, F.; Gerhards, M.; Hoffmann, L.; Udelhoven, T. A hyperspectral thermal infrared imaging instrument for natural resources applications. *Remote Sens.* **2012**, *4*, 3995–4009. [CrossRef]
49. Riley, D.; Hecker, C. Mineral Mapping with Airborne Hyperspectral Thermal Infrared Remote Sensing at Cuprite, Nevada, USA. In *Thermal Infrared Remote Sensing: Sensors, Methods, Applications*; Kuenzer, C., Dech, S., Eds.; Springer: Heidelberg, The Netherlands, 2013; Vol. 17, pp. 495–514. ISBN 978-94-007-6639-6.
50. Ball, M.; Pinkerton, H.; Harris, A.J.L. Surface cooling, advection and the development of different surface textures on active lavas on Kilauea, Hawai'i. *J. Volcanol. Geotherm. Res.* **2008**, *173*, 148–156. [CrossRef]
51. Ramsey, M.S.; Harris, A.J.L.; Crown, D.A. What can thermal infrared remote sensing of terrestrial volcanoes tell us about processes past and present on Mars? *J. Volcanol. Geotherm. Res.* **2016**, *311*, 198–216. [CrossRef]
52. Harris, A. *Thermal Remote Sensing of Active Volcanoes: A User's Manual*; Cambridge University Press: Cambridge, UK, 2013; ISBN 9781139029346.



**Paper III: Lava Flow Roughness on
the 2014–2015 Lava Flow-Field at
Holuhraun, Iceland, Derived from
Airborne LiDAR and Photogrammetry**

Article

Lava Flow Roughness on the 2014–2015 Lava Flow-Field at Holuhraun, Iceland, Derived from Airborne LiDAR and Photogrammetry

Muhammad Aumaristama ^{1,2,*} , Ármann Höskuldsson ¹ , Magnus Orn Ulfarsson ³ ,
Ingibjörg Jónsdóttir ^{1,2} and Thorvaldur Thordarson ^{1,2}

¹ Institute of Earth Sciences, University of Iceland, Sturlugata 7, 101 Reykjavík, Iceland; armh@hi.is (Á.H.); ij@hi.is (I.J.); torvth@hi.is (T.T.)

² Faculty of Earth Sciences, University of Iceland, Sturlugata 7, 101 Reykjavík, Iceland

³ Faculty of Electrical and Computer Engineering, University of Iceland, Hjardarhagi 2-7, 107 Reykjavík, Iceland; mou@hi.is

* Correspondence: mua2@hi.is

Received: 24 February 2020; Accepted: 27 March 2020; Published: 31 March 2020



Abstract: Roughness can be used to characterize the morphologies of a lava flow. It can be used to identify lava flow features, provide insight into eruption conditions, and link roughness pattern across a lava flow to emplacement conditions. In this study, we use both the topographic position index (TPI) and the one-dimensional Hurst exponent (H) to derive lava flow unit roughness on the 2014–2015 lava field at Holuhraun using both airborne LiDAR and photogrammetric datasets. The roughness assessment was acquired from four lava flow features: (1) spiny lava, (2) lava pond, (3) blocky surface, and (4) inflated channel. The TPI patterns on spiny lava and inflated channels show that the intermediate TPI values correspond to a small surficial slope indicating a flat and smooth surface. Lava pond is characterized by low to high TPI values and forms a wave-like pattern. Meanwhile, irregular transitions patterns from low to high TPI values indicate a rough surface that is found in blocky surface and flow margins. The surface roughness of these lava features falls within the H range of 0.30 ± 0.05 to 0.76 ± 0.04 . The roughest surface is the blocky, and inflated lava flows appear to be the smoothest surface among these four lava units. In general, the Hurst exponent values in the 2014–2015 lava field at Holuhraun has a strong tendency in 0.5, both TPI and Hurst exponent successfully derive quantitative flow roughness.

Keywords: lava roughness; TPI; Hurst exponent; LiDAR; photogrammetry

1. Introduction

In the Earth Sciences, surface roughness is important for modeling natural phenomena and classifying features of interest [1,2]. Surface roughness refers to a topographic expression of surface profiles over various scales (i.e., centimeters, meters, kilometers) [1–3]. Quantitative approaches to estimate the roughness of natural materials are increasingly sought in modern geological research [1]. Statistical descriptors of surface morphology, or roughness, are found in many applications, including volcanology, especially for analyzing lava flows. Field observations have long been used in the study of surface roughness of lava flow [2–6]. These analyses are mostly based on in situ measurements, which require extended time in the field [2,6–8]. In practice, a grid is laid out on the sample surface, and heights are measured manually or with a profiling instrument [2–4] and continuous Global Positioning System (GPS) [7]. Lava roughness reflects the morphology of lava flow, and some flows can be distinguished by roughness [2,7,9]. Thus, roughness can be used to identify lava flow features that reflect eruption conditions. Patterns of roughness across the lava flow can be tied to emplacement

conditions such as rate of flow and viscosity [2,3,10–12]. Roughness is typically determined from topography [2,3,13] or radar backscattering [4,14,15] (e.g., root mean square (RMS) height, correlation length, and autocorrelation function). Generally, the quantification of surface roughness is derived from analyzing height variations along profiles.

In the past 25 years, the study of lava flows roughness has embraced the use of remote sensing for acquiring surface geometry [11,16,17]. Airborne light detection and ranging (LiDAR) scanning and photogrammetry offers rapid three-dimensional (3D) data capture and have made datasets increasingly available to scientists [1]. Similar measurement techniques have been used to obtain ground-based measurements of surface roughness [7,16]. High-resolution topographic methods such as airborne LiDAR and photogrammetry generated DEMs (Digital Elevation Models) with meter scale resolution [8,18] allow for detailed roughness assessment. In this study, we evaluated two approaches to assess lava surface roughness based on LiDAR and photogrammetry datasets using: (1) the Topographic Position Index (TPI) [11,19]; and (2) the Hurst exponent (H) [2,7,8,16] on the most recent effusive eruption in Iceland, the 2014–2015 lava field at Holuhraun. We envisage future applications to assess geomorphic variation amongst different lava flows on Earth and other planets for which DEMs of high resolution and large areal extent are available.

2. The Surface Roughness of Lava Flows

Measurements of a lava flow surface roughness on Earth are used to describe changes in eruption conditions across a flow [20–22], surface processes that have occurred post-emplacement [2], to map flow units [3,8] and the relation between lava roughness and composition [2,9,23]. Effusive eruptions of basaltic magmas generally produce lava flows due to high magma temperatures and low viscosity. As lava starts to flow and cool, its surface may fold or break into blocks if the surface is steeply sloping due to the flow front stagnating from cooling [9,24]. This influences centimeter to decameter-scale roughness. If the emplacement surface is flat, the flow will advance slowly and take longer to cool, producing a smooth crust while intact, and a rougher surface if the crust breaks into blocks [9,11].

According to Kilburn [25], most basaltic lavas can be grouped according to surface roughness; (1) pahoehoe, where the surface is smooth and continuous (Figure 1a), (2) aa, where the surface is rough and fragmented (Figure 1b), and (3) blocky, where the surface is brecciated (Figure 1c). Furthermore, a transition surface morphology between aa and pahoehoe has been described as platty, slabby, and rubbly [26]. Thus, assessing lava flow textures can provide insight into the lava flow dynamics. Lower viscosities or shear strain results in smooth textures; rough textures are generally the result of higher viscosities, higher shear strain, or disruption of the cooled surface [2,3,7]. Identification of lava flow textures can further explain the geologic history of the eruption by confirming the styles, timing, and geographic extent of volcanic activity that occurred [27].

Volcanic eruptions can be understood through the variations in lava flow roughness at different scales. Spiny pahoehoe (Figure 1a) are typically smooth at meter scale and with spinose preserved on the surface of a pahoehoe flow and characterized by longitudinal grooves and ridges [28]. Ropy folds (Figure 1d) also provide an example of relating roughness to emplacement conditions [29,30]. Field observations of solidified pahoehoe surfaces and motion pictures of active flows suggest that these features may be interpreted as folds that develop in response to the shortening of the flow surface [30]. These features also indicate slowly moving low viscosity pahoehoe flows in basaltic eruptions [20,23,27,30–32]. Though these features may appear flat and devoid of height changes at the meter and decameter scale, the texture is quite rough when observed at the centimeter scale. Spiny and ropy folds are both different from aa lava flows, which are composed of piles of jagged blocks and are rough at centimeter to decameter scale [2,3]. Table 1 shows lava surface features and the scales at which they are observed.

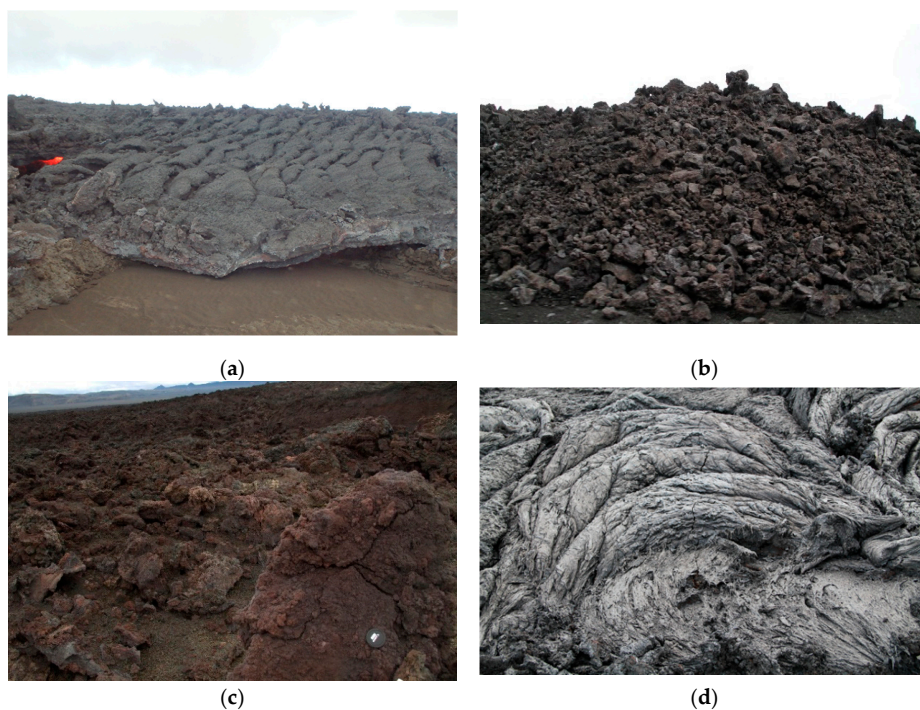


Figure 1. Surface morphology on the 2014–2015 lava flow at Holuhraun. (a) Spiny pahoehoe flow on Holuhraun lava flow with a smooth, coherent crust at the meter scale (Photo was taken by Thorvaldur Thordarson). (b) Aa lava flow with brecciated flow tops and bases (Photo was taken by G.B.M. Pedersen). (c) A blocky surface that is composed of larger blocks than aa lava and these blocks have a larger surface area (Photo was taken by Muhammad AUFARISTAMA). (d) Ropy folds observed in the channel flow and pond (Photo was taken by G.B.M. Pedersen).

Table 1. Features Affecting Lava Flow Roughness at Different Scales, modified from James [11].

Scale	Flow Features	Common Methods	Resolution	References
Millimeter to centimeter	Gas bubble walls and minor folds/cracks	Microscope, Radar backscattering	<1 cm	[33,34]
Centimeter to meter	Flow toes and blocks	Hurst exponent, RMS slope	<1 m	[2,7,11,33]
Meter	Tumuli, ridges, and crease patterns	Radar backscatter, Hurst exponent	~1 m	[7,11,16,31]
More than decameter	Full flow fields, flow margin	Radar polarization	>10 m	[3,4,15]

A variety of methods are used to quantify surface roughness of lava surfaces [2,3,35]. Two commonly used methods are the RMS of height and the H [2,7,16]. RMS represents the standard deviation of the height slope around the mean height [2]. RMS is a valuable method for vertical roughness, but it does not account for the horizontal patterns [11,36]. It has been used to study the roughness of lunar impact melts, and Martian lava flows [7]. To accurately reflect lava surface roughness, elevations in 360 degrees around a point should be considered, rather than only measuring topographic changes along one horizontal direction [11]. Therefore, we use TPI, and the one-dimensional H for determining the roughness of the 2014–2015 Holuhraun lava flows

from both LiDAR DEM and photogrammetry DEM. The detailed methodology for these techniques will be explained in Section 4.2.

3. Morphology of the 2014–2015 Lava Flow at Holuhraun

The six months long eruption at Holuhraun 2014–2015 was the largest effusive eruption in Iceland in 230 years with an estimated bulk lava volume of 1.44 km³ [37–39]. The eruption is split into three phases based on the lava flow-field evolution [37]. The first phase was dominated by open channels, and during the second phase, lava emplacement was affected by the formation of a 1 km² lava pond about 1 km downstream of the vent [37]. This pond became the main distribution point for the lava during this phase, controlling the emplacement of lava flows. Near the end of the second phase, vertical stacking of lava lobes became more prevalent, and lava tubes developed within the channel system, resulting in the formation of inflation plateaus [37]. In the final phase, transport of lava through tubes continued, and inflation plateaus grew in extent, raising the original channel surface by 5–10 m above the surrounding lava. Over 19 km² of the flow field was resurfaced via surface breakouts from the closed paths during this period. Pedersen et al. [37] suggest that the topography of the lava field and surrounding made it possible to build an open channel system that was at minimum 5–10 m higher than the fluid lava. This system increased the static lava pressure, which was enough to lift the roof of the lava channels creating the inflation plateaus, allowing new lava to be transported to the distal ends of the lava field.

During the three phases of the 2014–2015 eruption, major changes in surface morphology of the lava occurred several times [37,40]. According to Pedersen et al. [37], shelly pahoehoe, slabby pahoehoe, rubbly pahoehoe, spiny pahoehoe, and aa were observed within the first week of the eruption. During the first phase and the second phase, aa was the dominant flow morphology of lava flows, and in the final phase, spiny pahoehoe was the main lava morphology [37]. This change from aa and pahoehoe morphology in the first and second phases to spiny pahoehoe in the final phase makes Holuhraun a paired lava flow-field. A paired lava flow-field is formed due to the decline of the effusion rate over the course of an eruption [41]. The Holuhraun lava flow-field was emplaced on a low-slope floodplain, and the chemical composition of the lava was uniform throughout the whole eruption [42,43]. This suggests that neither the topography nor the lava composition was the main factor for the observed changes in flow morphology [37]. The first transition of slabby pahoehoe to rubbly pahoehoe to aa occurred downstream of the vent, which is consistent with such changes in other lava producing eruptions and is explained by increased viscosity due to mixing, cooling, and gas loss during lava transport [34,37].

In this study, we examined roughness over lava flow surfaces in four locations depicted in Figure 2 that exhibit the known lava flow morphology at Holuhraun [7,37,44]. These lava flow features are: (1) lava pond, (2) spiny pahoehoe, (3) inflated channel, and (4) blocky surface. The lava pond formed during the first phase of the eruption [37]. Ropy folds preserved on the surface of a lava pond (Figure 1d) indicate slowly moving, low viscosity pahoehoe flows, which develop in response to the shortening of the flow surface in basaltic eruptions [30]. At the Holuhraun lava flow-field, spiny lava is characterized by a network of interconnected lobes that form inflated sheet-like flow units with rough spinose surfaces [7]. The millimeter-scale spines on the surface of these flows resemble the texture of aa, but the flow surfaces are generally continuous and are not decomposed into clinker [7]. Spiny lava units are the dominant flow type along most of the flow margins, except near the NE margin of the flow [7]. The inflated channel formed towards the end of the second phase to the final phase [37]. This surface feature maintains the morphology of the flow channel but increases in thickness. Pahoehoe flows are typically identified as inflated lava flows, but aa type flows may also inflate under certain circumstances [45]. In this study, we use the term blocky surface to avoid confusion with rubbly lava. Blocky surface is composed of larger blocks than rubbly. Similar to rubbly lava this feature likely formed due to continued auto-brecciation of crustal slabs into blocks of material through mechanical collisions between the slabs during transport [26]. At Holuhraun lava flow-field,

blocky surfaces are mostly found close to the vent. These lava flows were analyzed using the approach described in Section 4, and the results for the roughness analysis are presented in Section 5.

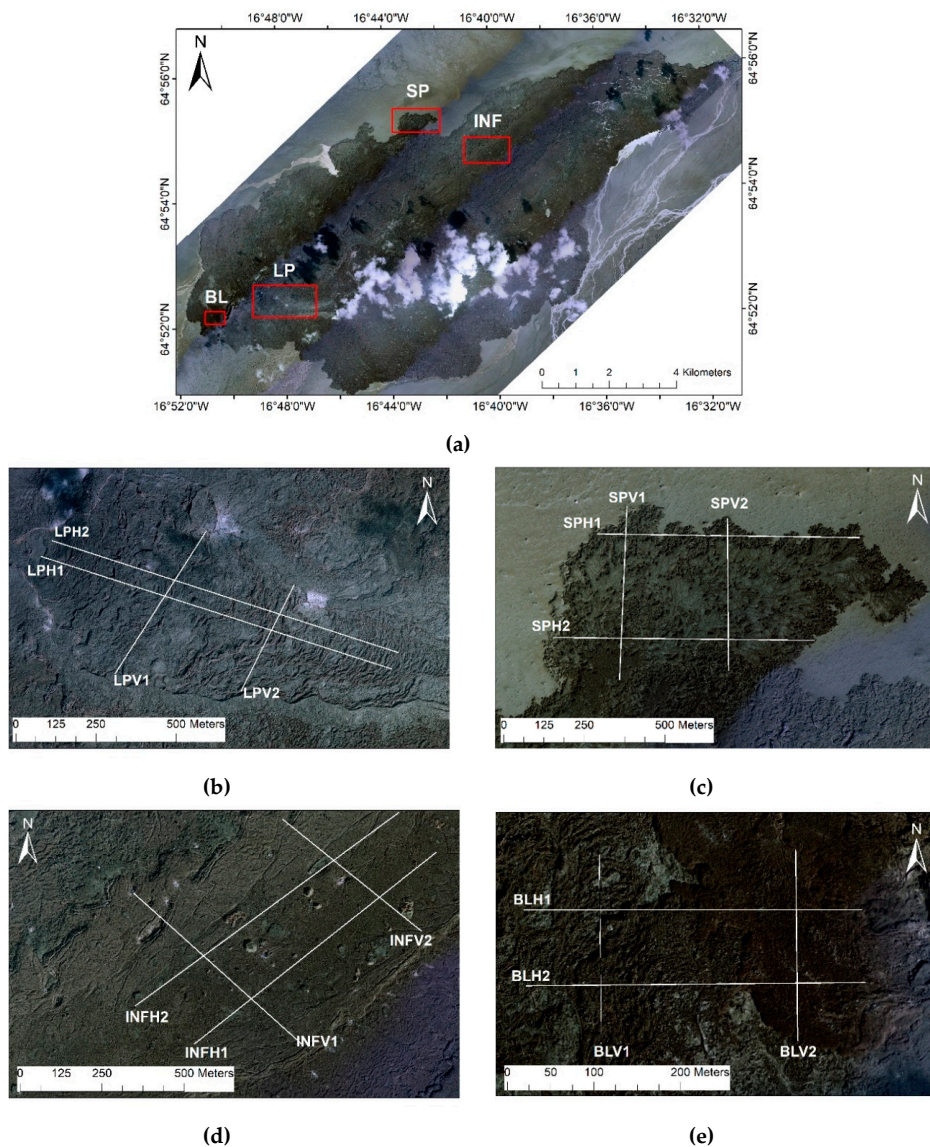


Figure 2. An aerial photograph of the Holuhraun lava field (a) taken by Loftmyndir ehf with four different facies units (red boxes): (b) Lava pond (LP); (c) spinnny pahoehoe (SP); (d) inflated channel (INF); and (e) blocky surface (BL). The white profiles are profiles used to derive the Hurst exponent. The horizontal and vertical profiles are collected for each unit marked with H1, H2, V1, and V2.

4. Datasets and Methods

To assess the surface roughness of lava flow features, we use high-DEM from two different sources. We focus on a subset of these data, obtained at four different facies on the lava flow-field. The datasets used in this study are described further in Table 2 and Section 4.1

Table 2. High-resolution DEM used in this study.

Platform	Date of Acquisition	Area	Spatial Resolution	Source
Airborne LiDAR	4 September 2015	100 km ² (Gap in between lines)	1 m (processed in ENVI LiDAR 5.3)	NERC
Airborne photogrammetry	30 August 2015	167 km ²	5 m	Loftmyndir ehf

4.1. Airborne LiDAR and Photogrammetry

Airborne LiDAR data, collected and processed by the Natural Environment Research Council (NERC) was acquired on September 4, 2015. We processed the point clouds to obtain 1 m spatial resolution over the lava flow-field with a vertical resolution of 4–5 cm (depending on the flight line). This was done using ENVI LiDAR 5.3 software. Eight flight lines were flown over Holuhraun: seven of these are parallel and aligned with the long axis of the field, while the eighth is transverse and crosses all the others (Figure 3a). The LiDAR measurements, therefore, do not cover the entirety of the flow-field. Furthermore, small clouds and fumaroles obscured parts of the lava and created gaps in the data. We sought to determine the surface roughness of the 2014–2015 lava flows at Holuhraun. DEMs are produced upon processing of point-clouds for a variety of lava flow textures around the study area.

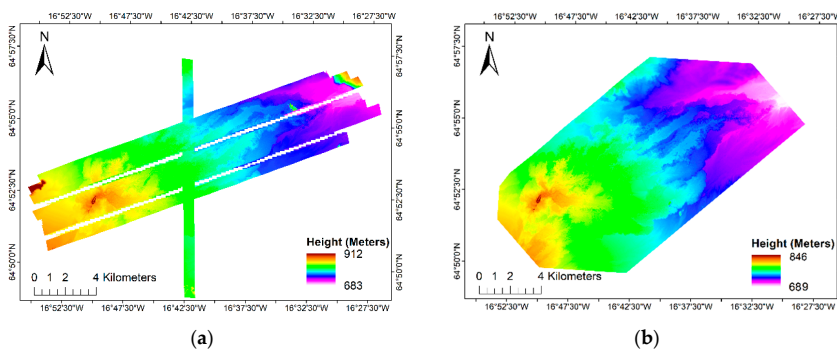


Figure 3. (a) The LiDAR DEM acquired on 4 September 2015, with a 1-meter pixel resolution. The LiDAR does not cover the entirety of the flow-field and has a gap in between the eight lines. (b) Photogrammetry-derived DEM based on an aerial photograph with a spatial resolution of 5 m.

We used photogrammetry-derived DEM provided by Loftmyndir ehf using data taken on August 30, 2015. Clouds obscured in some parts of the 2014–2015 Holuhraun lava flow-field (Figure 2). This Photogrammetry-derived DEM has a spatial resolution of 5 m (Figure 3b).

4.2. Deriving Surface Roughness

The methodology adopted for the assessment of the roughness is given in a sequential manner in Figure 4. In this study, we use TPI and one-dimensional H to quantify roughness values in the 2014–2015 Holuhraun lava flows from both photogrammetry DEM and LiDAR DEM. Finally, we determined the roughness properties for four different facies on the lava flow-field from Figure 2.

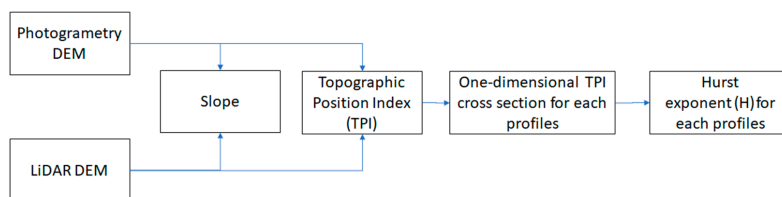


Figure 4. The workflow processing to assess roughness from the lava flow from LiDAR and photogrammetry.

4.2.1. Slope

The estimation of slope from a regularly gridded DEM is a common procedure in terrain analysis [46,47]. The slope can be defined as a function of the gradients in the x and y direction at every point in a DEM:

$$slope = \arctan \sqrt{f_x^2 + f_y^2}. \tag{1}$$

The key in the slope estimation is the computation of the perpendicular gradients f_x and f_y . We used moving 3×3 windows to derive local polynomial surface fit for the calculation [46,47]. This process was done using ArcGIS 10.6.

4.2.2. Topographic Position Index

In this study, topographic position index (TPI) [48] was used for deriving the roughness pattern of the lava flow-field. This method was originally created for use in ecology, geomorphology, and hydrology study [19,48] but has been recently used for assessing the topographic characteristics of lava flows [11]. TPI compares the elevation of each cell in a DEM to the mean elevation of a specified neighborhood around that cell. Mean elevation is subtracted from the elevation value at the center

$$TPI = \frac{C_0 - \bar{C}}{\sigma}, \tag{2}$$

where C_0 is the elevation of the model point under evaluation, \bar{C} is the mean elevation of a gridpoint in the neighborhood, σ is the standard deviation of elevation in the neighborhood. Positive TPI indicates that a cell is higher in elevation (or more steeply sloping) than the average of its neighbors up to a specified distance away, whereas a negative one indicates that a cell is lower than the average of surrounding elevations (Figure 5) [19]. The cell neighborhood can be adapted to produce varying TPI values for different scales, thus changing the scale of roughness could affect the results [11,19,48]. In this study, we use a rectangular TPI with a 3×3 neighborhood size for both LiDAR DEM and photogrammetry DEM.

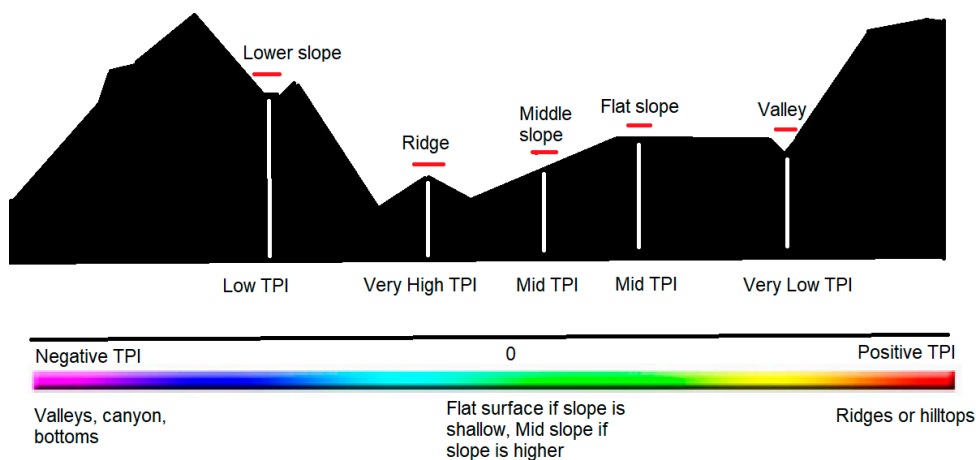


Figure 5. An illustration of the topographic position index (TPI) value in the topography, adapted, and modified from Jenness [19]. The red lines indicate the neighborhood size.

4.2.3. Hurst Exponent

In this study, we acquired a one-dimensional TPI profile over various lava flow surfaces in four locations in Figure 2. The profiles were typically a few hundred meters to kilometers long. Roughness

properties may have directional biases [2,7,8]. In this study, profiles were collected in perpendicular directions (Figure 2). The Hurst exponent (H) is derived using rescaled range analysis (R/S) [15,49] for the TPI profiles. Equation (3) below shows the relation between R/S and H as

$$H = \frac{\log\left(\frac{R}{S}\right)}{\log(\tau)}, \quad (3)$$

where R is the difference between the maximum and minimum TPI detected in profiles, S is the standard deviation, and τ is the transect profiles. Hurst coefficient ranges from 0 to 1, where a higher H means a smooth or equally rough surface [2]. The mean Hurst exponent (\bar{H}) was calculated for each lava unit.

5. Results

We extracted the slope, TPI, and Hurst exponent from the lava flow features in Figure 2 (lava pond, spiny pahoehoe, inflated channel, and blocky surface). Each lava feature displays TPI and H variations, although the entire range of H variation is not displayed at any individual flow. The roughness analysis results are shown as maps and profiles for each lava flow features. Based on the analysis, the surface feature that corresponds to a higher H and intermediate TPI pattern reflects a smoother surface than the lower H and irregular TPI patterns.

5.1. Lava Pond Roughness

For the photogrammetry DEM (Figure 6a), TPI and slope values at the lava pond ranged from -2.8 m to 2.8 m and from 0.4° to 12.5° (Figure 6b,c), respectively. For the LiDAR DEM (Figure 6d), TPI and slope values ranged from -3.2 m to 5.4 m and from 0.5° to 30° (Figure 6e,f), respectively. Both the LiDAR and photogrammetry derived TPI images have wave-like transitions patterns (Figure 6c,f). These patterns are also apparent from the slope (Figure 6b,e), indicating a relatively rough surface due to the ropy fold on the lava pond. Folds where the velocity and viscosity of the lava surface decreases rapidly with depth [30]. This causes surface folding and irregular waviness in the surface which preserve on wave-like pattern on TPI maps.

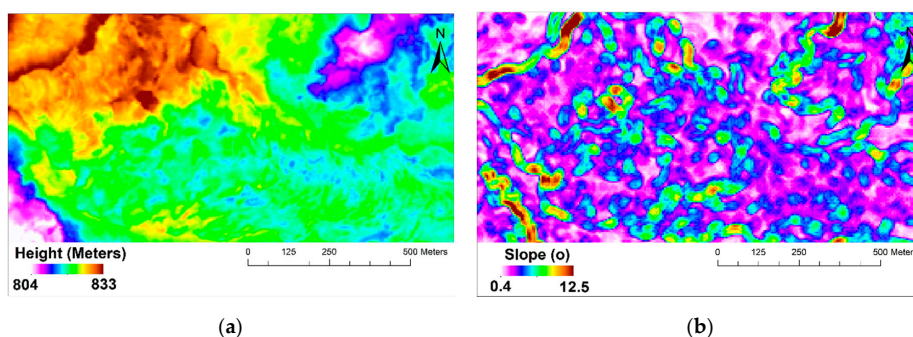


Figure 6. Cont.

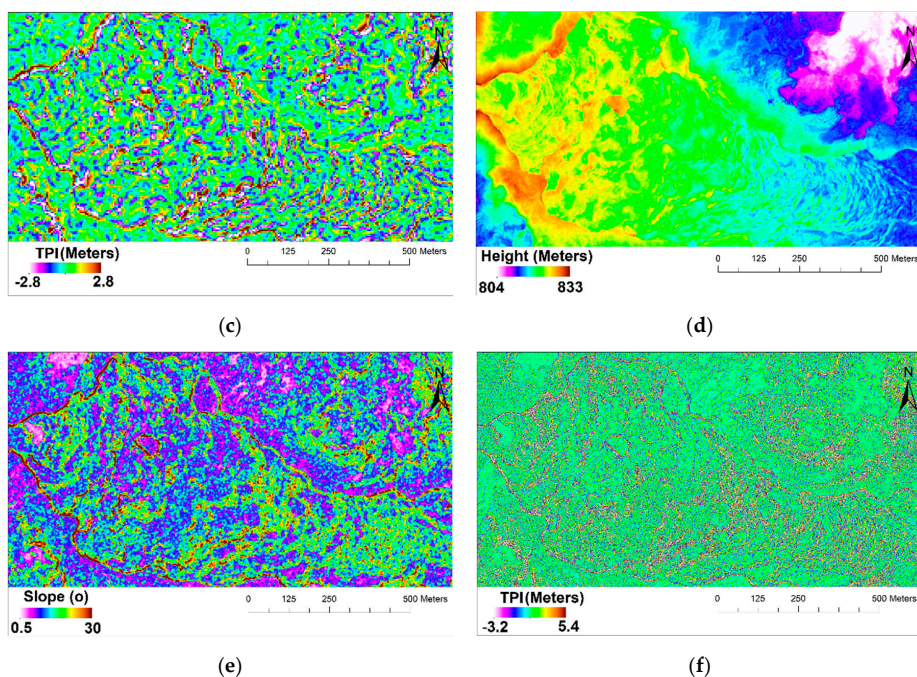


Figure 6. (a) DEM of lava pond derived from the photogrammetry image. (b) Slope of the lava pond derived from the photogrammetry DEM image. (c) TPI of lava pond derived from the photogrammetry DEM image. (d) DEM of lava pond derived from the LiDAR image. (e) TPI of lava pond derived from the DEM LiDAR image. (f) TPI lava pond derived from the DEM LiDAR image.

5.2. Spiny Lava Roughness

The photogrammetry DEM (Figure 7a) had TPI and slope values at the spiny lava ranging from -1.8 m to 2.2 m and from 0° to 38° (Figure 7b,c), respectively. On the other hand, the LiDAR DEM (Figure 7d), had TPI and slope values ranging from -2.1 m to 1.8 m and from 0° to 36° (Figure 6e,f). The LiDAR DEM does not cover the entirety of the spiny lava due to gaps in the image. The low TPI values correspond to a low slope and indicate a flat and smooth surface that has formed from inflated spiny lava; however, we cannot differentiate the spinose pattern in this meter scale. The irregular transitions from low to high TPI and slope pattern around the flow margin might indicate a rough surface resulting from a breakout from the inflated spiny lava. These features will be explained in more detail in Section 6.2.

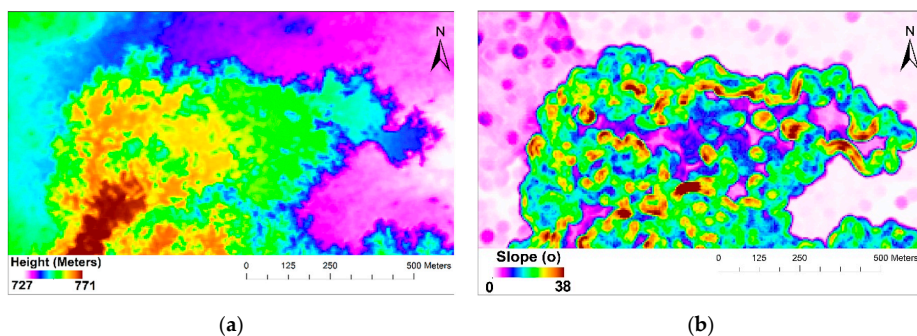


Figure 7. Cont.

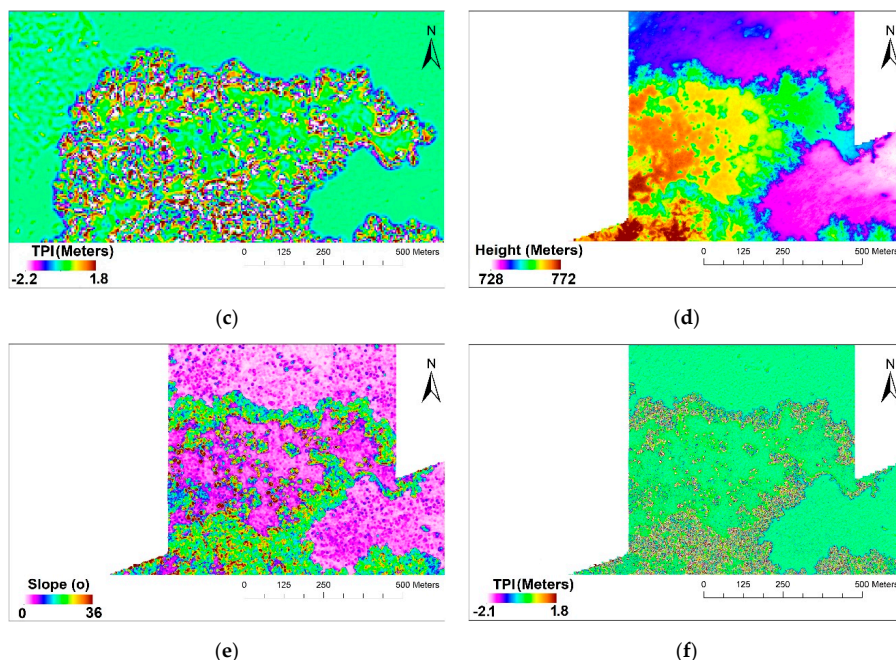


Figure 7. (a) DEM of spiny lava derived from the photogrammetry image. (b) Slope of the spiny lava from derived from the photogrammetry DEM image. (c) TPI of spiny lava channel derived from the photogrammetry DEM. (d) DEM of spiny lava derived from the LiDAR. (e) TPI of spiny lava derived from the DEM LiDAR. (f) TPI of spiny lava derived from the DEM LiDAR.

5.3. Inflated Channel Roughness

The photogrammetry DEM at the inflated channel (Figure 8a) yielded TPI and slope ranging from -3 m to 3.2 m and from 0.1° to 25° (Figure 8b,c), respectively. The LiDAR DEM (Figure 8d) yielded TPI and slope values ranging from -11 m to 4.8 m and from 0° to 33° (Figure 8e,f). Comparable to what we have found in spiny lava, low TPI patterns that correspond to a low slope were assigned to the flat surface of the inflated channel. The lowest TPI values correspond to a high slope indicating inflation pits and cracks. Inflation pits form where a portion of the flow is not inflating. The highest TPI values correspond to a high slope relating to boulders and grooves within the lava. The irregular transitions pattern from a low to a high slope and TPI values around the inflation margin are similar to what we have found on spiny lava. This indicates this feature is a rough surface that results from a breakout from the inflated channel (see Section 6.2 for more detail).

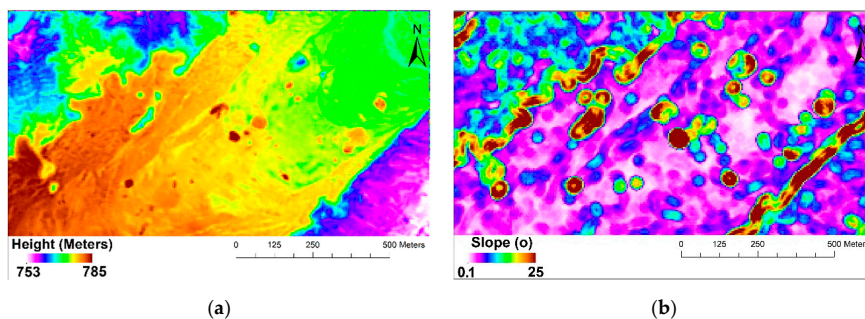


Figure 8. *Cont.*

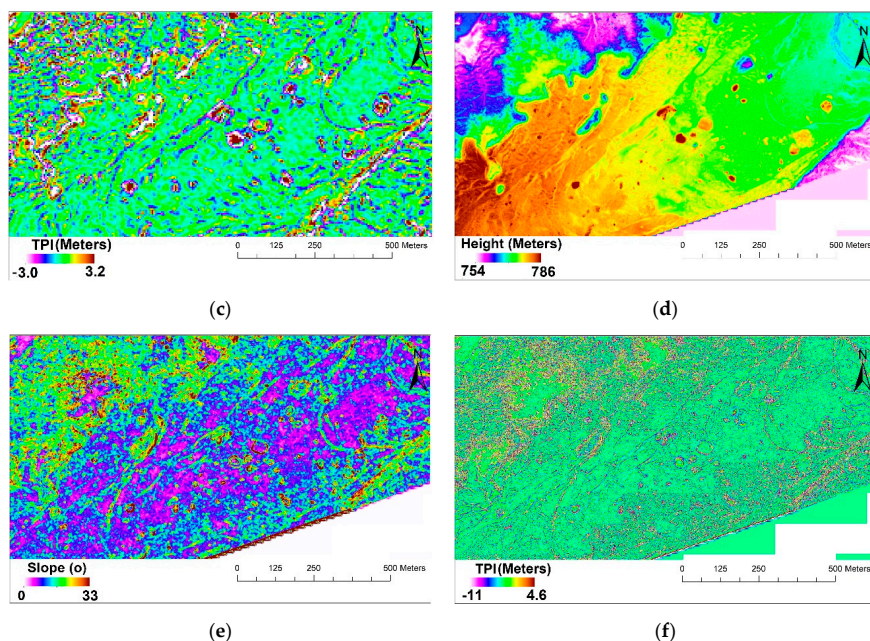


Figure 8. (a) DEM of the inflated channel derived from the photogrammetry image. (b) Slope of the inflated channel derived from the photogrammetry DEM. (c) TPI of the inflated channel derived from the photogrammetry DEM. (d) DEM of the inflated channel derived from the LiDAR. (e) TPI of the inflated channel derived from the DEM LiDAR. (f) TPI of the inflated channel derived from the DEM LiDAR.

5.4. Block Surface Roughness

The photogrammetry DEM (Figure 9a) at the blocky surface units had TPI and slope ranging from -2.1 m to 2 m and from 0.4° to 15° , respectively (Figure 9a,b). The LiDAR DEM (Figure 9d) had TPI, and slope values ranging from -2.3 m to 2.3 m and from 0° to 23° , respectively (Figure 9e,f). In the LiDAR, blocky surface, typically, had irregular TPI patterns. These patterns indicate that the surface is rough which related to the decimeter to meter scale blocks of fragmented pahoehoe-like crust. However, in the photogrammetry DEM, blocky surface appears to have smoother patterns corresponding to high slope since the roughness of the blocky surface is not distinct in lower resolution.

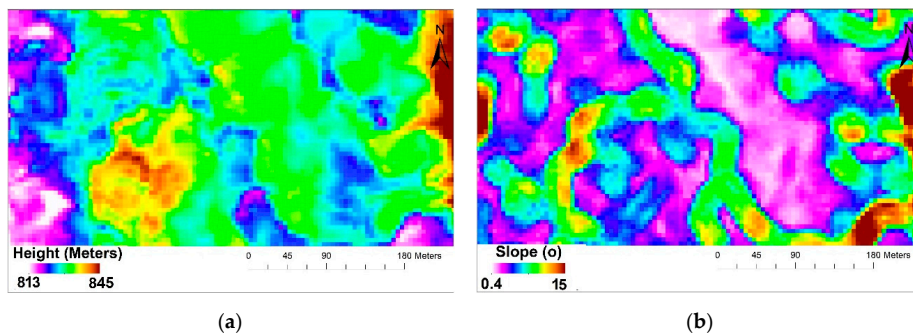


Figure 9. Cont.

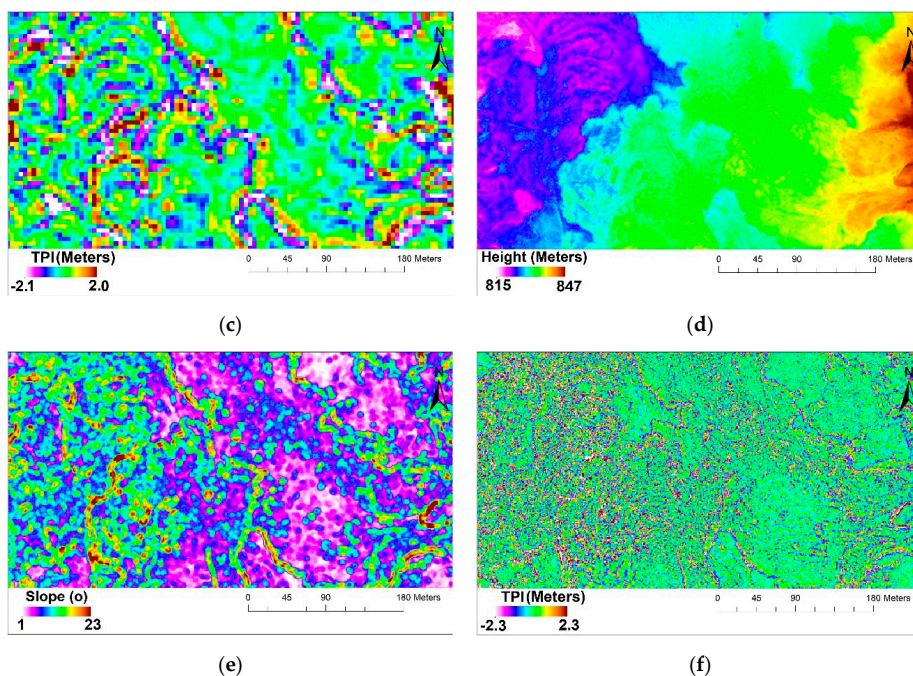


Figure 9. (a) DEM of blocky lava derived from the photogrammetry image. (b) The slope of the blocky surface derived from the photogrammetry DEM. (c) TPI of blocky surface derived from the photogrammetry DEM. (d) DEM of blocky lava derived from the LiDAR. (e) TPI of blocky surface derived from the DEM LiDAR. (f) TPI of blocky surface derived from the DEM LiDAR.

5.5. Hurst Exponent Derived Roughness

One Dimensional TPI Profiles

The one-dimensional TPI profiles over the four lava flow units are shown in Figure 10a–d. Based on H reported in Table 3, the surface roughness of lava features falls within the range from 0.3 ± 0.05 to 0.76 ± 0.04 . Typically, LiDAR DEM yields lower Hurst exponent values than photogrammetry DEM. This was also found for blocky surface, i.e., photogrammetry DEM had higher Hurst exponent than LiDAR DEM. LiDAR DEM has greater pixel resolution than photogrammetry DEM which results in more detailed TPI profiles. This issue will be addressed in Section 6.1. Based on the Mean Hurst exponent (\bar{H}), the roughest surface is the blocky surface with \bar{H} around 0.52 ± 0.04 and the inflated lava field appears to be the smoothest surface of these four lava units with \bar{H} around 0.61 ± 0.06 . These results are comparable with the results from the TPI map pattern that showed that inflated lava appears to be the smoothest surface, and blocky is the roughest surface. In general, the Hurst exponent values have a strong tendency to be close to 0.5. This was also suggested by an early study by Shepard et al. [2] for geological surface roughness.

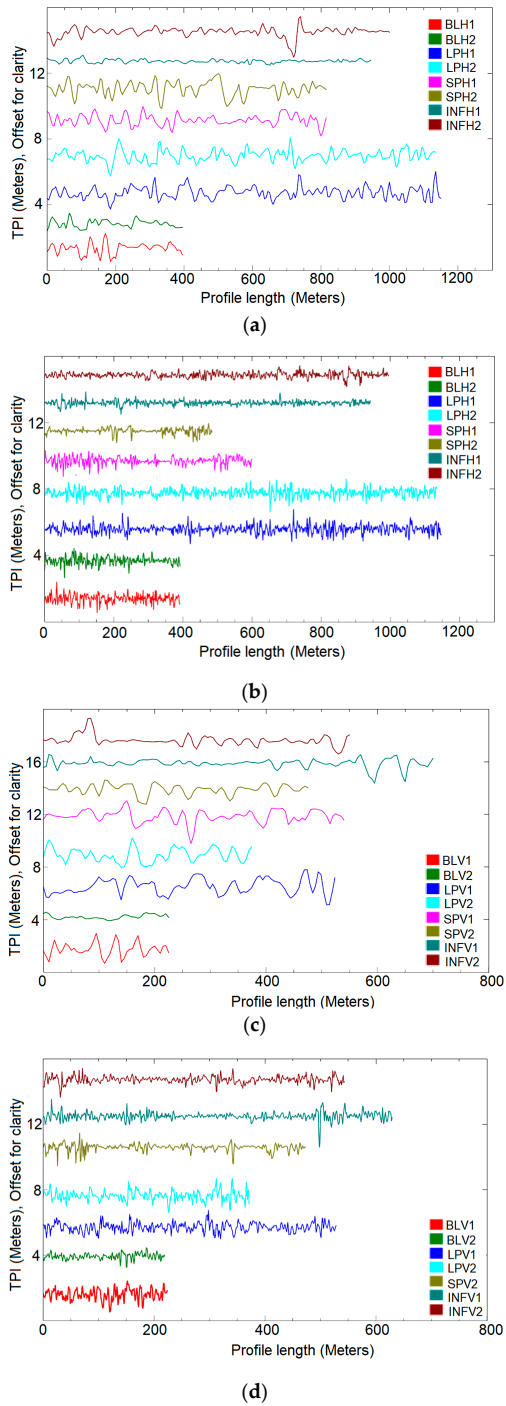


Figure 10. TPI profiles representing four different lava units at the 2014–2015 Holuhraun lava flow in Iceland; (a) horizontal profiles derived from photogrammetry DEM; (b) horizontal profiles derived from LiDAR DEM; (c) vertical profiles derived from photogrammetry DEM; (d) vertical profiles derived from LiDAR DEM. The profiles had been offset from each other for clarity.

Table 3. Lava flow roughness properties at the 2014–2015 eruption at Holuhraun, derived from one-dimension TPI profiles for each lava unit.

Profile	Lava Feature	Length (m)	H (Photogrammetry)	H (LiDAR)	H (Mean)
LPH1	Lava pond	1150	0.53 ± 0.07	0.52 ± 0.05	0.55 ± 0.06
LPH2	Lava pond	1150	0.55 ± 0.06	0.43 ± 0.07	
LPV1	Lava pond	530	0.56 ± 0.06	0.6 ± 0.03	
LPV2	Lava pond	370	0.65 ± 0.05	0.57 ± 0.06	0.58 ± 0.05
SPH1	Spiny	810	0.52 ± 0.06	0.56 ± 0.05	
SPH2	Spiny	810	0.65 ± 0.06	0.56 ± 0.05	
SPV1	Spiny	540	0.63 ± 0.04	- *	
SPV2	Spiny	480	0.63 ± 0.04	0.54 ± 0.06	
INFH1	Inflated channel	950	0.66 ± 0.06	0.52 ± 0.04	0.61 ± 0.06
INFH2	Inflated channel	1000	0.69 ± 0.06	0.55 ± 0.06	
INFV1	Inflated channel	630	0.56 ± 0.07	0.56 ± 0.06	
INFV2	Inflated channel	540	0.76 ± 0.04	0.60 ± 0.05	
BLH1	Blocky surface	390	0.61 ± 0.04	0.49 ± 0.03	0.52 ± 0.04
BLH2	Blocky surface	390	0.65 ± 0.05	0.56 ± 0.03	
BLV1	Blocky surface	220	0.4 ± 0.05	0.30 ± 0.04	
BLV2	Blocky surface	220	0.65 ± 0.05	0.52 ± 0.03	

* was not acquired due to the gap in the LiDAR data.

6. Discussion

In this work, we examined lava flows roughness in the 2014–2015 lava field at Holuhraun using TPI and one-dimensional H profiles. Both TPI and H successfully derived lava roughness on selected lava units at Holuhraun. However, there are still some issues. How does the scale affect the roughness results for both TPI and Hurst exponent? Is the ‘smooth’ surface still smooth for a different scale? How do we connect the roughness to the emplacement style? What can we improve to get a better roughness assessment? In this section, we address several issues related to (1) TPI neighborhood size and profile length, (2) Eruption condition and link roughness pattern with the emplacement style, and (3) alternative datasets and methods for deriving roughness.

6.1. TPI Neighborhood Size and Profile Length

TPI is naturally very scale dependent [11,19,48,50]. We should consider what scale is the most relevant for the study being analyzed [19]. The patterns produced by TPI vary on the scale that we use to analyze. Figure 11 shows an illustration of similar topography using different neighborhood sizes in TPI [19,51]. We test different TPI neighborhood sizes on LiDAR DEM spiny lava, as shown in Figure 12a–d. The 1 × 1 neighborhood size (Figure 12a) was not as clear as the larger scales to differentiate flow margins but appears to emphasize small features on the lava flows, which does not show in larger neighborhoods. James [11] recommends building a catalog of features presented at each scale. This could be useful in assessing the topographic characteristics of a lava flow surface.

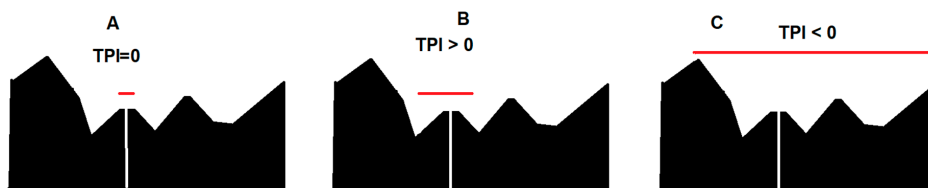


Figure 11. The illustration of the effects of the neighborhood size on TPI value adapted and modified from Jenness [19]. The red line depicts the neighborhood size. In topography (A), the neighborhood size is small enough that the point is at about the same elevation as the entire analysis region, so the TPI value is approximately 0, which means it is a flat surface. In topography (B), the neighborhood size is large enough to encompass the entire small hill, and the point is consequently much higher than its surroundings and has a correspondingly high TPI value resulting in that the point is detected as a ridge [19]. In topography (C), the neighborhood includes the hills on either side of the valley, and therefore the point is lower than its neighbors and has a negative TPI value [11,19].

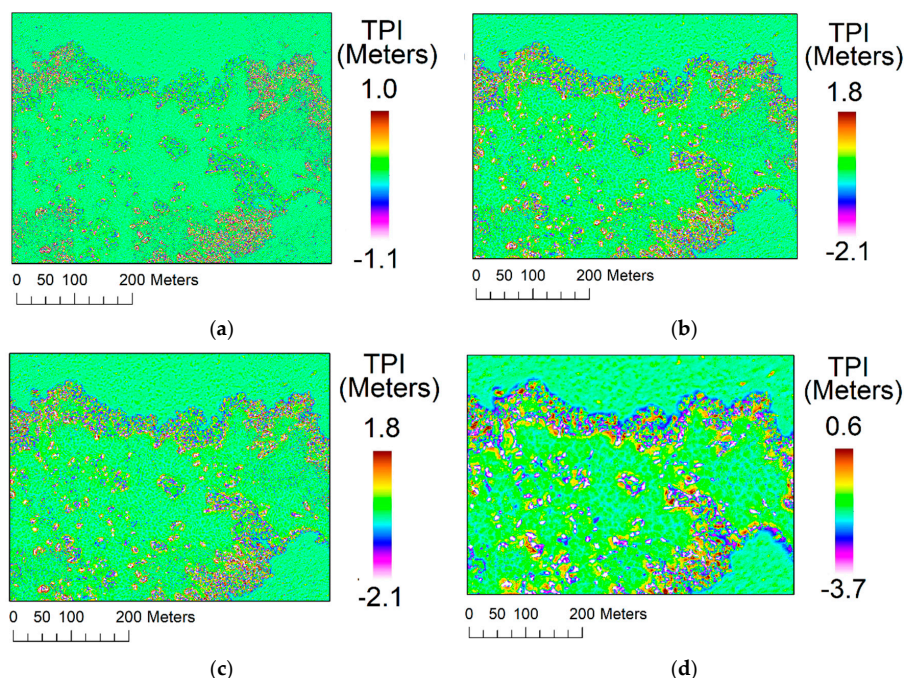


Figure 12. TPI maps derived from LiDAR DEM at spiny lava for different neighborhood size (a) 1×1 neighborhood size; (b) 3×3 neighborhood size; (c) 5×5 neighborhood size; (d) 10×10 neighborhood size.

We consider that there are at least two factors that affect the H values: (1) pixel size and (2) the profile length. Figure 13a shows TPI profiles representing blocky surface vertical profile (BLV1) from LiDAR DEM and photogrammetry DEM. The LiDAR DEM profile is rougher than the photogrammetry DEM since the spatial spacing (pixel size) in the LiDAR DEM is denser than photogrammetry DEM because the resolution is higher (1 m vs. 5 m). This spatial spacing issue corresponds to the TPI neighborhood size in Figure 11, where LiDAR DEM captures more detailed TPI value than photogrammetry DEM which affects the Hurst exponent derived roughness. Second, we also consider the profile length as a factor that affects the Hurst exponent values. In Figure 13b, we subset the first 100 m BLV1 profiles, and the Hurst exponent values for these subset profiles were increased for both topographies. For LiDAR DEM the Hurst exponent values are 0.55 ± 0.05 compared to 0.30 ± 0.05 for full profiles,

and for photogrammetry DEM the Hurst exponent values are 0.48 ± 0.01 compared to 0.40 ± 0.05 for full profiles. These results not necessarily conclude that the shorter profiles will increase the Hurst exponent. Extended profiles also can increase the Hurst exponent since the profiles could be equally rough, which can represent a ‘smooth’ surface [2]. In many cases, it depends on the morphology that we are studying [2,3], and we should know the morphology. The other thing we found is that the direction of profiles could bias the Hurst exponent [7,52]. We recommend in a future study to build series of profiles that are rotated by some number of degrees to capture a wider range of directions around the surface area of interest to derive precise roughness. Some studies are currently developing three-dimensional roughness estimates based on a 3D Gaussian filter applied to DEM [53].

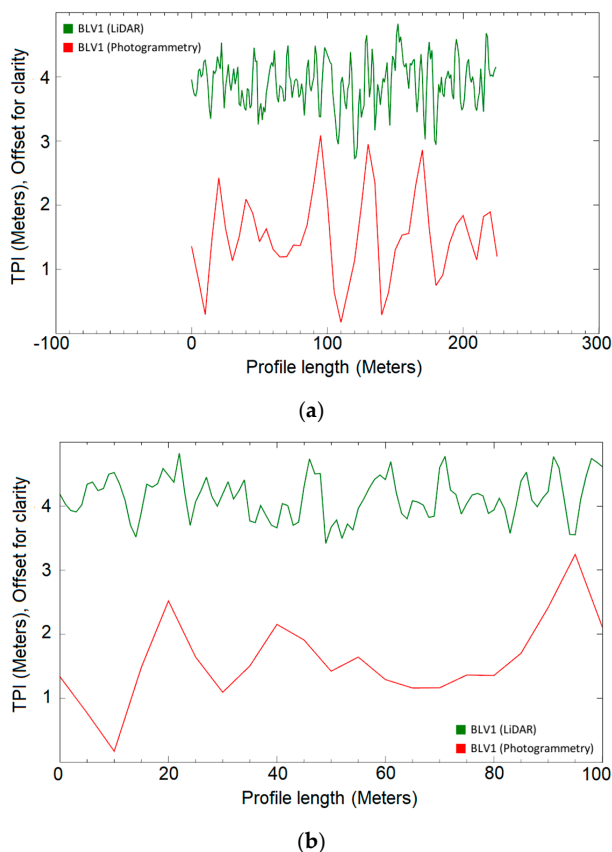


Figure 13. TPI profiles representing the first vertical profile of the blocky surface (BLV1) from the LiDAR DEM (green) and the photogrammetry DEM (red). (a) full profiles; (b) a zoom-in of the first 100 meters of (a). The profiles had been offset from each other for clarity.

6.2. Eruption Condition and Link Quantitative Roughness with the Emplacement Style

Quantitative roughness measurement of lava flow features provides insight into the relative emplacement styles. In particular, higher H and intermediate TPI patterns suggest a smoother surface, which reflects relatively lower viscosity lavas than for the lower H and irregular TPI pattern. However, roughness variations do not directly distinguish between lava viscosity. To quantify precise viscosity, more factors need to consider rather than single roughness. The difference in viscosity may be the result of transport within an insulated distributary system that limits heat loss. If the differences between the flow types are predominantly textural, local supply may be a controlling factor [5].

The two primary roughness identified in the, a smooth surface possibly inflated flow type and a rough surface possibly breakout, blocky surface and ropy fold data. Sections 5.2 and 5.3 shows that smoother surface types exhibit morphologic properties attributed to flow inflation. Along margins, irregular transitions TPI pattern supports the interpretation of the occurrence of breakout (Figures 7c–f and 8c–f). As displayed clearly in Figure 14a–b, the rough surface in lava flow margins from the three-dimension LiDAR surface model. These rough surfaces result from a breakout from the inflated surface from both spiny lava (Figure 14a) and inflated channel (Figure 14b). It is reported by Pedersen et al. [37] that a series of breakouts occurred during the third phase of the eruption, mostly in the flow margin and also in inflated channels. This breakout is inferred from the false color on the Earth Observing 1 (EO-1) Advanced Land Imager (ALI) satellite during the eruption (Figure 15). These breakouts occurred around 16 January 2015, a breakout from spiny lava and inflated channel. A breakout is a lobe originating from the liquid interior of active lava. It may take place through a crack at the front or the side of the flow margin when lava is inflated [54]. Injection of fresh basaltic magma into an established flow produces new breakouts of lava and promotes lifting of the upper crust (inflation). These breakout phenomena illustrated in Figure 16.

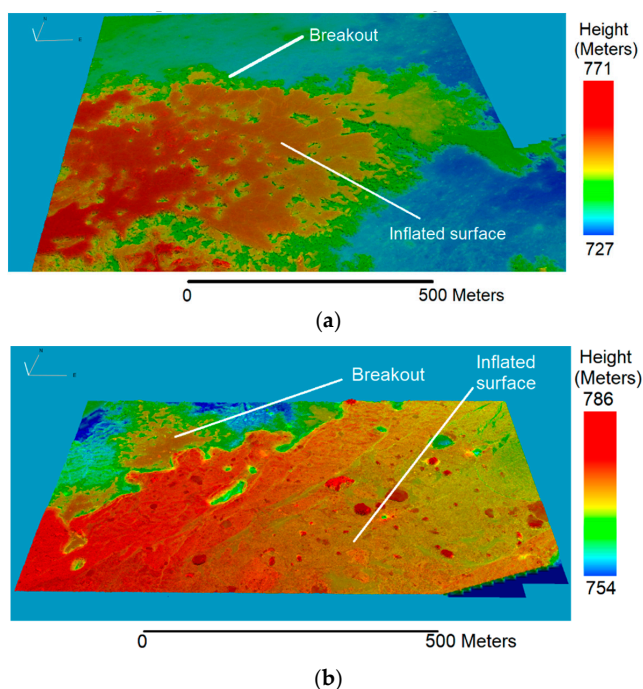
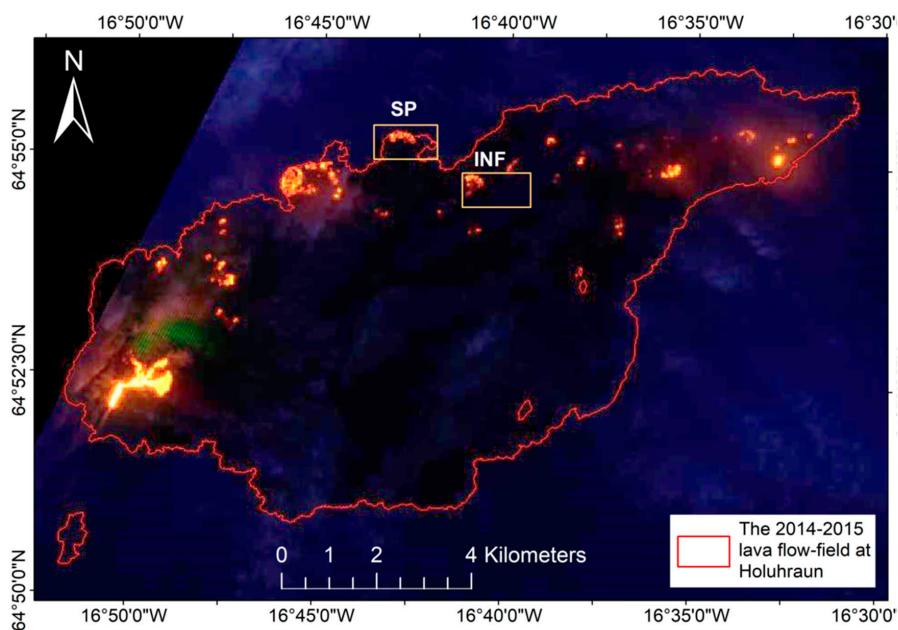
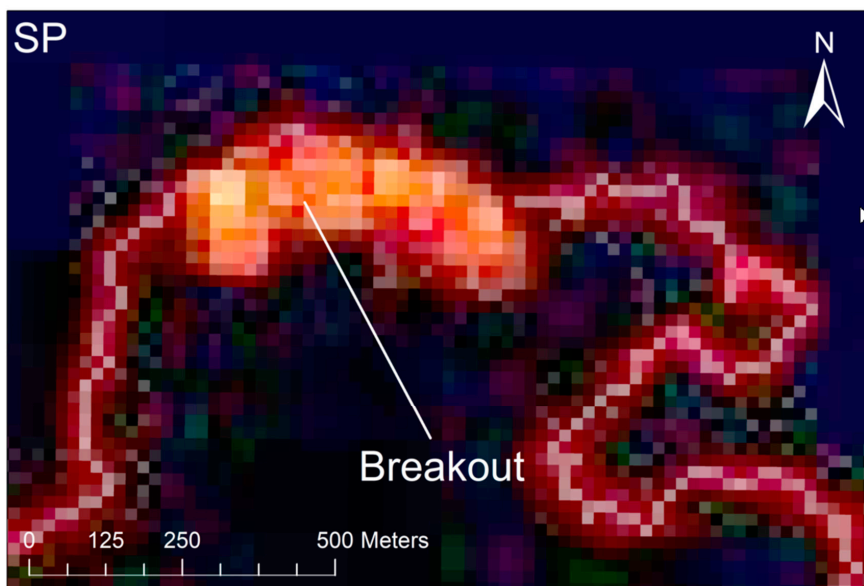


Figure 14. Three-dimensional LiDAR surface model, white line indicating breakout and inflated surface. (a) Spiny lava flow margin. (b) Inflated channel flow margin.

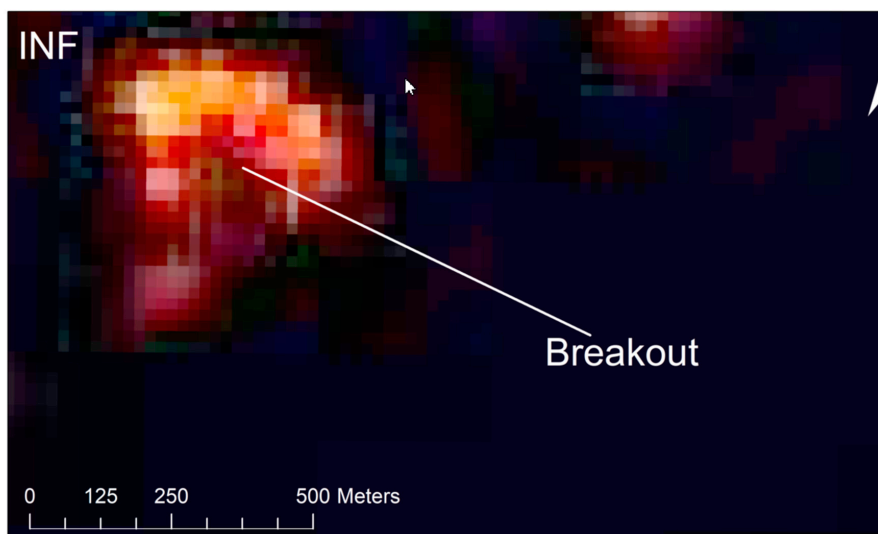


(a)



(b)

Figure 15. Cont.



(c)

Figure 15. (a) EO-ALI False color band 7,5,4' on 16 January 2015 shows the high-temperature area during the eruption at Holuhraun. Boxes show series of breakout occurred in the flow margin, including on: (b) spiny lava and; (c) inflated channel margin.

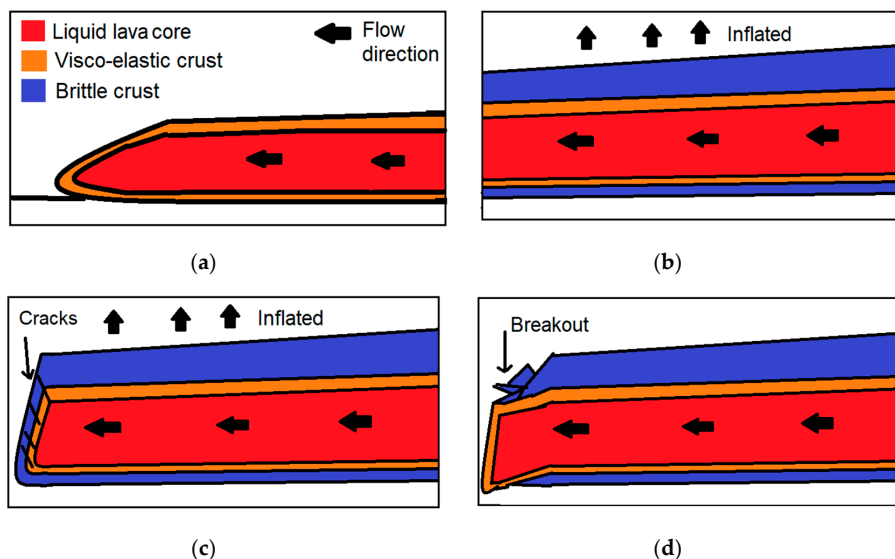


Figure 16. Cartoon illustrated the lava breakout. (a) A lava core exists within the lava channel/lobe under the visco-elastic crust. The lava core is contained within a visco-elastic skin covered by a brittle crust. (b) The lava flow became re-activated, and the lava core injected acted as a flow path promotes lifting of the upper crust (inflation). (c) Cracks formed on crust on the lava flow front/margin. (d) When the inflation continues, the crust eventually breaks, and breakouts leak from the margin or flow front of the inflated surface.

6.3. Alternative Datasets and Methods for Deriving Roughness

Recently, a number of methods are used to quantify surface roughness. Neish et al. [7] quantified the surface roughness from synthetic aperture radar (SAR) using the circular polarization ratio (CPR). This technique is defined as the radar backscatter ratio in the same polarization that was transmitted (SC) to the opposite polarization (OC), where the CPR is SC divided by OC [7]. Rough surfaces tend to have approximately equal OC and SC returns, with CPR values approaching one. Meanwhile, the flat surfaces tend to have high OC returns and low CPR values [7]. We can also apply Hurst exponent to the radar backscattering profiles in order to derive roughness [15]. Neish et al. [7] also show that linking radar backscatter to the high-resolution topographic profiles is essential to understanding the structure of various geologic units. Another technique we could consider in describing roughness is optical images (multispectral–hyperspectral). Several studies characterize roughness from multispectral and hyperspectral based on the spectral reflectance [27,31,55,56]. The main assumption is that rough surface has lower reflectance than a smooth surface. The integration of these techniques with field measurement could improve surface roughness estimation of lava flow.

7. Conclusions

In this study, both TPI and one-dimensional H successfully derive quantitative flow roughness. The roughness assessment was acquired from four lava flow features: (1) spiny lava, (2) lava pond, (3) blocky surface, and (4) inflated channel. TPI patterns on spiny lava and inflated channels show that the intermediate TPI patterns with low slope indicate flat and smooth surface. Lava pond has transitions pattern from low to high TPI values forming a wave-like pattern. Meanwhile, irregular transitions from low to high TPI and the slope patterns indicate a rough surface that is found in blocky surface and flow margins, indicating lava breakouts. Quantitative measures of surface roughness of lava features fall within the H ranges from 0.30 ± 0.05 to 0.76 ± 0.04 . The roughest surface is the blocky surface, and the inflated lava flow appears to be the smoothest surface among these four lava units. In general, the Hurst exponent values in the 2014–2015 lava field at Holuhraun has a strong tendency to be close to 0.5, which has good agreement with an earlier study for geological surface roughness. Neighborhood size is a critical component for TPI to quantify the roughness. Small neighborhoods capture small and local features and valleys, while large neighborhoods capture larger-scale features. We consider that there are at least two factors that affect the Hurst exponent values: (1) pixel size and (2) the profile length. We recommend in a future study to build a series of profiles that are rotated by some number of degrees to capture a wider range of directions, in order to derive precise roughness. The integration of multimodal remote sensing datasets and field measurement can improve the estimation of surface roughness of lava flow.

Author Contributions: Conceptualization, implementation, and preparation of the manuscript, M.A.; Supervision, Á.H., M.O.U., I.J., and T.T. All authors have read and agreed to the published version of the manuscript.

Funding: The first author was supported by the Indonesia Endowment Fund for Education (LPDP) Grant No. 20160222025516, European Network of Observatories and Research Infrastructures for Volcanology (EUROVOLC), and Vinir Vatnajökuls during his Ph.D. project. LiDAR airborne datasets provided by The European Facility for Airborne Research (EUFAR) and airborne photogrammetry provided by Loftmyndir ehf.

Acknowledgments: The authors would thank to Christopher Hamilton and anonymous reviewers for their thoughtful and constructive comments for the manuscript.

Conflicts of Interest: The authors declare no conflict of interest.

References

- Mills, G.; Fotopoulos, G. On the estimation of geological surface roughness from terrestrial laser scanner point clouds. *Geosphere* **2013**, *9*, 1410–1416. [\[CrossRef\]](#)
- Shepard, M.K.; Bulmer, M.H.; Gaddis, L.R.; Plaut, J.J.; Campbell, B.A.; Farr, T. The roughness of natural terrain: A planetary and remote sensing perspective. *J. Geophys. Res. Space Phys.* **2001**, *106*, 32777–32795. [\[CrossRef\]](#)
- Gaddis, L.R.; Mouginiis-Mark, P.J.; Hayashi, J.N. Lava flow surface textures: SIR-B radar image texture, field observations, and terrain measurements. *Photogramm. Eng. Remote Sens.* **1990**, *56*, 211–224.
- Campbell, B.A.; Shepard, M.K. Lava flow surface roughness and depolarized radar scattering. *J. Geophys. Res. Space Phys.* **1996**, *101*, 18941–18951. [\[CrossRef\]](#)
- Crown, D.A.; Ramsey, M. Morphologic and thermophysical characteristics of lava flows southwest of Arsia Mons, Mars. *J. Volcanol. Geotherm. Res.* **2017**, *342*, 13–28. [\[CrossRef\]](#)
- Whelley, P.; Garry, W.B.; Hamilton, C.W.; Bleacher, J. LiDAR-derived surface roughness signatures of basaltic lava types at the Muliwai a Pele Lava Channel, Mauna Ulu, Hawai'i. *Bull. Volcanol.* **2017**, *79*, 79. [\[CrossRef\]](#)
- Neish, C.; Hamilton, C.; Hughes, S.; Nawotniak, S.K.; Garry, W.; Skok, J.; Elphic, R.; Schaefer, E.; Carter, L.; Bandfield, J.; et al. Terrestrial analogues for lunar impact melt flows. *Icarus* **2017**, *281*, 73–89. [\[CrossRef\]](#)
- Morris, A.; Anderson, F.S.; Haldemann, A.F.C.; Brooks, B.A.; Foster, J.; Mouginiis-Mark, P.J. Roughness of Hawaiian volcanic terrains. *J. Geophys. Res. Space Phys.* **2008**, *113*. [\[CrossRef\]](#)
- Anderson, S.W.; Stofan, E.; Plaut, J.J.; Crown, D.A. Block size distributions on silicic lava flow surfaces: Implications for emplacement conditions. *GSA Bull.* **1998**, *110*, 1258–1267. [\[CrossRef\]](#)
- Byrnes, J.M. Lava Flow Field Emplacement Studies on Mauna Ulu (Kilauea, Volcano, Hawai'i, USA) and Venus, Using Field and Remote Sensing Analyses. Ph.D. Thesis, University of Pittsburgh, Pittsburgh, PA, USA, 2002; pp. 1–212.
- James, D.H. Comparing Terrestrial and Extraterrestrial Lava Surface Roughness Using Digital Elevation Models From High Resolution Topography and Structure From Motion. Master's Thesis, University of Northern Colorado, Greeley, CO, USA, 2019.
- Richardson, P.W.; Karlstrom, L. The multi-scale influence of topography on lava flow morphology. *Bull. Volcanol.* **2019**, *81*, 21. [\[CrossRef\]](#)
- Favalli, M.; Fornaciai, A.; Nannipieri, L.; Harris, A.; Calvari, S.; Lormand, C. UAV-based remote sensing surveys of lava flow fields: A case study from Etna's 1974 channel-fed lava flows. *Bull. Volcanol.* **2018**, *80*, 29. [\[CrossRef\]](#)
- Gharechelou, S.; Tateishi, R.; Johnson, B.A. A Simple Method for the Parameterization of Surface Roughness from Microwave Remote Sensing. *Remote. Sens.* **2018**, *10*, 1711. [\[CrossRef\]](#)
- Aufaristama, M.; Höskuldsson, Á.; Jónsdóttir, I.; Úlfarsson, M.; Thordarson, T. New Insights for Detecting and Deriving Thermal Properties of Lava Flow Using Infrared Satellite during 2014–2015 Effusive Eruption at Holuhraun, Iceland. *Remote. Sens.* **2018**, *10*, 151. [\[CrossRef\]](#)
- Mallonee, H.C.; Kobs Nawotniak, S.E.; McGregor, M.; Hughes, S.S.; Neish, C.D.; Downs, M.; Delparte, D.; Lim, D.S.S.; Heldmann, J.L.; Team, F. Lava flow morphology classification based on measures of roughness. In Proceedings of the 48th Lunar and Planetary Science Conference, The Woodlands, TX, USA, 20–24 March 2017.
- Witt, T.; Walter, T.R.; Müller, D.; Guðmundsson, M.T.; Schöpa, A. The relationship between lava fountaining and vent morphology for the 2014–2015 Holuhraun eruption, Iceland, analyzed by video monitoring and topographic mapping. *Front. Earth Sci.* **2018**, *6*, 235. [\[CrossRef\]](#)
- Kereszturi, G.; Németh, K.; Moufti, M.R.; Cappello, A.; Murcia, H.; Ganci, G.; Del Negro, C.; Procter, J.; Zahran, H.M.A. Emplacement conditions of the 1256AD Al-Madinah lava flow field in Harrat Rahat, Kingdom of Saudi Arabia—Insights from surface morphology and lava flow simulations. *J. Volcanol. Geotherm. Res.* **2016**, *309*, 14–30. [\[CrossRef\]](#)
- Jennes, J. *Topographic Position Index (tpi_jen.avx) Extension for ArcView 3.x, v. 1.3a*; Jenness Enterprises: Flagstaff, AZ, USA, 2006; pp. 1–43.
- Swanson, D.A. Pahoehoe Flows from the 1969–1971 Mauna Ulu Eruption, Kilauea Volcano, Hawaii. *GSA Bull.* **1973**, *84*, 615. [\[CrossRef\]](#)
- Lopes, R.M.C.; Kilburn, C.R.J. Emplacement of lava flow fields: Application of terrestrial studies to Alba Patera, Mars. *J. Geophys. Res. Space Phys.* **1990**, *95*, 14383. [\[CrossRef\]](#)

22. Diniega, S.; Smrekar, S.E.; Anderson, S.; Stofan, E.R. The influence of temperature-dependent viscosity on lava flow dynamics. *J. Geophys. Res. Earth Surf.* **2013**, *118*, 1516–1532. [[CrossRef](#)]
23. Ramsey, M.S.; Fink, J.H. Estimating silicic lava vesicularity with thermal remote sensing: A new technique for volcanic mapping and monitoring. *Bull. Volcanol.* **1999**, *61*, 32–39. [[CrossRef](#)]
24. Guest, J.E.; Duncan, A.M.; Stofan, E.R.; Anderson, S.W. Effect of slope on development of pahoehoe flow fields: Evidence from Mount Etna. *J. Volcanol. Geotherm. Res.* **2012**, *219*, 52–62. [[CrossRef](#)]
25. Kilburn, C.R.J. Lava flows and flow fields. In *Encyclopedia of Volcanoes*; Sigurdsson, H., Ed.; Academic Press: San Diego, CA, USA, 2000; pp. 291–305.
26. Hamilton, C.W. Fill and spill” lava flow emplacement: Implications for understanding planetary flood basalt eruptions. In *NASA Technical Memorandum: Marshall Space Flight Center Faculty Fellowship Program*; Six, N., Karr, G., Eds.; NASA Marshall Space Flight Center: Huntsville, AL, USA, 2019; pp. 47–56.
27. Byrnes, J.M.; Ramsey, M.S.; Crown, D. A Surface unit characterization of the Mauna Ulu flow field, Kilauea Volcano, Hawai’i, using integrated field and remote sensing analyses. *J. Volcanol. Geotherm. Res.* **2004**, *135*, 169–193. [[CrossRef](#)]
28. Griffiths, R.W.; Fink, J.H. The morphology of lava flows in planetary environments: Predictions from analog experiments. *J. Geophys. Res. Space Phys.* **1992**, *97*, 19739. [[CrossRef](#)]
29. Anderson, S.W.; Fink, J.H. *The Development and Distribution of Surface Textures at the Mount St. Helens Dome*; Springer Science and Business Media LLC: Berlin/Heidelberg, Germany, 1990; Volume 2, pp. 25–46.
30. Fink, J.H.; Fletcher, R.C. Ropy pahoehoe: Surface folding of a viscous fluid. *J. Volcanol. Geotherm. Res.* **1978**, *4*, 151–170. [[CrossRef](#)]
31. Byrnes, J.M.; Crown, D.A. Morphology, stratigraphy, and surface roughness properties of Venusian lava flow fields. *J. Geophys. Res. Space Phys.* **2002**, *107*, 9-1. [[CrossRef](#)]
32. Moore, R.B.; Clague, D.A.; Rubin, M.; Bohron, W.A. *Volcanism in Hawaii*; U.S. Geological Survey Professional Paper 1350; U.S. Geological Survey: Reston, VA, USA, 1987.
33. Wall, S.; Farr, T.; Muller, J.-P.; Lewis, P.; Leberl, F. Measurement of surface microtopography using helicopter-mounted stereo film cameras and two stereo matching techniques. In *Proceedings of the 12th Canadian Symposium on Remote Sensing Geoscience and Remote Sensing Symposium*, Vancouver, BC, Canada, 10–14 July 1989.
34. Cashman, K.V.; Thornber, C.; Kauahikaua, J.P. Cooling and crystallization of lava in open channels, and the transition of Pāhoehoe Lava to ‘A’ā. *Bull. Volcanol.* **1999**, *61*, 306–323. [[CrossRef](#)]
35. Whelley, P.; Glaze, L.S.; Calder, E.S.; Harding, D.J. LiDAR-Derived Surface Roughness Texture Mapping: Application to Mount St. Helens Pumice Plain Deposit Analysis. *IEEE Trans. Geosci. Remote. Sens.* **2013**, *52*, 426–438. [[CrossRef](#)]
36. Bretar, F.; Arab-Sedze, M.; Champion, J.; Pierrot-Deseilligny, M.; Heggy, E.; Jacquemoud, S. An advanced photogrammetric method to measure surface roughness: Application to volcanic terrains in the Piton de la Fournaise, Reunion Island. *Remote. Sens. Environ.* **2013**, *135*, 1–11. [[CrossRef](#)]
37. Pedersen, G.B.M.; Höskuldsson, A.; Dürig, T.; Thordarson, T.; Jónsdóttir, I.; Riishuus, M.S.; Óskarsson, B.V.; Dumont, S.; Magnússon, E.; Gudmundsson, M.T.; et al. Lava field evolution and emplacement dynamics of the 2014–2015 basaltic fissure eruption at Holuhraun, Iceland. *J. Volcanol. Geotherm. Res.* **2017**, *340*, 155–169. [[CrossRef](#)]
38. Bonny, E.; Thordarson, T.; Wright, R.; Höskuldsson, Á.; Jónsdóttir, I. The Volume of Lava Erupted During the 2014 to 2015 Eruption at Holuhraun, Iceland: A Comparison Between Satellite- and Ground-Based Measurements. *J. Geophys. Res. Solid Earth* **2018**, *123*, 5412–5426. [[CrossRef](#)]
39. Diego, C.; Ripepe, M.; Marco, L.; Cigolini, C. Modelling satellite-derived magma discharge to explain caldera collapse. *Geology* **2017**, *45*, 523–526.
40. Pedersen, G.; Höskuldsson, A.; Riishuus, M.S.; Jónsdóttir, I.; Thórdarson, T.; Gudmundsson, M.T.; Durmont, S. Emplacement dynamics and lava field evolution of the flood basalt eruption at Holuhraun, Iceland: Observations from field and remote sensing data. In *Proceedings of the EGU General Assembly*, Vienna, Austria, 17–22 April 2016; Volume 18, p. 13961.
41. Rowland, S.K.; Walker, G.P. Pahoehoe and aa in Hawaii: Volumetric flow rate controls the lava structure. *Bull. Volcanol.* **1990**, *52*, 615–628. [[CrossRef](#)]

42. Gíslason, S.; Stefánsdóttir, G.; Pfeffer, M.A.; Barsotti, S.; Jóhannsson, T.; Galeczka, I.; Bali, E.; Sigmarsson, O.; Stefánsson, A.; Keller, N.S.; et al. Environmental pressure from the 2014–15 eruption of Bárðarbunga volcano, Iceland. *Geochem. Perspect. Lett.* **2015**, *1*, 84–93. [[CrossRef](#)]
43. Gudmundsson, M.T.; Jónsdóttir, K.; Hooper, A.; Holohan, E.; Halldórsson, S.A.; Ófeigsson, B.G.; Cesca, S.; Vogfjörð, K.S.; Sigmundsson, F.; Högnadóttir, T.; et al. Gradual caldera collapse at Bárðarbunga volcano, Iceland, regulated by lateral magma outflow. *Science* **2016**, *353*, aaf8988. [[CrossRef](#)] [[PubMed](#)]
44. Aufaristama, M.; Höskuldsson, Á.; Ulfarsson, M.; Jónsdóttir, I.; Thordarson, T. The 2014–2015 Lava Flow Field at Holuhraun, Iceland: Using Airborne Hyperspectral Remote Sensing for Discriminating the Lava Surface. *Remote. Sens.* **2019**, *11*, 476. [[CrossRef](#)]
45. Hargitai, H. Inflated lava flow. In *Encyclopedia of Planetary Landforms*; Hargitai, H., Kereszturi, Á., Eds.; Springer: New York, NY, USA, 2015; pp. 1029–1034.
46. Florinsky, I. Accuracy of local topographic variables derived from digital elevation models. *Int. J. Geogr. Inf. Sci.* **1998**, *12*, 47–62. [[CrossRef](#)]
47. Zhou, Q.; Liu, X. Analysis of errors of derived slope and aspect related to DEM data properties. *Comput. Geosci.* **2004**, *30*, 369–378. [[CrossRef](#)]
48. Guisan, A.; Weiss, S.B. GLM versus CCA spatial modeling of plant species distribution. *Plant Ecol.* **1999**, *143*, 107–122. [[CrossRef](#)]
49. Liu, B.; Yao, L.; Fu, X.; He, B.; Bai, L. Application of the Fractal Method to the Characterization of Organic Heterogeneities in Shales and Exploration Evaluation of Shale Oil. *J. Mar. Sci. Eng.* **2019**, *7*, 88. [[CrossRef](#)]
50. Hirzel, A.; Guisan, A. Which is the optimal sampling strategy for habitat suitability modelling. *Ecol. Model.* **2002**, *157*, 331–341. [[CrossRef](#)]
51. Mokarram, M.; Roshan, G.; Negahban, S. Landform classification using topography position index (case study: Salt dome of Korsia-Darab plain, Iran). *Model. Earth Syst. Environ.* **2015**, *1*, 1–7. [[CrossRef](#)]
52. Hamilton, C.W.; Mouginiis-Mark, P.J.; Sori, M.M.; Scheidt, S.P.; Bramson, A.M. Episodes of Aqueous Flooding and Effusive Volcanism Associated With Hrad Vallis, Mars. *J. Geophys. Res. Planets* **2018**, *123*, 1484–1510. [[CrossRef](#)]
53. Fan, K.; Neish, C.D.; Zanetti, M.; Kukko, A. An improved methodology for 3-dimensional characterization of surface roughness as applied to lava flows. In Proceedings of the 49th Lunar and Planetary Science Conference 2018, The Woodlands, TX, USA, 19–23 March 2018.
54. Thordarson, T.; Self, S. The Roza Member, Columbia River Basalt Group: A gigantic pahoehoe lava flow field formed by endogenous processes? *J. Geophys. Res. Space Phys.* **1998**, *103*, 27411–27445. [[CrossRef](#)]
55. Spinetti, C.; Mazzarini, F.; Casacchia, R.; Colini, L.; Neri, M.; Behncke, B.; Salvatori, R.; Buongiorno, M.F.; Pareschi, M.T. Spectral properties of volcanic materials from hyperspectral field and satellite data compared with LiDAR data at Mt. Etna. *Int. J. Appl. Earth Obs. Geoinf.* **2009**, *11*, 142–155. [[CrossRef](#)]
56. Aufaristama, M.; Höskuldsson, Á.; Jonsdottir, I.; Ólafsdóttir, R. Mapping and Assessing Surface Morphology of Holocene Lava Field in Krafla (NE Iceland) Using Hyperspectral Remote Sensing. *IOP Conf. Ser. Earth Environ. Sci.* **2016**, *29*, 12002. [[CrossRef](#)]



Appendix A: Deriving Hurst exponent with R/S technique

The process for estimating the Hurst exponent from equation 8 and 9 are described in detail: Firstly data points (T) on profile series were divided into d contiguous sub-series of points τ , where $d \times \tau = T$, For each of these sub-series m , where $m = 1, \dots, d$:

- 1) Determine the mean, E_m , of each sub-series.
- 2) Determine the standard deviation, S_m , of each sub-series.
- 3) Normalized the data ($Z_{i,m}$) by subtracting the mean from each data point:

$$X_{i,m} = Z_{i,m} - E_m$$

- 4) Using the Normalized data create a cumulative profile series by consecutively summing the data points:

$$Y_{i,m} = \sum_{j=1}^i X_{j,m}, i = 1, \dots, \tau.$$

- 5) Using the new cumulative series find the range by subtracting the minimum value

from the maximum value from profiles:

$$R_m = \max(Y_{1,m}, \dots, Y_{\tau,m}) - \min(Y_{1,m}, \dots, Y_{\tau,m})$$

- 6) Rescale the range, R_m/S_m by dividing the range by the standard deviation.
- 7) Calculate the mean of the rescaled range for all sub-series of length τ .

$$(R/S)_\tau = \frac{1}{d} \sum_{m=1}^d R_m/S_m$$

- 8) The length of τ must be increased to the next higher value, where $d \times \tau = T$ and d is an integer value. Steps 1 to 7 are then repeated, these steps should be repeated until $\tau = T/2$.

- 9) Finally, the value of H is obtained using a simple least squares regression with

$\log(\tau)$ and $\log(R/S)$. The slope of the resulting equation (9) is the estimate of the Hurst exponent